Nuclear Magnetic Resonance of Low-Receptivity Nuclides: The First Demonstration of ^{61}Ni SSNMR as Applied to Structural and Crystallographic Characterization of Diamagnetic Nickel Complexes

Peter Werhun

A thesis submitted in partial fulfillment of the requirements for the degree of

Master of Science

Department of Chemistry and Biomolecular Sciences
Faculty of Science
University of Ottawa

TABLE OF CONTENTS

LIST OF FIGURES

LIST OF TABLES

LEGEND

δ_{iso}	(isotropic) chemical shift
η	asymmetry parameter (quadrupolar)
κ	skew
λ	linewidth parameter ($1/T_2$)
Ω	span (unless otherwise noted)
B3LYP	Becke 3 parameter exchange/Lee-Yang-Parr correlation hybrid functional
BP86	Becke exchange/Perdew correlation GGA functional
CPMG/QCPMG	Carr-Purcell-Meiboom-Gill/Quadrupolar CPMG
C_{Q}	Quadrupolar Coupling constant
CSA	Chemical Shift Anisotropy
CT	Central Transition
DFT	Density Functional Theory
EFG	Electric Field Gradient
GGA	Generalized Gradient Approximation
GIAO	Gauge-Including Atomic Orbitals
GIPAW	Gauge Including Projector Augmented Waves
HF	Hartree-Fock
LCAO	Linear Combination of Atomic Orbitals
MAS	Magic-Angle Spinning
$\mathrm{Ni(cod)_2}$	bis(1,5-cyclooctadiene)nickel(0)
$\mathrm{Ni(PPh_3)_4}$	tetrakis(triphenylphosphine)nickel(0)
$\mathrm{Ni[P(OPh)_3]_4}$	tetrakis(triphenylphosphite)nickel(0)
NMR	Nuclear Magnetic Resonance
PAS	Principal Axis System
QZ4P	Quadruple Zeta with four Polarizion function all-electron basis set
RMSD	Root-Mean-Square Deviation
SCF	Self-Consistent Field
SSNMR	Solid-State Nuclear Magnetic Resonance
T_1	Longitudinal relaxation time constant
T_2	Transverse relaxation time constant
TZP	Triple Zeta with one Polarization function basis set
ZORA	Zeroth-Order Regular Approximation

ABSTRACT

Nuclear magnetic resonance (NMR) spectroscopy has proven to be an invaluable tool for the modern chemist, despite being a relatively insensitive spectroscopic technique. However, it is precisely this insensitivity that limits characterization of low-receptivity nuclides, which make up the bulk of transition metal nuclides, in particular. In this work, high-fields were used to collect the first ^{61}Ni solid-state NMR (SSNMR) spectra of diamagnetic nickel compounds, specifically, bis(1,5-cyclooctadiene)nickel(0) (Ni(cod)$_2$), tetrakis(triphenylphosphite)nickel(0) (Ni[P(OPh)$_3$]$_4$), and tetrakis(triphenylphosphine)nickel(0) (Ni(PPh$_3$)$_4$). This was complemented by NMR study of the co-ordinated ligands and ^{61}Ni density functional theory (DFT) computations.

^{61}Ni SSNMR spectra of Ni(cod)$_2$ were used to determine its isotropic chemical shift (δ_{iso} = 965 ± 10 ppm), span (Ω = 1700 ± 50 ppm), skew (κ = -0.15 ± 0.05), quadrupolar coupling constant (C_{Q} = 2.0 ± 0.3 MHz), quadrupolar asymmetry parameter (η = 0.5 ± 0.2), and the relative orientation of the chemical shift and EFG tensors. Solution study of Ni(cod)$_2$ saturated in C_6D_6 yielded a narrow ^{61}Ni signal, and the temperature dependence of $\delta_{\mathrm{iso}}(^{61}\mathrm{Ni})$ was assessed (δ_{iso} being 936.5 ppm at 295 K). The solution is proposed as a secondary chemical shift reference for ^{61}Ni NMR in lieu of the extremely toxic Ni(CO)$_4$ primary reference. For Ni[P(OPh)$_3$]$_4$, ^{61}Ni SSNMR was used to infer the presence of two distinct crystallographic sites and establish ranges for δ_{iso} in the solid state, as well as an upper bound for C_{Q} (3.5 MHz for both sites). For Ni(PPh$_3$)$_4$, fitting provided a δ_{iso} value of 515 ± 10 ppm, Ω of 50 ± 50 ppm, κ of 0.5 ± 0.5, C_{Q} of 0.05 ± 0.01 MHz, and η of 0.0 ± 0.2. Ni(cod)$_2$ was chosen for study as it is a ubiquitous source of nickel(0), used for both further synthesis of nickel(0) compounds and directly as a catalyst. The

study of $Ni[P(OPh)_3]_4$ and $Ni(PPh_3)_4$ demonstrated the utility of ^{61}Ni SSNMR given the lack of a previously reported crystal structure for both and the transient nature of $Ni(PPh_3)_4$ in solution.

The work begins in Chapter 1 by introducing the interactions fundamental to NMR spectroscopy, before moving on to briefly review the field of transition metal nuclide NMR, the chemistry of nickel (with an emphasis on homogeneous catalysis with nickel(0)), and the literature with respect to nickel NMR up to this point. In Chapter 2, the theory and practice of NMR are explained, including solid-state NMR, as well as the basic principles of density functional theory NMR computations. The specific experimental and computational methods of this work are also introduced. Lastly, in Chapter 3 the results are discussed in the context of the concepts presented and literature reviewed, and highlight the use of ^{61}Ni NMR as a means to gain novel information about the chemistry of the compounds studied.

ACKNOWLEDGEMENTS

Firstly, I would like to thank my family: my mother and father, who have worked tirelessly to give me the kind of opportunities they never had, and for their unconditional love and support. Without them neither I, nor this document, would be complete. My sister Natalia also has my eternal gratitude for being a rock of stability in hard times, a great friend in good ones, and ever a fount of wisdom.

The past two years have been an amazing, rewarding, and to be frank, at times exhausting experience, and I have many individuals to acknowledge for helping me along my way. First and foremost, I would like to thank my supervisor Prof. David Bryce for giving me this opportunity, for being always accessible and helpful, for his support, and for being an exceptionally good-natured person. During the course of my Master's program he has been role model in both his professional and personal conduct, and I am grateful to him for taking a chance on me. I would also like to acknowledge the postdoctoral fellows who have shared with me the great wealth of their practical knowledge and experience, namely Drs. César Leroy and Libor Kobera. In my personal estimation, both from my time at the University of Ottawa and in my undergraduate research, the role of postdoctoral fellows as front-line mentors and resources for both incoming and seasoned graduate students is invaluable. I am also grateful to the undergraduate and visiting students I have had the pleasure of meeting, as well as visiting professor Paméla Faure, for broadening my horizons with their diverse backgrounds and personalities. I want to also acknowledge our NMR technicians, Glenn Facey and Eric (Gang) Ye, as well as Victor Terskikh at the National Ultra-high Field NMR Facility for Solids. They provided the technical support and practical advice necessary to get the best possible results out of NMR spectroscopy, allowing me to turn plans, goals, and ideas into real results. Not least of all, I would also like to thank my fellow graduate students in the Bryce group: Scott Southern, Patrick Szell, Ying-Tung Angel Wong, and Collette (Yijue) Xu. Their help, support, and camaraderie are a part of my graduate studies that I will especially miss.

I extend my thanks to the University of Ottawa and indeed the city of Ottawa for being a place where I could develop and grow as a student and as a person. Life and work here has been a transformative experience, and I feel as though I leave having realized goals as an individual that I did not plan or expect to achieve, but that I will nonetheless look back on with a sense of humbled gratitude.

Finally, thank you to my supervisor and examiners for taking the time to read my thesis, for their feedback, and for the opportunity to defend my work before them. My aim was to prepare a document that is both clear and illuminating, and I hope that from the reader’s perspective it is.

STATEMENT OF ORIGINALITY

I certify that the work presented in this thesis is my own. With permission from the publisher, a significant portion of the scientific contribution of this work is based on work published in a peer-reviewed journal. Such material, where reproduced, is with permission from Copyright (2017) The American Chemical Society. Some figures from other sources have been reprinted and adapted to aid the reader in understanding the material presented and are noted as such, with permissions from the respective publisher.

"Probably no one really understands spin on a level much above the technical mathematical rules. Fortunately, it doesn't matter so much. We know the rules for spin and that's enough to be able to exploit the phenomenon."

-Malcolm Levitt

1 INTRODUCTION

From a reductionist perspective, chemistry is the study of ensembles of nuclei and electrons, and their interactions with each other and other fundamental particles. As such, it is useful, from a physical chemistry perspective, to consider the fundamental properties of these constituents of matter. Two of them, rest mass and electric charge, are readily observable on a macroscopic scale. Indeed, the mass and charge of a nucleus, paired with a complementary-charge worth of electrons, is what defines atoms and elements.

Mass especially is a tangible concept. A book is heavier than a feather, and it is not a conceptual stretch to imagine different compositions of atomic building blocks with different spatial rearrangements giving rise to this everyday property. Mass, weight, and density are experientially unique from a human perspective, and thus it seems natural that they scale down to the atomic level.

Electric charge is perhaps a less intuitive property of matter, but it can be argued that electromagnetic interactions are the most significant in terms of their implications for chemistry. Charge is, however, a less intuitive concept than mass. While it manifests on the scale of human experience, for the most part matter is composed of an equal amount of positive and negative charges, and thus electric charge is usually only observed on the macroscale when one applies a perturbation to a substance. Nonetheless, given the ease with which one can demonstrate static charge buildup using a balloon and a cloth, electric charge is a fundamental property of nuclei and electrons that can be encountered in extended form in day-to-day life.

A third property of matter, spin, is an intrinsic form of angular momentum possessed by nuclei and electrons, and, while inaccessible from an everyday perspective, it is nevertheless as important as mass and charge in the way the chemical world is structured. Absent exotic conditions, nuclear and electronic spin states are degenerate in energy and therefore an equal proportion of spins in different states will exist in any bulk substance. Further, the spin of fermions (half-integer spin particles) is essential to the Pauli exclusion principle, which governs atomic and molecular structure (one should also note that for the most part, electron degeneracy pressure is the driving force preventing the ultimate collapse of every star in the universe into a black hole[1]).

Despite the importance of spin angular momentum, in retrospect it was only with the Stern-Gerlach experiment of 1922 that the implications of spin were observed in a laboratory setting. However, the modern chemist is generally well-acquainted with perhaps the most pervasive manifestation of spin, a phenomenon which has broad clinical applications in addition to its chemical utility: nuclear magnetic resonance (NMR). Specifically, nuclear magnetic resonance spectroscopy is ubiquitous in the chemical world, but because of the foreignness of the concept of spin, the field itself can often come across as inaccessible on a deeper level without specialist training. Fortunately, this same inaccessibility has also led to a preponderance of models and analogies for explaining NMR spectroscopy.

1.1 Nuclear Magnetic Resonance (NMR) Interactions

NMR spectroscopy is, at its most basic level, an exercise in the measurement of nuclear spin states (and their perturbation). Here the fundamental origins of magnetic resonance and its chemical usefulness will be described, with the mathematics and practical methods for manipulating spins and measuring their response described in the Chapter 2.

1.1.1 The Zeeman Interaction

The degeneracy of spin states precludes the observation of a 'net spin' for a bulk substance. However, in the presence of an applied magnetic field different nuclear spin states acquire different energies because of what is known as the Zeeman interaction. Consider first the case of a single spin-1/2 particle I in an external magnetic field B_0. The energy of the two Zeeman states of a spin-1/2 are given by:

$$E = -\gamma m \hbar B_0 \tag{1-1}$$

where γ is the gyromagnetic ratio of the spin (which is intrinsic to a class of particles, and in the case of NMR, to specific nuclides), m is the spin state itself (± 1/2 for a spin-1/2 particle), and $\hbar$ is the reduced Planck constant. The separation between the energy levels, correspondingly, is:

$$\Delta E = \gamma \hbar B_0 \tag{1-2}$$

or equivalently: $\Delta E = \hbar \omega_0$

[1-3]

where ω_0 is the resonant (Larmor) frequency of the nucleus. This energy separation is usually exceedingly small, and therefore when extrapolating to the macroscopic level the population of states for a sample is governed by the Boltzmann distribution:

$$\frac{N\left(\mathrm{m} = -\frac{1}{2}\right)}{N\left(\mathrm{m} = +\frac{1}{2}\right)} = \mathrm{e}^{-\Delta E/k_B T}$$

[1-4]

where k_B is the Boltzmann constant, T is temperature, and ΔE is given by [1-2] and [1-3]. As a result, the population difference between states is also extremely small. For the most sensitive nuclide (the one with the largest gyromagnetic ratio, the proton (^{1}H)), the difference in population between the spin-up and spin-down states is on the order of one-in-tens-of-thousands, moving toward one-in-millions and one-in-billions for less sensitive spin-1/2 nuclides such as ^{13}C and ^{15}N. Given that only transitions between states are observable spectroscopically, NMR is very insensitive, particularly compared to other spectroscopies. As a result, high magnetic fields are employed to give the best NMR spectra per unit time (to a first approximation); pictorially the separation of energy levels for a spin-1/2 particle as a function of external field strength B_0 is provided in Figure 1.

While it is fundamental to the physics of NMR spectroscopy, the Zeeman interaction on its own provides no chemical information. Treating the Zeeman energy as a Hamiltonian, most chemical information which can be gained from an NMR spectrum stems from other interactions which act as perturbations on the Zeeman Hamiltonian. These other interactions will now be discussed in detail.

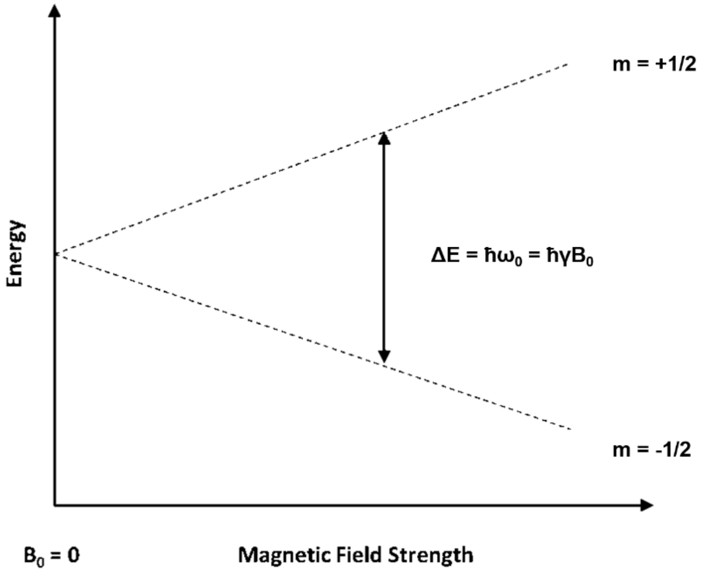

Figure 1: The Zeeman splitting observed for a spin-1/2 nucleus in a magnetic field. The energy of the transition depends on γ (the gyromagnetic ratio of the nucleus), which is an intrinsic property of the nuclide, and the strength of the external field B_0. Neither of these terms provide chemical information, which is derived from other interactions. These other interactions change the energies of the basic Zeeman states and by extension the observed transitions.

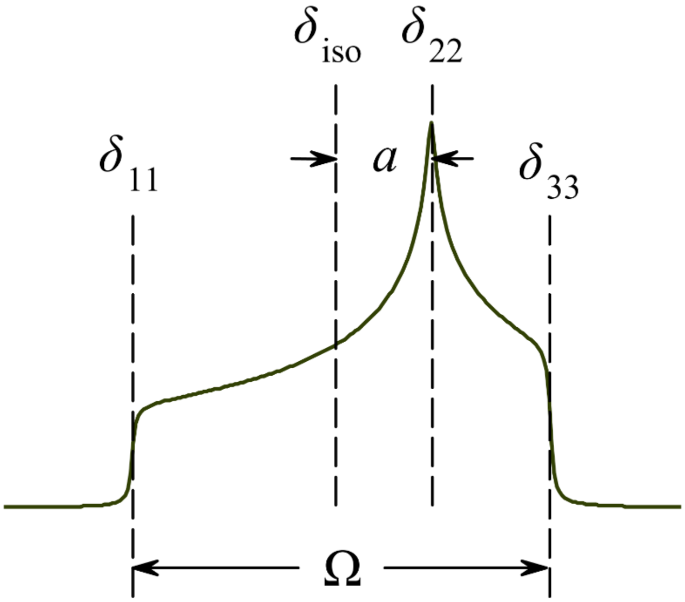

Figure 2: Schematic of the Herzfeld-Berger convention ([1-18], [1-19]) in terms of the principal axis system (PAS) components of the chemical shift tensor, as applied to a solid-state CSA-only NMR spectrum. a is shorthand for $(\delta_{22} - \delta_{\mathrm{iso}})$, which, when divided by the span, provides information about how the spectrum 'skews' ([1-19]) toward the isotropic position.

1.1.2 Magnetic Shielding

Magnetic shielding originates from the interaction of the external magnetic field B_0 with a nucleus, as mediated by electrons. As a result of this, it is a ubiquitous interaction and also a chemically useful one, with the location, density, and behaviour of electrons contributing to a perturbation of the Zeeman Hamiltonian such that different chemical species give NMR signals at different frequencies (energies). Magnetic shielding (σ) can be decomposed into diamagnetic (σ_d) and paramagnetic (σ_p) contributions:[2]

$$\sigma = \sigma_p + \sigma_d \tag{1-5}$$

The diamagnetic term encapsulates circulation of electrons in ground state orbitals, which has the effect of countering the external magnetic field, or 'shielding' the nucleus (decreasing the frequency of the NMR line).[3] Paramagnetic shielding occurs when electrons are promoted from ground state to excited state orbitals by the external magnetic field, which typically 'deshields' nuclei, moving their NMR signals to higher frequencies (i.e. σ_p tends to take negative values).[2,3] The diamagnetic term dominates for ^{1}H (since only the diamagnetic term is non-zero for *s* orbitals)[4], while the paramagnetic term is otherwise usually dominant (although competition between the terms does occur).[4,5]

Further, while magnetic shielding is the fundamental NMR interaction, experimentally only chemical shifts can be recorded. The chemical shift is defined from the magnetic shielding by:

$$\delta = 10^6 \times \frac{\sigma_{\mathrm{ref}} - \sigma}{1 - \sigma_{\mathrm{ref}}} \tag{1-6}$$

where σ_{ref} is the magnetic shielding for the primary chemical shift reference of the nuclide in question. The δ scale is therefore field-independent, with chemical shifts reported in terms of parts per million (ppm) of frequency separation from the primary chemical shift reference.

In understanding magnetic shielding, and other NMR interactions, it is useful to think in terms of the perturbing Hamiltonian associated with the interaction. This Hamiltonian can be written as a product of a nuclear spin operator $\hat{I}$ (for which the component matrices are provided in Appendix I), a second rank Cartesian tensor **A** specific to the interaction, and $\hat{S}$, either a second spin operator or another vector (depending on the interaction):[6]

$$\hat{H} = \hat{I} \cdot \mathbf{A} \cdot \hat{S} \tag{1-7}$$

$$\hat{I} = \begin{bmatrix} \hat{I}_x & \hat{I}_y & \hat{I}_z \end{bmatrix} \tag{1-8}$$

$$\mathbf{A} = \begin{bmatrix} A_{xx} & A_{xy} & A_{xz} \\ A_{yx} & A_{yy} & A_{yz} \\ A_{zx} & A_{zy} & A_{zz} \end{bmatrix} \tag{1-9}$$

The magnetic shielding Hamiltonian is then expressed as:

$$\begin{aligned} \hat{H}_\sigma &= \gamma\left(\hat{I} \cdot \boldsymbol{\sigma} \cdot \hat{B}_0\right) \\ &= \gamma\left(\begin{bmatrix} \hat{I}_x & \hat{I}_y & \hat{I}_z \end{bmatrix} \cdot \begin{bmatrix} \sigma_{xx} & \sigma_{xy} & \sigma_{xz} \\ \sigma_{yx} & \sigma_{yy} & \sigma_{yz} \\ \sigma_{zx} & \sigma_{zy} & \sigma_{zz} \end{bmatrix} \cdot \begin{bmatrix} B_{0,x} \\ B_{0,y} \\ B_{0,z} \end{bmatrix}\right) \\ &= \gamma B_{0,z}\left(\sigma_{xz}\hat{I}_x + \sigma_{yz}\hat{I}_y + \sigma_{zz}\hat{I}_z\right) \end{aligned} \tag{1-10}$$

since B_0 is negligible in the plane perpendicular to the field, compared to the field along the *z* axis.[3,7,8]

By applying the secular approximation, the magnetic shielding Hamiltonian becomes:[6]

$$\hat{H}_\sigma = \gamma B_{0,z}\sigma_{zz}\hat{I}_z \tag{1-11}$$

In order to simplify analysis it is useful to move from the laboratory frame to the fixed principal axis system (PAS) of the molecule experiencing the shielding interaction:

$$\sigma_{zz} = [\sin\theta\cos\varphi \quad \sin\theta\sin\varphi \quad \cos\theta] \cdot \boldsymbol{\sigma}(\mathrm{PAS}) \cdot \begin{bmatrix} \sin\theta\cos\varphi \\ \sin\theta\sin\varphi \\ \cos\theta \end{bmatrix}$$

[1-12]

$$\text{where } \boldsymbol{\sigma}(\mathrm{PAS}) = \begin{bmatrix} \sigma_{11} & 0 & 0 \\ 0 & \sigma_{22} & 0 \\ 0 & 0 & \sigma_{33} \end{bmatrix}$$

[1-13]

where σ_{11} is the component along the *x* axis in the molecular (PAS) frame, and likewise for σ_{22} and σ_{33} along the *y* and *z* axis respectively, θ is the angle of σ_{33} with respect to the external magnetic field, and φ is the angle between σ_{11} and σ_{22} (a constant).[6] This is in essence a rotation operation in the Cartesian coordinate system using a set of Euler angles, with one of the angles defined to be zero.[6,9] Note that by convention $\sigma_{11} \le \sigma_{22} \le \sigma_{33}$.[3,7]

By substituting [1-12] back into [1-11] one can obtain the total magnetic shielding Hamiltonian in terms of the magnetic shielding components in the molecular frame, as observed in the laboratory frame:

$$\widehat{H}_{\sigma} = \gamma B_0(\sigma_{11}(\sin\theta\cos\varphi)^2 + \sigma_{22}(\sin\theta\sin\varphi)^2 + \sigma_{33}(\cos\theta)^2)\hat{I}_z$$

[1-14]

The implication here is that [1-14] is dependent on the angle between the molecule and the applied magnetic field. In solution only the isotropic term (the trace of the magnetic shielding tensor)[3] survives, a result which stems from time-averaging of the angular dependence due to molecular tumbling:[7]

$$\sigma_{\mathrm{iso}} = \frac{1}{3}(\sigma_{11} + \sigma_{22} + \sigma_{33})$$

[1-15]

Powdered solids, on the other hand, can generally be well-approximated as an aggregate of particles with different, random orientations, sampling each possible orientation with equal probability. The result of this is that the NMR signal for a powder is, in general, spread into a manifold of orientation-dependent magnetic shieldings, since the anisotropic component of the magnetic shielding tensor survives (an antisymmetric component can also be described, but is not significant to experimental lineshapes[7]).[3] The powder line shape stemming from chemical shift anisotropy (CSA) is effectively described by the three PAS magnetic shielding components, but, as Figure 2 demonstrates, Herzfeld-Berger notation is often more intuitive in describing the width and symmetry of the powder pattern:

$$\text{Span: } \Omega = \sigma_{33} - \sigma_{11} \tag{1-16}$$

$$\text{Skew: } \kappa = \frac{3(\sigma_{\text{iso}} - \sigma_{22})}{\Omega} \tag{1-17}$$

with σ_{iso} having the same definition as in [1-15].[10] The span and skew can be expressed equivalently in the chemical shift (δ) notation, accounting for the exchange of signs between the scales implied by [1-6]:

$$\Omega = \frac{\sigma_{33} - \sigma_{11}}{1 - \sigma_{\text{ref}}} \approx \delta_{11} - \delta_{33} \tag{1-18}$$

$$\kappa = \frac{3(\delta_{22} - \delta_{\text{iso}})}{\Omega} \tag{1-19}$$

1.1.3 The Quadrupolar Interaction

While the other NMR interactions involve magnetic interactions between nuclear spins and their environment, whether directly or mediated by intermediate charged particles (electrons), the quadrupolar interaction is purely electrostatic. In some cases, the quadrupolar interaction may be so large that it cannot be effectively treated as simply a perturbation on the Zeeman Hamiltonian and instead approaches it in magnitude. Despite this, most practitioners of NMR spectroscopy rarely encounter the quadrupolar interaction directly because it does not exist for spin-1/2 nuclides, which are by far the most commonly observed. To understand why the quadrupolar interaction is only present for $I > 1/2$ nuclides, it is helpful to think of a geometric model of a nucleus. The charge distribution within a nucleus is, to a very good approximation, uniform;[11] the difference in quadrupole moment therefore stems from the shape of the nucleus itself. Spin-1/2 nuclei are spherical, and therefore have no net quadrupole moment.[12] Spin > 1/2 nuclei, on the other hand, can be modelled as prolate or oblate ellipsoids (depending on the nuclide).[12] The distortion from spherical symmetry produces regions where there is effectively more or less positive charge around the nucleus. Keeping in mind that the charge is distributed essentially equally throughout the nucleus, the longer surface of the ellipsoid will be more positively charged (see Figure 3). As a result, while nuclei possess essentially no dipole moment, they can have significant quadrupole moments, depending on the degree of distortion from spherical symmetry.

The quadrupole moment of the nucleus by itself does not produce a quadrupolar coupling; rather, the quadrupole moment interacts with the electric field gradient surrounding the nucleus. The quadrupolar interaction Hamiltonian can be written in terms of the electric field gradient (EFG) and quadrupole moment of the nucleus:

$$\hat{H}_Q = \frac{1}{6}\sum_{a.b} V_{a,b} Q_{a,b}$$

[1-20]

where $Q_{a,b}$ is the electric quadrupole moment of the nucleus and $V_{a,b}$ is the electric field gradient in the direction of a, b (with a and b being x, y or z). Building on the concept of the principal axis system from the discussion of magnetic shielding, it is possible to construct an analogous EFG tensor:[12]

$$\boldsymbol{V}(\text{PAS}) = \begin{bmatrix} V_{11} & 0 & 0 \\ 0 & V_{22} & 0 \\ 0 & 0 & V_{33} \end{bmatrix}$$

[1-21]

Note that unlike the magnetic shielding interaction tensor, only two components can be independent in order for Laplace's equation to be satisfied, which is the requirement that the electric field gradient for a volume in free space be zero:

$$V_{11} + V_{22} + V_{33} = 0$$

[1-22]

This is true in that the electric field gradient experienced by the nucleus is not produced by any charges at the position of the nucleus (i.e. the nucleus is treated as a test charge in a region of empty space containing an externally generated electric field gradient). It is necessary to note that the principal axis system for the quadrupolar interaction is not necessarily the same as for the magnetic shielding interaction. Rotation between the two is accomplished through a set of Euler angles (α, β, γ). Also, by convention $|V_{33}| \geq |V_{22}| \geq |V_{11}|$.[12]

Practically speaking, inclusion of angular momentum terms in the quadrupolar interaction Hamiltonian [1-20] yields a quadrupolar Hamiltonian in the principal axis system which is more readily applicable to NMR discussions:

$$\widehat{H}_{\mathrm{Q}} = \frac{eQ}{6I(2I-1)}\left[V_{11}\left(3\hat{I}_X^2 - I^2\right) + V_{22}\left(3\hat{I}_y^2 - I^2\right) + V_{33}\left(3\hat{I}_z^2 - I^2\right)\right]$$

[1-23]

where *e* is the elementary charge, *Q* is the nuclear electric quadrupole moment, $\hat{I}_{x,y,z}$ are angular momentum operators (Appendix I), and *I* is the spin of the nuclide.[4] By expanding and simplifying it is possible to show that this Hamiltonian is equivalent to:[4]

$$\widehat{H}_Q = \frac{eQ}{4I(2I-1)}V_{33}\left[\left(3\hat{I}_Z^2 - I^2\right) + \eta\left(\hat{I}_x^2 - \hat{I}_y^2\right)\right]$$

[1-24]

where η is the quadrupolar asymmetry parameter:

$$\eta = \frac{V_{11} - V_{22}}{V_{33}}$$

[1-25]

Applying this Hamiltonian to the Zeeman Hamiltonian gives the first- and second-order quadrupolar perturbations to the Zeeman energy levels:

$${\hat{E}_m}^{(1)} = \frac{eQV_{33}}{4I(2I-1)}\left\{\frac{1}{2}(3\cos^2\theta - 1) + \frac{\eta}{2}\sin^2\theta\cos(2\varphi)\right\}\{3m^2 - I(I+1)\}$$

[1-26]

$$\begin{aligned}{\hat{E}_m}^{(2)} = -\left(\frac{eQV_{33}}{4I(2I-1)}\right)^2\left\{\frac{m}{\omega_0}\right\}\Bigg\{&-\frac{1}{5}(I(I+1) - 3m^2)(3+\eta^2) \\ &+ \frac{1}{28}(8I(I+1) - 12m^2 - 3)[(\eta^2 - 3)(3\cos^2\theta - 1) + 6\eta\sin^2\theta\cos(2\varphi)] \\ &+ \frac{1}{8}(18I(I+1) - 34m^2 - 5)\left[\frac{1}{140}(18+\eta^2)(35\cos^4\theta - 30\cos^2\theta + 3)\right. \\ &\left. + \frac{3}{7}\eta\sin^2\theta\,(7\cos^2\theta - 1)\cos(2\varphi) + \frac{1}{4}\eta^2\sin^4\theta\cos(4\varphi)\right]\Bigg\}\end{aligned}$$

[1-27]

where θ is the angle between V_{33} and B_0, and φ is the angle between V_{11} and V_{22} (a constant).[12] While the second order correction is not important for other interactions, it can be significant in the case of quadrupolar coupling due to the potential magnitude of the interaction. The effects of the first- and second-order quadrupolar perturbations to Zeeman states are shown schematically for a spin-3/2 nuclide (such as ^{35}Cl and ^{61}Ni) in Figure 4.

In addition to the asymmetry parameter, it is often useful to also give the quadrupolar coupling constant instead of individual components of the interaction tensor:

$$C_{\mathrm{Q}} = \frac{eQV_{33}}{\hbar} \tag{1-28}$$

The quadrupolar coupling constant can then be incorporated as a simplification into previous equations.

In practical terms, the second-order quadrupolar coupling constant causes a deviation of the central (m = -1/2 → m = +1/2) transition from its Zeeman value (i.e. causing a shift in its isotropic value), which is dependent on the overall strength of the interaction. The magnitude of the second-order quadrupolar shift is given by:[13]

$$\Delta\nu_{m,m-1} = -\frac{3}{40}\left(\frac{{C_{\mathrm{Q}}}^2}{{\omega_0}^2}\right)\frac{(I(I+1) - 9m(m-1) - 3)}{I^2(2I-1)^2}\left(1 + \frac{1}{3}\eta^2\right) \tag{1-29}$$

The first-order quadrupolar interaction significantly changes the energy separation of the satellite transitions (m = -3/2 → -1/2 and m = +1/2 → +3/2, for I = 3/2), causing multiple lines to appear in an NMR spectrum. Again, the energy (frequency) of these transitions in an NMR spectrum depends on the strength of the quadrupolar interaction; as a practical matter, satellite transitions are not observed in NMR spectra for all but highly symmetric (low C_{Q}) sites. The reason for this is that in solution the orientation dependence of the first-order Hamiltonian results in its

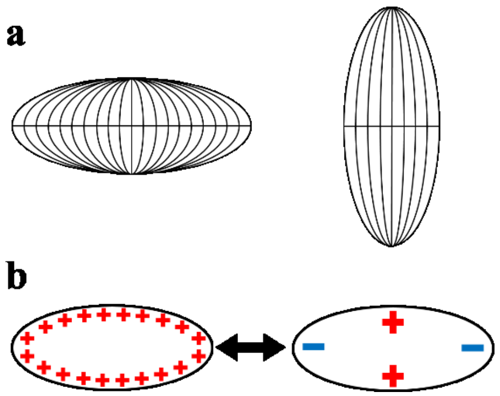

Figure 3: a) Quadrupolar nuclei can be oblate (‘flattened’, left) or prolate (‘elongated’, right) ellipsoids. b) The ellipsoidal geometry of a quadrupolar nucleus combined with its uniform charge distribution has the effect of producing localized regions where the charge density on the surface is apparently greater or lesser than the average for the volume. The charge relative to the average can be treated as positive or negative respectively, so that the emergence of a quadrupole moment is readily apparent.

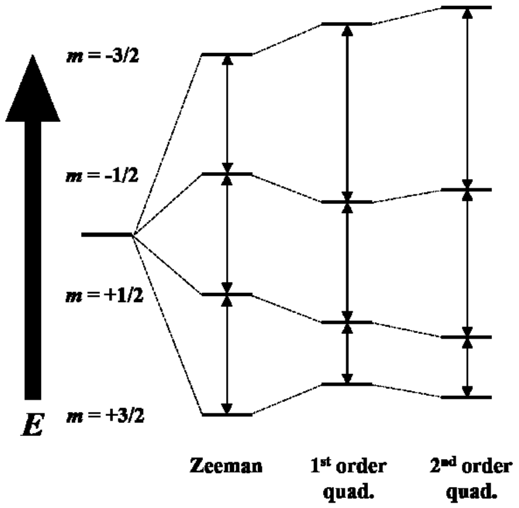

Figure 4: The energy levels for a spin-3/2 nucleus in an external magnetic field. The first-order quadrupolar coupling decreases the energy of the central $m = \pm 1/2$ levels and increases the energy of the $m = \pm 3/2$ levels, removing the degeneracy in the transition energies. The second-order interaction changes the separation between the central $m = \pm 1/2$ states, causing what is known as the second-order quadrupolar shift.

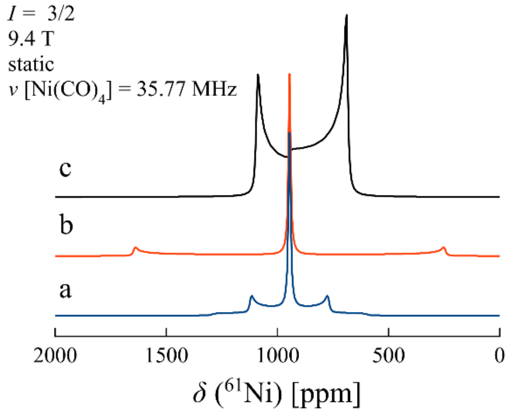

Figure 5: Simulation of the powder pattern for a purely quadrupolar interaction for a hypothetical nickel-61 (spin-3/2) sample. From a) C_Q = 25 kHz to b) C_Q = 100 kHz one can see how quickly the satellite transition energies change under quadrupolar coupling. By c) C_Q = 2.0 MHz, the satellite transitions are outside the spectral window and the central transition itself exhibits significant broadening (relative intensities of simulations not to scale).

averaging out, while in powdered solids the orientation-dependent first-order quadrupolar Hamiltonian produces a powder pattern, spreading its intensity over a wide area of the spectrum (akin to what was discussed with magnetic shielding). The central transition (CT) produces a much narrower line by comparison and is therefore much more intense (Figure 5). The equation for the width of a purely quadrupolar static central transition is given as:

$$\Delta\nu_{\mathrm{CT}} = \frac{9}{4}\frac{C_{\mathrm{Q}}{}^2}{\nu_0}\frac{I(I+1)-\frac{3}{4}}{I^2(2I-1)^2}\left(\frac{25+22\eta+\eta^2}{6}\right)$$

[1-30]

The quadrupolar interaction can complicate even solution acquisition due to relaxation-induced line broadening, as it is an extremely efficient means of nuclear relaxation. It will be discussed in that context later in this work (Section 2.1.1.5).

1.1.4 Indirect Spin-Spin (J) Coupling

A third NMR interaction stems from coupling between nuclear spins as mediated by intervening electrons, and hence is known as indirect spin-spin coupling (also as *J* coupling). Because indirect spin-spin coupling involves electrons it is a source of great chemical information, depending on electronic structure and behaviour through the bonding network of a compound. The Hamiltonian, correspondingly, consists of a pair of spins connected through the *J* coupling tensor:[14]

$$\hat{H}_J = h\,\hat{I}_1 \cdot \boldsymbol{J} \cdot \hat{I}_2$$

[1-31]

The *J* coupling tensor in its principal axis system is structurally analogous to the PAS magnetic shielding tensor:[7]

$$\boldsymbol{J}(PAS) = \begin{bmatrix} J_{11} & 0 & 0 \\ 0 & J_{22} & 0 \\ 0 & 0 & J_{33} \end{bmatrix}$$

[1-32]

The *J* coupling tensor itself can be approximated as the trace of the matrix, as the anisotropic component is small and masked by direct spin-spin coupling (and the antisymmetric component has limited effect on experimental spectra):[15]

$$\boldsymbol{J} \approx J_{\text{iso}} = \frac{1}{3}(J_{11} + J_{22} + J_{33})$$

[1-33]

This simplifies the *J* coupling Hamiltonian to:

$$\widehat{H}_J = h\, J_{\text{iso}}\, \hat{I}_1 \cdot \hat{I}_2$$

[1-34]

Note that this is unlike the magnetic shielding case, as the anisotropic component of the *J* coupling tensor is not generally observed in either solution or the solid state, leading to the misleading moniker of ‘scalar coupling’. The indirect dipole-dipole interaction is nevertheless a tensor quantity.

1.1.5 Direct Spin-Spin (Dipolar) Coupling

Lastly, since nuclei themselves possess magnetic moments they can also interact directly through space. The direct spin-spin coupling Hamiltonian stems from the classical equation for the interaction of magnetic dipoles:

$$E = \left(\frac{\mu_0}{4\pi}\right)\left[\frac{\boldsymbol{\mu_1} \cdot \boldsymbol{\mu_2}}{r^3} - \frac{3(\boldsymbol{\mu_1} \cdot \boldsymbol{r})(\boldsymbol{\mu_2} \cdot \boldsymbol{r})}{r^5}\right]$$

[1-35]

where μ_0 is the vacuum permeability constant, $\boldsymbol{\mu}$ is the magnetic moment of the indicated nucleus, $\boldsymbol{r}$ is the internuclear vector, and r is the magnitude of the internuclear vector. Substituting in the quantum mechanical definition of the magnetic moment:

$$\boldsymbol{\mu} = \gamma\hbar\hat{I}$$

[1-36]

$$\widehat{H}_{DD} = (\gamma_1\gamma_2\hbar^2)\left(\frac{\mu_0}{4\pi}\right)\left[\frac{\hat{I}_1 \cdot \hat{I}_2}{r^3} - \frac{3(\hat{I}_1 \cdot \boldsymbol{r})(\hat{I}_2 \cdot \boldsymbol{r})}{r^5}\right]$$

[1-37]

By expanding the spin matrices into their components, it is possible to arrive at an equation of similar form to the other NMR interaction Hamiltonians:

$$\widehat{H}_{DD} = hR\left(\begin{bmatrix}\hat{I}_{1,x} & \hat{I}_{1,y} & \hat{I}_{1,z}\end{bmatrix} \cdot \begin{bmatrix}(r^2 - 3x^2)/r^2 & -3xy/r^2 & -3xz/r^2 \\ -3xy/r^2 & (r^2 - 3y^2)/r^2 & -3yz/r^2 \\ -3x^2/r^2 & -3y^2/r^2 & (r^2 - 3z^2)/r^2\end{bmatrix} \cdot \begin{bmatrix}\hat{I}_{2,x} \\ \hat{I}_{2,y} \\ \hat{I}_{2,z}\end{bmatrix}\right)$$

[1-38]

$$\widehat{H}_{DD} = hR\,(\hat{I}_1 \cdot \boldsymbol{D} \cdot \hat{I}_2)$$

[1-39]

with the constant *R* subsuming the other constant terms:

$$R = \frac{(\gamma_1\gamma_2)}{r^3}\frac{\hbar}{2\pi}\left(\frac{\mu_0}{4\pi}\right)$$

[1-40]

Rearranging to the familiar form allows for further expansion and simplification, given that the internuclear vector in the principal axis system of the dipolar interaction is defined to lie along the *z* axis (i.e. the *x* and *y* components of the displacement are zero):

$$\boldsymbol{D}(PAS) = \begin{bmatrix}1 & 0 & 0 \\ 0 & 1 & 0 \\ 0 & 0 & -2\end{bmatrix}$$

[1-41]

$$\hat{H}_{DD} = hR\,(\hat{I}_1 \cdot \begin{bmatrix} 1 & 0 & 0 \\ 0 & 1 & 0 \\ 0 & 0 & -2 \end{bmatrix} \cdot \hat{I}_2)$$

[1-42]

Two significant results are immediately apparent from the form of the dipolar coupling interaction tensor: firstly, under isotropic averaging the dipolar interaction is only observable through its effect on relaxation (since the interaction tensor is traceless), and secondly the interaction Hamiltonian is directly dependent on the distance between two spins (which means NMR can be used as a 'molecular ruler' to extract structural information). The interaction Hamiltonians will take different forms depending on whether the two spins are of the same nuclide (homonuclear) or different nuclides (heteronuclear):[16]

$$\hat{H}_{DD}(\text{homonuclear}) = hR\left(\frac{1 - 3\cos^2\theta}{2}\right)\left(3\hat{I}_{1,z}\hat{I}_{2,z} - \hat{I}_1\hat{I}_2\right)$$

[1-43]

$$\hat{H}_{DD}(\text{heteronuclear}) = hR(1 - 3\cos^2\theta)(\hat{I}_{1,z}\hat{I}_{2,z})$$

[1-44]

Nonetheless, because of the gyromagnetic ratio dependence (and field independence) of dipolar coupling, it can be very difficult to observe for insensitive nuclides, as in the solid state (where dipolar coupling can be directly observed) the CSA and quadrupolar interaction (where applicable) tend to mask the direct dipolar coupling.[17]

1.2 NMR of Transition Metal Nuclides

As was mentioned, NMR is an inherently insensitive technique due to the small difference in populations between the states involved. The sensitivity of an NMR experiment is also heavily dependent on the presence and magnitude of NMR interactions, as these can cause broadening and/or splitting of signal. Therefore, experimental times and practicability can vary dramatically even for a single nuclide. Nevertheless, the character of the nuclide itself is also significant, and for many nuclides no experimental NMR results of any kind have been obtained. Factors determining the difficulty of experiments with a particular nuclide will now be discussed, with a focus on the Group 10 elements and other transition metal nuclides.

1.2.1 Spin-1/2 Nuclides

It is helpful to first introduce the concept of receptivity, which is an ‘all-else-being-equal’ comparison of sensitivity between nuclides. Receptivity is defined relative to the most receptive nuclide, the proton:

$$R^{\mathrm{X}} = \frac{|\gamma_{\mathrm{X}}{}^{3}|A_{\mathrm{X}}I_{\mathrm{X}}(I_{\mathrm{X}}+1)}{\left(\frac{3}{4}\right)|\gamma_{^{1}\mathrm{H}}{}^{3}|A_{^{1}\mathrm{H}}}$$

[1-45]

where γ is the gyromagnetic ratio, A the natural abundance, and I the spin number of nuclide X and ^{1}H respectively.[18] From this equation, the technical difference between sensitivity and receptivity is apparent: a nuclide can be inherently sensitive, but due to low natural abundance can have a low receptivity. However, one should note the cubic dependence on the gyromagnetic ratio, which limits the benefits that can be gained for low-sensitivity nuclides simply by isotopically enriching them. Consider for example the difference between ^{57}Fe and the more familiar ^{13}C: ^{57}Fe is almost twice as abundant as ^{13}C (2.119% against 1.07%), but with a gyromagnetic ratio eight times smaller than ^{13}C (0.868×10^{7} rad·s^{-1}·T^{-1} versus 6.728×10^{7} rad·s^{-1}·T^{-}

^{1}),[19] iron-57 NMR must deal with a decrease in receptivity relative to carbon-13 NMR of almost 235 times, significantly limiting work with this nuclide (among other reasons). Table 1 provides NMR relevant properties of some of the more commonly observed spin-1/2 nuclides, as well as all spin-1/2 transition metal nuclides. Most of these transition metal nuclides suffer from low natural abundance, low sensitivity, or both; however, ^{113}Cd, ^{199}Hg, and, in particular, ^{195}Pt are all more receptive than ^{13}C. ^{195}Pt NMR, therefore, is an ideal case within Group 10 to showcase the benefits of directly detecting metal centers by NMR spectroscopy, as opposed to relying only on the NMR of more sensitive or chemically ubiquitous co-ordinating ligand heteronuclei.

^{195}Pt NMR is routinely used for platinum containing samples, thanks in large part to the favourable NMR properties of ^{195}Pt (including a receptivity 20.7 times that of ^{13}C, a natural abundance of 33.8%, and a gyromagnetic ratio of 5.84×10^{7} rad·s^{-1}·T^{-1}), but also because of its broad chemical shift range of 16000 ppm (compared to 300 ppm for ^{13}C and 15 ppm for ^{1}H NMR of diamagnetic species).[5,20] ^{195}Pt NMR isotropic chemical shifts (δ_{iso}) are, as a result, particularly sensitive to molecular composition, conformation, environment and temperature, with shifts of 100 ppm routinely observed upon ligand substitution.[5,20] For platinum-195, magnetic shieldings (and likewise chemical shifts) are dominated by the paramagnetic term due to low lying excited electronic states, but a spin-orbit coupling term must be added to the magnetic shielding equation [1-5] to account for relativistic effects observed in heavy transition metal atoms.[5] The δ_{iso} values for ^{195}Pt NMR have been well studied in solution, with chemical shift ranges strongly dependent on oxidation state.[5] The bulk of work focuses on Pt(II) compounds, which exhibit substantial chemical shift dependence on the *cis-*/*trans-* isomerism of the complex, though work has also been done on Pt(III) (primarily binuclear species), Pt(IV),

Table 1: NMR properties of some commonly observed spin-1/2 nuclides, and the spin-1/2 transition metal nuclides. Nuclides of particular interest to this work are highlighted in boldface. Where multiple isotopes exist for an element, ones less suitable for NMR are given in parentheses. Values are adapted from reference 19.

Nuclide	Natural abundance [%]	$R^{C\ a}$	γ [10^7 rad s^{-1} T^{-1}]^b	Ξ^c
^{1}H	**99.9885**	**5.87×10^3**	**26.752 2128**	**1.000 000 00**
^{13}C	**1.07**	**1.00**	**6.728 284**	**0.251 450 20**
^{15}N	0.368	2.25×10^{-2}	-2.712 618 04	0.101 367 67
^{19}F	100	4.90×10^3	25.181 48	0.940 940 11
^{31}P	**100**	**3.91×10^2**	**10.8394**	**0.404 807 42**
^{57}Fe	2.119	4.25×10^{-3}	0.868 0624	0.032 377 78
^{89}Y	100	0.700	-1.316 2791	0.049 001 98
^{103}Rh	100	0.186	-0.8468	0.031 864 47
(^{107}Ag)	51.839	0.205	-1.088 9181	0.040 478 19
^{109}Ag	48.161	0.290	-1.251 8634	0.046 535 33
(^{111}Cd)	12.80	7.27	-5.698 3131	0.212 154 80
^{113}Cd	12.22	7.94	-5.960 9155	0.221 931 75
^{183}W	14.31	6.31×10^{-2}	1.128 2403	0.041 663 87
^{187}Os	1.96	1.43×10^{-3}	0.619 2895	0.022 823 31
^{195}Pt	**33.832**	**20.7**	**5.8385**	**0.214 967 84**
^{199}Hg	16.87	5.89	4.845 7916	0.179 108 22

[a] Receptivity versus ^{13}C at natural abundance
[b] Gyromagnetic ratio
[c] Frequency factor (relative to 1.000 000 00 for ^{1}H)

and Pt(0).[5] In particular, Pt(0) platinum-195 chemical shifts for Pt(cod)$_2$,[21] Pt(PMe$_3$)$_4$ and Pt(PPh$_3$)$_4$,[22] and Pt[P(OMe)$_3$]$_4$[23] do not follow the same trends exhibited in ^{61}Ni chemical shifts of analogous nickel compounds, which will be discussed later in the text. Apart from chemical shifts, *J* couplings measured in solution by ^{195}Pt NMR can be useful for structural and chemical characterization due to their size: one-bond couplings can be in the range of thousands of hertz for ^{1}H, ^{31}P, ^{119}Sn, and ^{205}Tl, reaching above 50 kHz for $^{1}J(^{195}\mathrm{Pt}\text{-}^{205}\mathrm{Tl})$. Multiple bond couplings are also routinely observed, including between ^{195}Pt nuclei themselves.[5] As with chemical shifts, *J* coupling is also sensitive to *cis-*/*trans-* isomerism, as often seen for $^2J(^{195}\text{Pt}-^{13}\text{C})$ couplings (which are usually on the order of tens of hertz).[5] Measurement of connectivity in non-equivalent platinum clusters is an application of the information gained by *J* coupling measurement.[20]

Given the interest in platinum as a catalyst for a host of commercial and industrial processes, much work has also been done recently to characterize platinum and platinum compounds in the solid state. Nanoparticles, consisting of Pt, Pt-Sn, and Pt_3X (where X = Al, Sc, Nb, Ti, Hf, and Zr) have been studied by ^{195}Pt solid-state (SS)NMR.[24] The spectra for elemental platinum nanoparticles have been deconvoluted to separate and quantify the platinum content and size of different layers of the nanoparticle.[24] Other recent solid-state results include using ^{195}Pt NMR as a component for holistic characterization of phosphanido-bridged diplatinum complexes,[25] and coupling sensitivity enhancement techniques (specifically dynamic nuclear polarization) with ^{195}Pt wideline NMR spectroscopy to study metal-organic frameworks[26].

Other spin-1/2 transition metal nuclides will not be discussed in detail here. Broadly speaking, they behave similarly to ^{195}Pt, with notable differences in results primarily ensuing from differences in chemical behaviour, receptivity (with *J* coupling as well as sensitivity depending on γ), and paramagnetism. The latter property in particular can have significant detrimental effects on NMR spectra. For compounds with unpaired electrons, multiple nuclear-electronic interactions can occur, including the Fermi contact shift (FCS) and pseudocontact shift (PCS; the former being a ‘through-bond’ interaction and the latter being a ‘through-space’ interaction), both of which result in chemical shifts that can be thousands of ppm outside the diamagnetic chemical shift range.[27,28] In addition to the broad chemical shift range which can be induced by paramagnetic interactions, spectral broadening can occur due to anisotropy in the paramagnetic shift interaction (PSA, which is primarily a solid-state effect) and paramagnetic relaxation enhancement (PRE), which can induce rapid relaxation that hinders observation by broadening lines.[27] As will be discussed in the Chapter 2, rapid relaxation, caused by the quadrupolar interaction or PRE for instance, results in spectral broadening due to the inverse relationship between the time domain of acquisition and frequency domain of NMR spectra. For these reasons, NMR spectroscopy, particularly for insensitive nuclides, is generally pointedly easier for diamagnetic chemical species (although in bulk metals or alloys the sheer number of spins can compensate for broadening).

1.2.2 Quadrupolar Nuclides

The focus now turns to quadrupolar transition metal nuclides, which have similar difficulties as the spin-1/2 transition metal nuclides, but with the added complication of the quadrupolar interaction. In general, there are four main subgroups of quadrupolar transition metal nuclides, separated by the difficulty in performing NMR with the specific nuclear properties of the nuclide, the particulars of the element's chemistry, accessible diamagnetic oxidation states, and other, more peculiar issues that will be discussed. The NMR properties of all the quadrupolar nuclides discussed here are included in Table 2.

Firstly, a combination of factors have severely limited observation to date of hafnium and iridium (with two NMR active isotopes each), gold (with one active isotope), and mercury-201 (mercury does however possess a spin-1/2 isotope with relatively favourable NMR properties).[29] None of these nuclides have been observed in solution, and solid state results are almost exclusively limited to Knight shift (K_{iso}) studies of the metals and indirect detection.[29]

A second group of nuclei are well-studied, in solution as well as the solid state. Vanadium has two nuclides, ^{50}V and ^{51}V. Both are NMR active, but the primary nuclide of study is ^{51}V due to its overwhelmingly higher natural abundance, higher gyromagnetic ratio, and smaller quadrupole moment.[30] Trends in NMR parameters stemming from electronics and sterics, solvent effects, temperature, and coordination have been well documented, and reviews exist on the subject.[30,31] Vanadium (particularly vanadium oxides) has also been well characterized in the solid state. Cobalt has one, spin-7/2, isotope with a relatively high gyromagnetic ratio but a more substantial quadrupole moment compared to vanadium-51.[19,32] Cobalt-59 NMR is complicated to a greater extent by its chemistry, with the most prevalent cobalt(II) oxidation state being paramagnetic, but has nevertheless developed a substantial literature. Molybdenum-95 is preferred over molybdenum-97; though both have low gyromagnetic ratios (and hence sensitivity), their receptivity, while much lower than the rest of the nuclides discussed here, is still three times larger than for carbon-13.[19] The relatively smaller quadrupole moment of molybdenum-95 compared to the other well-documented quadrupolar transition metal nuclides aids in solution study, and, like vanadium-51, ^{95}Mo chemical shifts are sensitive to isotopic substitution in complexes.[29] Scandium-45 has a high receptivity and moderate quadrupole moment.[19,32] It tends to produce broad lines in solution, but has been well-documented in the solid state, despite the relative paucity of scandium coordination complexes. Zirconium-91 has a receptivity six times larger than ^{13}C and a quadrupole moment similar to the more thoroughly studied ^{59}Co. It is ultimately rather surprising that more work has not been reported with zirconium; while the quadrupole moment makes solution observation non-trivial, more has been done with cobalt. Further, although solid-state magic-angle spinning (MAS) NMR studies (Section 2.1.2.1) typically use zirconia rotors, it is no great difficulty to procure rotors made of, for example, silicon nitride, to allow for NMR study of zirconium. Lastly, niobium-93 possesses a significant quadrupole moment, but nonetheless some chemically useful information can be gained from chemical shifts and *J* coupling constants in solution,[29] and a number of solid-state studies have been reported in the literature.

Third is the group of nuclides which have reasonable NMR sensitivity but which do not have a deeply developed literature for other reasons. Titanium has two NMR active isotopes, ^{47}Ti and ^{49}Ti, but the resonant frequencies are separated by only 267 ppm, leading to issues with overlapping resonances.[29] Separation of resonances, particularly of solid-state wideline spectra, is possible but not trivial.[33] Manganese has one stable isotope, which is NMR active, with a high receptivity but comparably large quadrupole moment.[19,32] Unfortunately, ^{55}Mn NMR is limited by the fact that manganese has more stable oxidation states than any other transition metal, but only the +1, 0, and -1 states are diamagnetic.[29] Copper has two stable isotopes, both spin-3/2 and with similar quadrupole moments.[19,32] Despite ^{63}Cu being 69.1% abundant, ^{65}Cu is preferred due to its larger receptivity. However, like manganese, oxidation states are an issue, with high-symmetry structures mostly confined to the Cu(I) oxidation state.[29] Technetium-99 is sensitive and synthetically produced (so is always at 100% abundance) but radioactivity presents an issue for all but highly specialized research groups.[29] Lanthanum has two isotopes, but ^{138}La is only 0.089% abundant and has a larger quadrupole moment than ^{139}La.[19,32] While some solid-state studies have been published, organometallic lanthanum chemistry is limited and thus NMR of the element is likewise limited.

Finally, there is a group of transition metals which have quadrupolar isotopes with poor overall NMR suitability. Included in this group are chromium, nickel, zinc, palladium, tantalum, rhenium, osmium, and ruthenium. The ^{53}Cr nuclide, which is the only active nuclide of chromium, has a similar quadrupole moment and is eight times more abundant while having only three-fifths of the gyromagnetic ratio of nickel-61.[19,32] Chromium-53 is therefore actually less receptive than ^{61}Ni, but thanks to the diamagnetic nature of its most dominant oxidation states, has been previously characterized in at least two SSNMR studies.[34,35] The NMR properties of nickel-61 itself are summarized in Table 2, and the particulars of nickel chemistry and NMR will be discussed in detail in the following sections. Apart from ^{61}Ni and ^{195}Pt, ^{105}Pd is the only other NMR-active nuclide in Group 10. It is an essentially uncharacterized nuclide, with a problematic quadrupole moment (0.660×10^{-28} m^2), extremely low gyromagnetic ratio (-1.23×10^{7} rad·s^{-1}·T^{-1}), and middling natural abundance (22.33%). The body of work involving this nuclide is thoroughly underwhelming, with indirect coupling to phosphorus,[36] Knight shift studies,[37,38] and one solution NMR report forming the whole of the literature.[39] Tantalum-181, despite being very receptive, is endowed with a truly massive quadrupole moment.[19,32] The two rhenium isotopes (^{185}Re and ^{187}Re) are similarly hindered, and are also extremely close in resonance frequency, leading to overlap issues similar to those observed for titanium NMR.[19,32,40] Osmium-189 NMR is likewise hampered by the large quadrupole moment of the nuclide (spin-1/2 osmium-187, on the other hand, is the least receptive nuclide in the periodic table), while both ruthenium isotopes suffer from very small gyromagnetic ratios, with the more abundant ^{101}Ru also possessing a significant quadrupole moment.[19,32]

Sulfur-33, while not a transition metal nuclide, is a useful yardstick for anticipating the difficulties of ^{61}Ni NMR. Compared to chromium-53, ^{33}S has a gyromagnetic ratio and natural abundance (Table 2) much closer to nickel-61 (although the quadrupole moment of sulfur-33 is lower than either metal nuclide).[19,32] Therefore, given the difficulty in acquiring the NMR spectrum of a low-symmetry species such as S_8,[41] one would expect that the task would be even more impractical for nickel-61 NMR and that high symmetry sites (with their incipient small quadrupolar couplings) are required to attain solid-state nickel NMR spectra in reasonable timeframes at present. Indeed, the comparative ease of ^{33}S SSNMR characterization of inorganic sulfides[42] would suggest that ^{61}Ni SSNMR of highly-symmetric species should be a reasonable prospect.

Table 2: NMR properties of the quadrupolar transition metal nuclides, with nuclides of particular interest highlighted in boldface. Where multiple isotopes exist for an element, ones less suitable for NMR are given in parentheses. Sulfur-33 is included thanks to its gyromagnetic ratio and natural abundance, which are similar to nickel-61. The chlorine nuclides are included as a result of their utility in the experimental setup of nickel experiments (see Section 2.3.1). Values are adapted from reference 19, with quadrupole moments from 32.

Nuclide	*I*	Natural abundance [%]	$R^{C\ a}$	Q [10^{-30} m^2]^b	γ [10^7 rad s^{-1} T^{-1}]^c	Ξ^d
^{33}S	**3/2**	**0.76**	**0.101**	**-6.78**	**2.055 685**	**0.076 760 00**
^{35}Cl	**3/2**	**75.78**	**21.0**	**-8.165**	**2.624 198**	**0.097 979 09**
^{37}Cl	**3/2**	**24.22**	**3.87**	**-6.435**	**2.184 368**	**0.081 557 25**
^{45}Sc	7/2	100	1.78×10^3	-22.0	6.508 7973	0.242 917 47
^{47}Ti	5/2	7.44	0.918	30.2	-1.5105	0.056 375 34
^{49}Ti	7/2	5.41	1.20	24.7	-1.510 95	0.056 390 37
(^{50}V)	6	0.250	0.818	21.0	2.670 6490	0.099 703 09
^{51}V	7/2	99.750	2.25×10^3	-5.2	7.045 5117	0.263 029 48
^{53}Cr	**3/2**	**9.501**	**0.507**	**-15.0**	**-1.5152**	**0.056 524 96**
^{55}Mn	5/2	100	1.05×10^3	33.0	6.645 2546	0.247 892 18
^{59}Co	7/2	100	1.64×10^3	42.0	6.332	0.237 270 74
^{61}Ni	**3/2**	**1.1399**	**0.240**	**16.2**	**-2.3948**	**0.089 360 51**
^{63}Cu	3/2	69.17	3.82×10^2	-22.0	7.111 7890	0.265 154 73
^{65}Cu	3/2	30.83	2.08×10^2	-20.4	7.604 35	0.284 036 93
^{67}Zn	5/2	4.10	0.692	15.0	1.676 688	0.062 568 03
^{91}Zr	**5/2**	**11.22**	**6.26**	**-17.6**	**-2.497 43**	**0.092 962 98**
^{93}Nb	9/2	100	2.87×10^3	-32.0	6.5674	0.244 761 70
^{95}Mo	5/2	15.92	3.06	-2.2	-1.751	0.065 159 26
(^{97}Mo)	5/2	9.55	1.95	25.5	-1.788	0.066 536 95
^{99}Tc	9/2	–	–	-12.9	6.046	0.225 083 26

Nuclide	I	Natural abundance [%]	R^{C} [a]	Q [10^{-30} m^2] [b]	γ [10^7 rad s^{-1} T^{-1}] [c]	Ξ [d]
^{101}Ru	5/2	17.06	1.59	45.7	-1.377	0.051 613 69
^{105}Pd	**5/2**	**22.33**	**1.49**	**66.0**	**-1.23**	**0.045 761 00**
^{138}La	5	0.090	0.497	45.0	3.557 239	0.131 943 00
^{139}La	7/2	99.910	3.56×10^2	20.0	3.808 3318	0.141 256 41
^{177}Hf	7/2	18.60	1.54	336.5	1.086	0.040 07[e]
^{179}Hf	9/2	13.62	0.438	379.3	-0.6821	0.025 17[e]
^{181}Ta	7/2	99.988	2.20×10^2	317.0	3.2438	0.119 896 00
(^{185}Re)	5/2	3.7710	3.05×10^2	218.0	6.1057	0.225 246 00
^{187}Re	5/2	3.8096	5.26×10^2	207.0	6.1682	0.227 516 00
^{189}Os	3/2	16.15	2.32	85.6	2.107 13	0.077 654 00
(^{191}Ir)	3/2	37.3	6.38×10^{-2}	81.6	0.4812	0.017 18[e]
^{193}Ir	3/2	62.7	0.137	75.1	0.5227	0.018 71[e]
^{197}Au	3/2	100	0.162	54.7	0.473 060	0.017 29[e]
^{201}Hg	3/2	13.18	1.16	38.7	-1.788 769	0.066 115 83

[a] Receptivity versus ^{13}C at natural abundance
[b] Nuclear quadrupole moment
[c] Gyromagnetic ratio
[d] Frequency factor (relative to 1.000 000 00 for ^1H)
[e] Calculated value

1.3 Nickel Compounds and Nickel NMR

Selecting high-symmetry nickel species for NMR characterization is not trivial. Like some other transition metal elements discussed previously, the majority of nickel chemistry occurs with nickel in a paramagnetic oxidation state (usually nickel(II)). Diamagnetic species do exist (i.e. Ni(0) compounds) but tend to be extremely air-sensitive. Therefore, before introducing nickel NMR and the literature therein, it is first worth discussing nickel chemistry, with a focus on nickel(0) and its chemical importance from a synthetic and catalytic perspective.

1.3.1 Nickel Chemistry

From a catalytic point-of-view, nickel has developed a rather underserved reputation as a less effective, cheaper substitute for palladium.[43] The cost difference between nickel and the other Group 10 elements alone commends exploration of it as an alternative catalyst, but it also has many properties which give it unique chemical advantages in certain reactions versus other transition metal elements.[43] Nickel is relatively electropositive, such that oxidative addition occurs readily (since it removes electron density from the metal center), while reductive elimination is more difficult.[43] The preference over palladium toward oxidative addition allows for cross-coupling reactions with electrophiles to occur much more favourably, allowing for the use of phenol derivatives, aromatic nitriles, and aryl fluorides, to name a few.[43] Further, nickel has a tendency to donate *d*-electrons readily to π-acceptors, resulting in unusually strong olefin bonding.[43] β-hydride elimination with nickel is consequentially more difficult than with palladium due to rigidity in the Ni-C bond.[43] Nickel also has a tendency to activate otherwise inert C-N and C-O bonds, and has a smaller atomic radius than palladium, such that nickel-ligand bond lengths are usually relatively short.[43] However, the most important difference chemically between nickel and palladium, in terms of their catalytic performance at least, is the ready access of nickel catalytic cycles to a variety of oxidation states. While both Pd(0)/Pd(II) and Ni(0)/Ni(II) catalytic cycles are prevalent, nickel also has access to the +1 and +3 oxidation states (radical chemistry is therefore also much significant for nickel compared to palladium), which can facilitate much more varied catalytic pathways; these include Ni(I)/Ni(III), Ni(0)/Ni(II)/Ni(I), and even wholly Ni(I) cycles.[43]

Wilke laid much of the groundwork for understanding the structure and reactivity of nickel complexes in the postwar period (and was the first to synthesize bis(1,5-cyclooctadiene)nickel(0) (Ni(cod)$_2$)), and nickel has been used from the 1970s in cross-coupling reactions of alkenes and alkynes.[43,44] However, it is only fairly recently that intensive efforts at taking advantage of the unique chemistry of nickel for homogenous catalytic application have begun in earnest.[43] In particular, nickel has been shown to have important uses in cross-coupling reactions, the Heck reaction, and reductive coupling reactions.[43]

Cross-coupling reactions, where two starting materials are added together with the aid of a transition metal catalyst and (usually) activating groups, are an active area of research, with an ever-expanding library of cross-coupling partners reported in the literature.[43] Nickel has been shown to be particularly effective for Suzuki-Miyaura (organoboron-activated) and Negishi (organozinc-activated) cross-coupling reactions.[43,45] Suzuki-Miyaura reactions producing various biaryls are catalyzed by nickel, including Ni(cod)$_2$ (Figure 6).[43,45] Activation of benzylic C-O bonds by Ni(0) catalysts is promising for its use in pharmaceutical synthesis, given that such reactions can be extremely stereoselective and have the advantage of preserving the chirality information contained in the starting material without the use of directing groups or catalyst control (Figure 7).[43,46,47] As also shown in Figure 7, ligands can be added to reaction mixtures involving Suzuki-Miyaura cross-coupling of benzylic esters, carbonates, and carbamates to control whether the stereoisomerism of the starting material is retained or inverted.[43,47] Further, nickel catalysts have been used for cross-coupling reactions between *sp*^{3} carbon electrophiles, demonstrating the first carbon-carbon *sp*^{3}-*sp*^{3} cross-coupling with a secondary electrophile

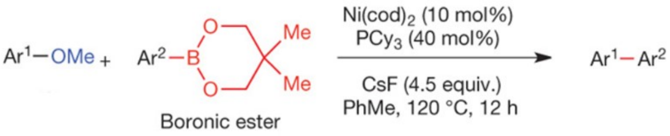

Figure 6: A Suzuki-Miyaura-type biaryl synthesis using Ni(cod)$_2$ as a homogenous catalyst. Adapted by permission from Macmillan Publishers Ltd: Nature (ref. 43), copyright (2014). https://www.nature.com/

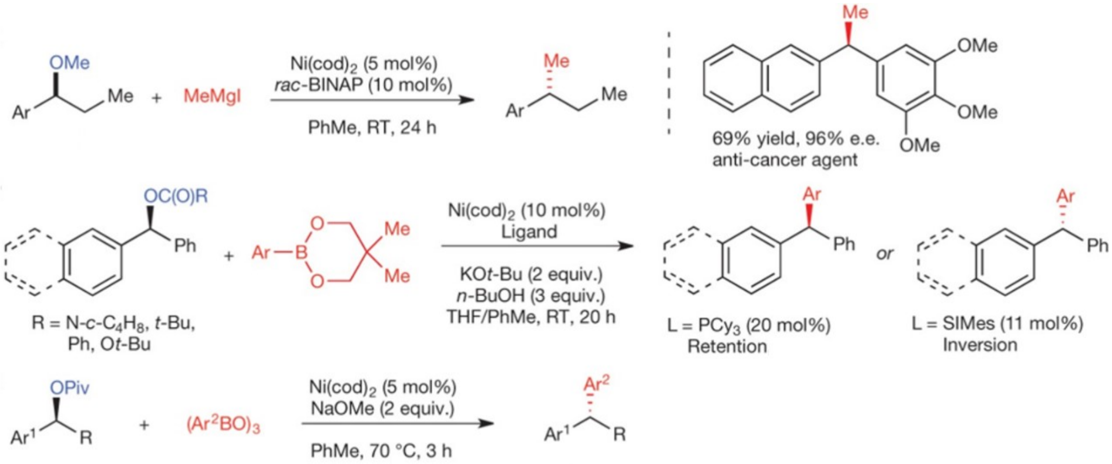

Figure 7: A selection of stereospecific cross-coupling reactions catalyzed by Ni(cod)$_2$. The choice of ligand and the use of a nickel catalyst allows for highly stereospecific reactions, and in some cases (as for the middle reaction) use of different ligands allows for selection of either stereochemistry in the product. Adapted by permission from Macmillan Publishers Ltd: Nature (ref. 43), copyright (2014). https://www.nature.com/

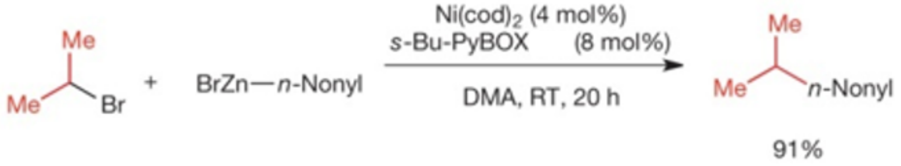

Figure 8: The prototypical reaction for secondary C(sp^3)-C(sp^3) cross-coupling, which made use of organozinc reagents and secondary bromides and iodides in a Negishi reaction. *s*-Bu-PyBOX is a bulky chelating ligand that suppresses *β*-hydride elimination. Adapted by permission from Macmillan Publishers Ltd: Nature (ref. 43), copyright (2014). https://www.nature.com/

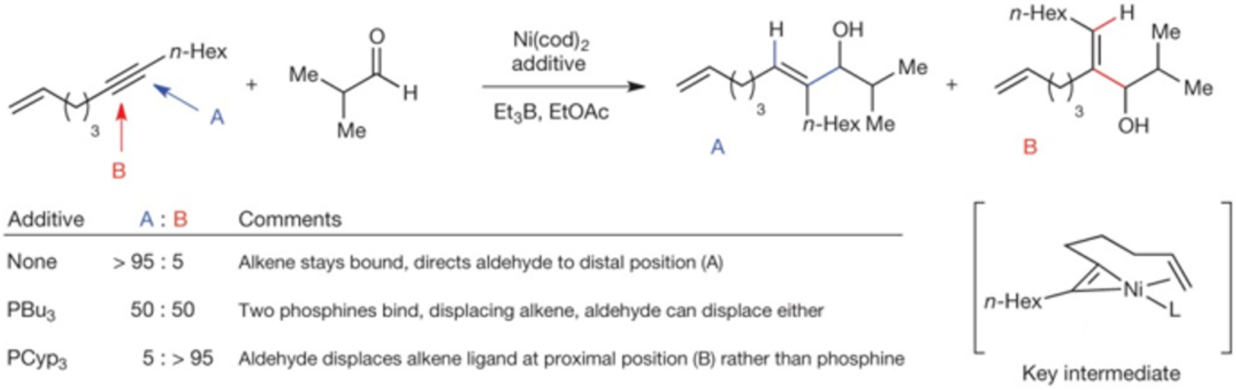

Additive	A : B	Comments
None	> 95 : 5	Alkene stays bound, directs aldehyde to distal position (A)
PBu_3	50 : 50	Two phosphines bind, displacing alkene, aldehyde can displace either
$PCyp_3$	5 : > 95	Aldehyde displaces alkene ligand at proximal position (B) rather than phosphine

Figure 9: The use of additives with nickel-catalysed reductive coupling reactions has been demonstrated to provide regiocontrol, allowing for selective production of either branched or linear products. Adapted by permission from Macmillan Publishers Ltd: Nature (ref. 43), copyright (2014). https://www.nature.com/

(Figure 8), and more recently, through the use of a nickel 'pincer' complex in catalyzing Kumada coupling and Sonogashira reactions.[43,48] Reductive cross-coupling reactions, which obviate the use of nucleophilic reagents by joining two electrophiles without forming organometallic side-products on a stoichiometric scale, have also benefited from the use of nickel. These reactions are complicated by the possibility of homodimerization, which can be suppressed by the use of radical- and polar-addition mechanisms for the two different cross-coupling reagents; the availability of a myriad of nickel oxidation states allows for radical and polar addition/reduction steps to be separated.[43] Finally, direct functionalization through C-H bond activation presents its own sets of benefits and challenges (namely difficulty in control of addition, due to the frequent presence of numerous chemically similar C-H bonds).[43]

The Heck reaction is related to cross-coupling reactions, but with the oxidative addition complex coordinating an alkene rather than undergoing transmetallation.[43,49] Migratory insertion followed by β-hydride elimination results in a more substituted alkene.[43,49] Among other interesting characteristic behaviour of nickel catalysts with respect to the Heck reaction, it has been shown that these catalysts in particular are able to perform highly regioselective Heck reactions (for both branch- and terminal-selective reactions), thanks likely to the short lengths of nickel-ligand bonds.[43]

Lastly, reductive coupling, wherein two π-bonded components are joined through the catalytic formation of a σ-bond, has also taken advantage of nickel catalysis in recent years to fine-tune regiocontrol.[43,50] The key to this reaction is the use of additives to direct the addition, producing either linear or branched molecules (Figure 9).[43,51]

Apart from the specific applications mentioned here, Ni(cod)$_2$ is a ubiquitous source of Ni(0), whether for synthesis of further nickel catalysts or as a catalyst itself.[43,52] The other target compounds of this thesis also have important catalytic uses: tetrakis(triphenylphosphite)nickel(0) ($Ni[P(OPh)_3]_4$) has been shown to catalyze transfer hydrogenation[53] and as an initiator for free-radical polymerization of vinyl monomers[54] (among other applications), while the uses of tetrakis(triphenylphosphine)nickel(0) ($Ni(PPh_3)_4$) include, but are not limited to, catalytic cyanation[55] and oxidation of phosphines to phosphine oxides.[56]

Nickel(0) catalytic precursors, despite their importance, are not trivial in terms of their characterization, given that most are very air-sensitive and decompose rapidly in atmosphere. However, their diamagnetic electronic configuration, and for the most part high-symmetry tetrahedral structures, would recommend them for study by NMR spectroscopy, which is by its nature non-invasive.

Nickel homogeneous catalysis, despite only scratching the surface of the element's applications, demonstrates the diversity and utility of nickel chemistry. Furthermore, unlike for the more catalytically-celebrated palladium, nickel NMR spectroscopy has a clear and present role to play in characterizing nickel structures, both in solution and the solid state.

1.3.2 Nickel-61 NMR

Given the chemical significance of nickel(0) in particular, it is perhaps unsurprising that several solution ^{61}Ni NMR reports exist in the literature, (though solid-state characterization has thus far been limited to Knight shift studies of intermetallics and nickel metal, and will be discussed later). Early work by L.E. Drain[57] (1964) was followed by Schumann et al.[58] (1980), who characterized ^{61}Ni chemical shifts and measured $^{1}J(^{61}\text{Ni}-^{31}\text{P})$ values for six monosubstituted nickel tetracarbonyl derivatives. Hao et al. provided a thorough characterization of nickel complexes by solution ^{61}Ni NMR in 1982,[59] using $Ni(CO)_4$ as the primary reference, as suggested by previous work. A number of parameters were provided, including isotropic shifts, linewidths, and *J* coupling values (in general, $^{1}J(^{61}Ni-^{31}P)$ values are 200 to 500 Hz).[59] Of particular interest is the spectrum of $Ni(PF_3)_4$ provided, where two-bond fluorine-nickel coupling could be observed and measured (with $^{2}J(^{61}Ni-^{19}F)$ = 17 Hz).[59] The trends in reduced coupling constants agreed with the established observation that reduced coupling constants increase across and down the periodic table due to contraction of *s*-electron density toward the metal center (the reduced coupling constant is related to the *J* coupling constant, but includes corrections for the gyromagnetic ratios of the nuclei involved).[59] Benn and Rufińska added some solution $\delta_{iso}(^{61}Ni)$ values to the literature in their 1986 review of metal NMR spectroscopy of organometallics, and noted that the ^{61}Ni chemical shift in tetrahedrally co-ordinated nickel complexes appeared to be dominated by the frontier orbitals.[20] Characterization of the synthetic product $Ni(PMe_3)_4$ by Avent et al. in 1988 included characterization by solution ^{61}Ni NMR spectroscopy.[60] In their publication from the same year regarding two-dimensional heteronuclear NMR spectroscopy of low-γ metal nuclei, Benn and Rufińska included two dimensional ^{61}Ni-^{31}P correlation spectra, and, combined with one-dimensional spectra, documented chemical shifts and *J* coupling values of more monosubstituted tetracarbonylnickel derivatives (though their referencing scheme is versus $Ni(PMe_3)_4$, they do include a measured chemical shift of $Ni(CO)_4$).[61] The authors noted that unlike the spin-1/2 nuclides studied by their method (^{183}W, ^{57}Fe, and ^{103}Rh), sensitivity enhancement was limited by the rapid relaxation of quadrupolar ^{61}Ni nuclei relative to the ^{31}P polarization source (i.e. limiting the amount of polarization which could be effectively transferred from the slower-relaxing ^{31}P nuclei in any given experiment before the ^{61}Ni nuclei relaxed to their Boltzmann distribution).[61] A 1995 study by Behringer and Blümel demonstrated the benefits of using solenoid probeheads to measure solution ^{61}Ni NMR spectra, documenting temperature and solvent dependencies for monosubstituted nickel tetracarbonyl complexes.[62] The authors also made successful attempts to characterize the chemical shifts of less symmetric disubstituted nickel tetracarbonyl derivatives, but were only able to successfully measure the $^{1}J(^{61}\mathrm{Ni}\text{-}^{31}\mathrm{P})$ value for $Ni[(CO_4)]_2[PMe_3]_2$, which was 250 Hz, as the other ^{61}Ni spectra were prohibitively broadened.[62] Beyond this, Behringer and Blümel found that measurement of nickel-phosphorus couplings from satellites in ^{31}P spectra was in general impractical (due to relaxation induced broadening), and concluded that steric effects (i.e. ligand cone angles) had no correlation with either chemical shifts or *J* coupling values, both apparently being dominated by electronic effects.[62] They also attempted to acquire a ^{61}Ni SSNMR spectrum of $Ni(cod)_2$ using a 7 mm rotor at a 4 kHz spinning speed,[62] but given the spectra presented in this thesis it is unsurprising that they did not obtain results. In their following (1996) solid-state ^{31}P and ^{13}C NMR study of immobilized catalysts, Behringer and Blümel used a similar approach to measure the solution ^{61}Ni chemical shift and *J* coupling values (where possible) of further di- and tricarbonylnickel complexes.[63] More recently, Bühl et al. carried out a thorough computational study at the gauge-including atomic orbitals density functional theory (GIAO DFT) level of ^{61}Ni NMR spectroscopy parameters for gas-phase structures, including some limited experimental results.[64] Their computational results will be discussed in more detail in Section 2.2.3, but most notably they were able to assess the effects of functional hybridization on calculation of ^{61}Ni chemical shifts, proposed the adoption of an indirect magnetic shielding referencing scheme for nickel-61 computation, and were able to provide some limited insights into the quadrupolar environment of the nickel site in some of the compounds studied.[64] It should be noted that despite their lower symmetry (which induces more rapid relaxation and signal broadening) the δ_{iso} values in solution for two trigonal planar species ($Ni(C_2H_4)_2(PMe_3)$ and (all-*trans*-1,5,9-cyclododecatriene)nickel(0)) have been reported.[20,64]

The first solid-state NMR characterization of ^{61}Ni outside Knight shift studies of the metal itself[65,66] appears to be a Knight shift study of a Ce_7Ni_3 antiferromagnet at ultralow temperatures at ambient pressure, published in 2000 by Mishina et al.[67] The resulting spectra were extremely low resolution and are not directly comparable to the quality of NMR spectra necessary for characterization of anything but extremely basic line shape features.[67] A 2003 study by Bastow et al. of Ni-Y intermetallics produced Knight shift spectra which could be used to access a significant amount of chemically relevant information.[68] ^{61}Ni NMR spectroscopy performed with $Ni_{1-x}Al_x$ (with $0.492 \leq x \leq 0.520$) as a function of aluminum stoichiometry showed the presence of two sites, with a lower-symmetry site producing a broadened baseline feature and a higher-symmetry site producing a sharp peak.[68] Nickel-61 SSNMR spectra were also recorded as a function of temperature, highlighting phase transitions in NiTi.[68] Full solid-state ^{61}Ni NMR spectra were reported for Ni_2Al_3; Ni_2Ga_3; Ni_2In_3; $NiAl_3$; $Ni_{1-x}Ga_x$ with $x = 0.52$, 0.51, 0.50, 0.49 and 0.48; Ni_3Al_4; NiIn; and NiTi, with quadrupolar coupling constants (C_Q) and quadrupolar asymmetry parameters (η) measured from spectral fitting for the latter three species ($C_Q = 5.0$ MHz and $\eta = 0.68$ for Ni_3Al_4; $C_Q = 6.0$ MHz and $\eta = 0.67$ for NiIn; $C_Q = 5.7$ MHz and $\eta = 0.30$ for NiTi).[68] The Knight shifts displayed for these compounds are well outside the -1000 to +1000 ppm range established for solution (diamagnetic) ^{61}Ni NMR, with K_{iso} values ranging from 7510 ppm for NiTi to 140 ppm for Ni_3Al_4.[68] Beyond these Knight shift studies, however, it is expected that this thesis presents the first characterization of diamagnetic compounds in the solid state by ^{61}Ni NMR spectroscopy.

1.4 Objectives

The goal of this thesis, then, is primarily to demonstrate how nuclear magnetic resonance spectroscopy can be applied to studies of insensitive nuclides, especially in the solid state, by providing novel results in the application of ^{61}Ni NMR spectroscopy. Specifically, it will be shown that there exists a relationship between observed NMR parameters and the chemical environment of the nickel site, which can be characterized directly by taking advantage of ^{61}Ni NMR. To the knowledge of the author, this work presents the first characterization of diamagnetic compounds in the solid state by nickel-61 NMR spectroscopy, as well as the first reported ^{61}Ni chemical shift tensors. Computational work and solution NMR are also described as a complement to the solid-state NMR results obtained. The theory of the techniques used, the means of their application, and the obstacles involved will be thoroughly accounted, before introducing the results of the Master's work and their significance in the context of literature.

2 EXPERIMENTAL METHODOLOGY

2.1 NMR Spectroscopy

Having discussed the physical origins of nuclear magnetic resonance phenomena in the preceding section, the fundamental physical and chemical aspects of NMR spectroscopy will be extended into the realm of practical experimentation, both in terms of the basic principles of simple magnetic resonance experiments and carrying on to the special considerations required when performing SSNMR. Distinct attention will be paid to the Carr-Purcell-Meiboom-Gill (CPMG, and its analogous quadrupolar QCPMG) experiment.

2.1.1 General Considerations of the NMR Experiment

NMR spectroscopy can be tremendously complicated, especially when one considers experiments that involve polarization transfer between multiple nuclides, sample rotation, variable temperature effects, quadrupolar nuclei, and more. However, the basic framework of the NMR experiment can be described equally well by both vector and quantum mechanical models. As such, the principles of NMR spectroscopy, together with considerations of the equipment involved and concepts mundane to NMR in both solution and the solid-state (including of quadrupolar nuclides), will be discussed now with reference to the vector model.

2.1.1.1 The Basic NMR Experiment

Before discussing manipulation of spins, it is first necessary to explicitly define the behaviour of an ensemble of spins at rest in an external magnetic field – essentially, providing a physical and mathematical description of the net magnetization resulting from the Zeeman effect-derived Boltzmann distribution of spins. After inserting a sample into an NMR spectrometer, the net magnetization will evolve according to:

$$M(t) = M_z(t) = M(\mathrm{eq})\left(1 - \exp\left\{-\frac{t - t_a}{T_1}\right\}\right)$$

[2-1]

where M_z is the magnetization vector along the external magnetic field, $M(\mathrm{eq})$ is the equilibrium magnetization vector, t_a is the time at which the sample is (instantaneously) transferred into the magnetic field, and T_1 is the longitudinal relaxation time constant (see Figure 10).[9,69] This can be visualized using a magnetization vector growing along the axis of the applied magnetic field (which will be defined as *z*). A complementary equation exists for when the external magnetic field is abruptly removed, but given that the only time this occurs is when the sample is removed from the spectrometer (and given that both equations depend on the same time constant), it will not be discussed here.[9,69]

Focusing on a single spin in the ensemble, one can describe it as rotating about the *z* axis by combining [1-2] and [1-3], with the frequency of this precession determined by the magnitude of the external field and the gyromagnetic ratio of the nucleus:

$$\omega_0 = -\gamma B_0$$

[2-2]

This rotation occurs because the spin possesses angular momentum in addition to its magnetic moment. Precession becomes extremely important for NMR spectroscopy because it governs the behaviour of magnetization in the transverse plane; magnetization along the external magnetic field is an exceedingly small perturbation on that field, and therefore, out of necessity, detection of nuclear magnetization is performed in the transverse plane. The equations for magnetization in the transverse plane as a function of time are:

$$M_y(t) = -M(\mathrm{eq})\cos(\omega_0 t)\exp\left\{-\frac{t}{T_2}\right\} \tag{2-3}$$

$$M_x(t) = -M(\mathrm{eq})\sin(\omega_0 t)\exp\left\{-\frac{t}{T_2}\right\} \tag{2-4}$$

where T_2 is the transverse relaxation time constant.[9,69] From these equations it becomes clear that the transverse net magnetization vector rotates and decays to zero with time, whereas the longitudinal relaxation vector decays from its starting value to its equilibrium value with time. As a practical matter, transferring magnetization from the *z* axis to the *xy* plane would seem irrelevant, given that the obvious means of doing so would require a magnetic field of similar strength to the field along *z*. However, because of the physical phenomenon of resonance, a much weaker field oscillating at the Larmor frequency ω_0 can be used to bring the net magnetization vector into alignment. Piecing the relaxation components together with an applied resonating field B_1 gives the simplest magnetic resonance experiment (Figure 11a). Note that the shorthand for this sequence of relaxation, applied magnetic field pulses, and detection (as shown in Figure 11b) is called a pulse sequence. Pulse sequences are the 'roadmaps' of NMR experiments and can become immensely complex. Note that the phase of the applied pulse (i.e. the axis along which it is applied) governs how magnetization is transferred into the *xy* plane (being governed by the 'right-hand rule').

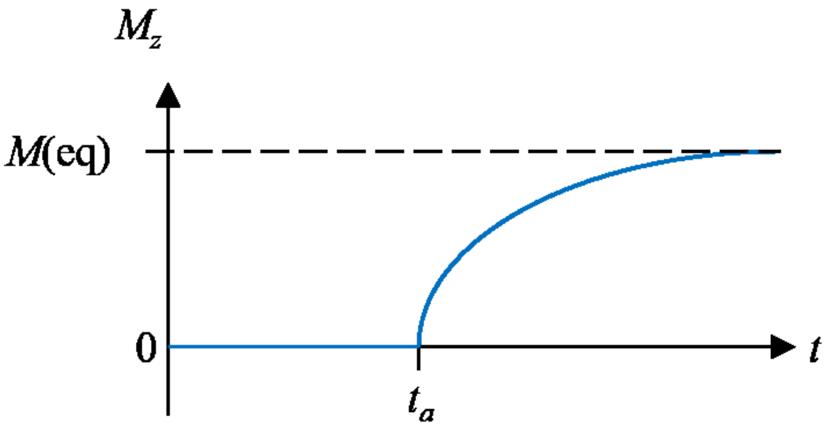

Figure 10: The net magnetization increases asymptotically to its equilibrium value when a sample is inserted into an NMR spectrometer magnetic field (instantaneously) at time t_a, according to [2-1]. Longitudinal 'relaxation' thus involves an increase in magnetization along the z axis (as opposed to transverse relaxation along the x and y axes, described by [2-3] and [2-4]).

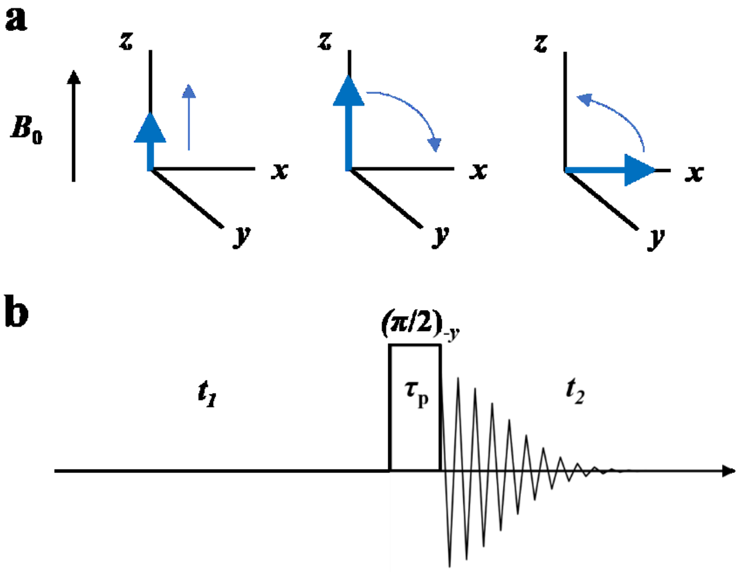

Figure 11: A simple one-pulse NMR experiment as described in vector notation. a) The magnetization along the longitudinal axis decays to its equilibrium value according to [2-1]. Application of a resonating B_1 field causes the magnetization to transfer into the transverse plane. After the B_1 field is turned off, the magnetization decays in the transverse plane according to [2-3] and [2-4], while also decaying longitudinally. As mentioned in Section 2.1.1.5, the transverse relaxation decays at a rate equal to or faster than the longitudinal relaxation. b) A very simple pulse sequence describing the process in a). During the time t_1 the spins are allowed to relax to their equilibrium magnetization. A pulse of length τ_p is then applied, and signal is acquired during time interval t_2 as the spins oscillate in and relax in the transverse plane. This entire process can be repeated to increase signal-to-noise according to [2-11].

Table 3: Equivalent designations for NMR pulse phases.

Phase	Vector notation	Bruker pulse program
$\varphi = 0$	x pulse	0
$\varphi = \pi/2$	y pulse	1
$\varphi = \pi$	$-x$ pulse	2
$\varphi = 3\pi/2$	$-y$ pulse	3

From a mechanical/electronic perspective, the basic $\pi/2$ (90°) pulse experiment can be described (in a simplified manner) as follows: The sample is inserted into a probe contained in a superconducting cryomagnet, where the spins in the sample 'relax' to their Zeeman Boltzmann distribution. Next, the oscillating B_1 field is produced. A transmitter, consisting of an r.f. (radio-frequency) synthesizer, which produces an r.f. wave fluctuating at the spectrometer reference frequency ω_{ref}, a phase shifter and pulse gate, both controlled by a pulse programmer, as well as an r.f. amplifier, combine to produce the particular r.f. pulse demanded for the experiment.[9] The synthesizer-produced r.f. pulse can be described as a cosine wave:

$$s_{\text{synth}} \sim \cos(\omega_{\text{ref}} t + \varphi(t)) \tag{2-5}$$

with the phase of the signal given by $\varphi(t)$.[9,69] The phase shifter controls the phase of the pulse by discontinuously truncating the wave associated with the pulse.[9] The $\pi/2$ phase increments (which are most often used in NMR), and their designations both in NMR literature and the Bruker pulse programming library, are provided in Table 3. The pulse gate opens for a set amount of time to allow the pulse to continue to the spectrometer.[9] This time length is called the pulse length (τ_{p}). The pulse power can alternatively be described in terms of its 'frequency' (in Hz):[9]

$$\nu_{\mu} = \frac{\mu}{2\pi \times \tau_{\text{p}}(\mu)} \tag{2-6}$$

where μ is the effective flip angle of the pulse, and $\tau_p(\mu)$ is the pulse duration required for said flip angle. The amplifier steps up the power of the r.f. pulse, which is modulated by an attenuator to a strength specified for the experiment.[69]

Next the signal from the amplifier arrives at the duplexer, where the incoming r.f. pulse is routed to the probe.[9] The r.f. circuits and coils in the probe generate the B_1 field. The resulting magnetization in the sample spins induces an oscillating field in the probe coil, while is carried toward the duplexer, which now routes the signal to the preamplifier.[9] The signal preamplifier scales up the extremely weak NMR signal so that it can be processed.[9] This amplified signal passes into a quadrature receiver, which compares the output to the spectrometer reference frequency and encodes the resulting signal as a complex function (to preserve information on the sign of the signal frequency relative to ω_{ref}):

$$s_A(t) \sim \cos(\Omega_0 t)\exp\{-\lambda t\} \tag{2-7}$$

$$s_B(t) \sim \sin(\Omega_0 t)\exp\{-\lambda t\} \tag{2-8}$$

$$s(t) = s_A(t) + \mathrm{i}s_B(t) \sim \exp\{(\mathrm{i}\Omega_0 - \lambda)t\} \tag{2-9}$$

$$\Omega_0 = \omega_0 - \omega_{\mathrm{ref}} \tag{2-10}$$

where λ is equivalent to T_2^{-1} and Ω_0 is the relative Larmor frequency.[9,69] Finally, the output signals (real and imaginary separately) are processed by analogue-to-digital converters. Either post-digitization or in the receiver, the NMR signal may have a phase imparted to it (called the receiver phase), in order to suppress artifacts or for selecting coherence pathways (which will be discussed later).[9]

The pulse length is an important value, particularly for acquiring wide spectra, as it directly affects the effective excitation profile of the pulse. Specialized sequences exist to maximize the effective bandwidth excited in an experiment, but for the spectra collected in this thesis the pulse lengths were sufficiently short to excite the full spectrum uniformly (although variable offsets were used to ensure that this was the case).

Some other general matters surrounding NMR spectroscopy will now be briefly introduced. Firstly, signal averaging is of tremendous importance to NMR spectroscopy, given the low inherent sensitivity of the technique. It can be shown that the signal-to-noise ratio increases as the square-root of the number of transients:[9]

$$\frac{s_{\mathrm{NMR}}(1+2+\cdots n)}{s_{\mathrm{noise}}(1+2+\cdots n)} = \sqrt{n}\frac{s_{\mathrm{NMR}}(1)}{s_{\mathrm{noise}}(1)}$$

[2-11]

Secondly, it is important to note that the NMR experiment assumes that the field is homogenous throughout a sample volume, but this is not necessarily the case. Differences in magnetic susceptibility, or inhomogeneity in the external/applied fields themselves, can induce inhomogeneous broadening, as the Larmor frequency of the spins in the sample is dependent on the field in the sample:

$$\omega_0(\mathbf{r}) = -\gamma B_0(\mathbf{r})$$

[2-12]

where $\mathbf{r}$ is a three-dimensional position vector. This causes spins that are otherwise experiencing the same interactions to resonate at different frequencies in the spectrum, spreading out the signal intensity. Lastly, modern NMR spectroscopy depends crucially on the Fourier transform (FT) to convert time-domain acquisition data to frequency-domain spectra. The definition of the FT is:[9]

$$S(\Omega) = \int_0^\infty s(t) \exp\{-\mathrm{i}\Omega t\}\, dt$$

[2-13]

The frequency domain result is a scaled complex Lorentzian function:

$$\mathcal{L}(\Omega; \Omega_l, \lambda) = \frac{1}{\lambda + \mathrm{i}(\Omega - \Omega_l)}$$

[2-14]

where Ω_l and λ, respectively, are the frequency and linewidth parameter (T_2^{-1}) of the component l of the total NMR signal (i.e. for each of the peaks l in the overall spectrum).[9] The complex Lorentzian can be decomposed into absorption and dispersion components:[9]

$$\mathcal{A}(\Omega; \Omega_l, \lambda) = \mathrm{Real}\{\mathcal{L}(\Omega; \Omega_l, \lambda)\} = \frac{\lambda}{\lambda^2 + (\Omega - \Omega_l)^2}$$

[2-15]

$$\mathcal{D}(\Omega; \Omega_l, \lambda) = \mathrm{Imaginary}\{\mathcal{L}(\Omega; \Omega_l, \lambda)\} = \frac{\Omega - \Omega_l}{\lambda^2 + (\Omega - \Omega_l)^2}$$

[2-16]

These functions are depicted visually as Figure 12. The absorption mode Lorentzian is much easier to work with given its rapid decay away from the center of the line, and for the 1D NMR experiments encountered in this work it is possible to convert between the two modes post-processing using a set of zero- and first-order phase correction terms. It is important to note that both Lorentzian components depend on the transverse relaxation rate, and thus the NMR linewidth depends directly on the rate of relaxation of the nuclei measured (with faster relaxing spins producing broader lines).

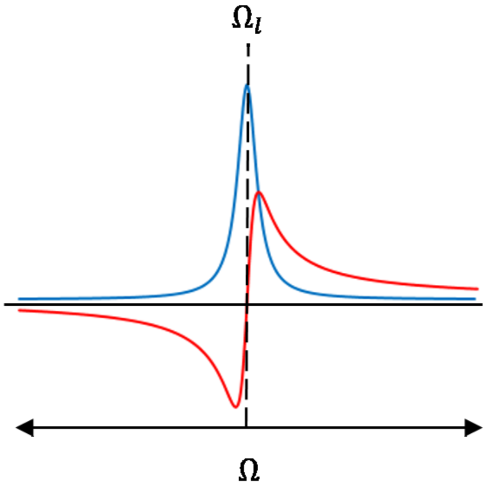

Figure 12: A plot of the real (absorption, blue) and imaginary (dispersion, red) components of the Lorentzian function
[2-15], [2-16]). λ affects the width of the function, while Ω_l defines its center.

2.1.1.2 The Quantum Mechanical Model of NMR

While the vector model of NMR has its uses, understanding the evolution of nuclear spins under more complex pulse sequences requires a quantum mechanical treatment of magnetic resonance. Analysis through the quantum mechanical lens will begin with isolated spin-1/2 nuclei, moving on to ensembles of nuclei, before introducing some of the specific quantum mechanics and practical phenomena associated with NMR of quadrupolar nuclei. The NMR interaction Hamiltonians, which were examined in Chapter 1, will be taken at their face value, as the primary concern is being able to describe nuclear spins and the effects of applying r.f. pulses to those spins. In this section, the basic single-pulse experiment will be expressed for a single spin through quantum mechanics.

A single spin-1/2 has two angular momentum eigenstates along the *z* axis parallel to the external field B_0:

$$|\alpha\rangle = \left|\frac{1}{2}, +\frac{1}{2}\right\rangle \tag{2-17}$$

$$|\beta\rangle = \left|\frac{1}{2}, -\frac{1}{2}\right\rangle \tag{2-18}$$

with $|\alpha\rangle$ being referred to as 'spin-up' and $|\beta\rangle$ as 'spin-down'.[9,69] These states are Zeeman eigenstates if they satisfy the following eigenequations:

$$\hat{I}_z|\alpha\rangle = +\frac{1}{2}|\alpha\rangle \tag{2-19}$$

$$\hat{I}_z|\beta\rangle = -\frac{1}{2}|\beta\rangle \tag{2-20}$$

where $\hat{I}_z$ is the z angular momentum operator (Appendix I).[9,69] The spin can exist in a superposition of states, though the coefficients must be normalized:

$$|\psi\rangle = c_\alpha|\alpha\rangle + c_\beta|\beta\rangle$$

$$|c_\alpha|^2 + |c_\beta|^2 = 1 \tag{2-21}$$

where c_α and c_β are called superposition coefficients.[9,69] A summary of the important superposition states is provided in Appendix I. When the sample is equilibrated with the external magnetic field, there is no r.f. field applied and the motion can be described by solving the time-dependent Schrodinger equation using the Zeeman Hamiltonian:

$$\frac{\mathrm{d}}{\mathrm{d}t}|\psi\rangle(t) = -\mathrm{i}\hat{H}_0|\psi\rangle(t) = -\mathrm{i}\omega_0\hat{I}_z|\psi\rangle(t) \tag{2-22}$$

$$|\psi\rangle(t_b) = \exp\{-\mathrm{i}\omega_0\tau\hat{I}_z\}|\psi\rangle(t_a) \tag{2-23}$$

where t_a and t_b are initial and final timepoints and τ is the time between them.[9] The first term in [2-23] has the form of a rotation operator, which is the quantum mechanical operator which describes motion about an axis (in this case the z-axis):[9,16]

$$\hat{R}_z(\varphi) = \exp\{-i\varphi\hat{I}_z\} = \begin{bmatrix} \exp\left\{-i\left(\frac{\varphi}{2}\right)\right\} & 0 \\ 0 & \exp\left\{+i\left(\frac{\varphi}{2}\right)\right\} \end{bmatrix}$$
$$= \begin{bmatrix} \cos\left(\frac{\varphi}{2}\right) - \mathrm{i}\sin\left(\frac{\varphi}{2}\right) & 0 \\ 0 & \cos\left(\frac{\varphi}{2}\right) + \mathrm{i}\sin\left(\frac{\varphi}{2}\right) \end{bmatrix} \tag{2-24}$$

The solution to the Schrödinger equation for an unperturbed spin in an external magnetic field is then:

$$|\psi\rangle(t_b) = \hat{R}_z(\omega_0 \tau)|\psi\rangle(t_a)$$

[2-25]

The angular frequency and time interval term in the rotation operator are equivalent to an angle of arc swept out by the spin during that time interval:

$$\tau = \left|\frac{\pi}{2\omega_0}\right|$$

[2-26]

A spin completely in either the α or β state can be shown to not evolve over time:

$$|\psi\rangle(t_b) = \hat{R}_z(\omega_0 \tau)|\alpha\rangle(t_a) = \frac{1}{\sqrt{2}}\begin{bmatrix} \exp\left\{-i\left(\frac{\omega_0 \tau}{2}\right)\right\} & 0 \\ 0 & \exp\left\{+i\left(\frac{\omega_0 \tau}{2}\right)\right\} \end{bmatrix}\begin{bmatrix} 1 \\ 0 \end{bmatrix}$$

$$= \frac{1}{\sqrt{2}}\exp\left\{-i\left(\frac{\omega_0 \tau}{2}\right)\right\}\begin{bmatrix} 1 \\ 0 \end{bmatrix} = k|\alpha\rangle$$

[2-27]

where k is simply a constant called a phase factor (and similarly for the β eigenstate). Likewise, it is possible to show that a spin in a superposition state will evolve as would be expected from the vector model (i.e. around a circle in the *xy* plane).[9,69]

Before analyzing the effects of B_1 fields on the magnetization, it is preferable to move to a rotating reference frame, which rotates with constant frequency ω_{ref} about the *z* axis. The axes of the rotating frame are related to the laboratory frame axes by a time-dependent angle $\Phi(t)$ (for brevity, the dependence of Φ on *t* will be assumed in subsequent notation):

$$\mathbf{e}^{\text{rrf}}{}_x = \mathbf{e}_x \cos\Phi(\text{t}) + \mathbf{e}_y \sin\Phi(\text{t})$$

[2-28]

$$\mathbf{e}^{\text{rrf}}{}_y = \mathbf{e}_y \cos\Phi(\text{t}) - \mathbf{e}_x \sin\Phi(\text{t})$$

[2-29]

$$\mathbf{e}^{\text{rrf}}{}_z = \mathbf{e}_z$$

[2-30]

where the superscript 'rrf' is indicative of the rotating reference frame.[9,69] Thus, any conversion between the laboratory and rotating frames can be accomplished by rotation about the z axis:

$$|\psi^{\mathrm{rrf}}\rangle = \hat{R}_z(-\Phi)|\psi\rangle$$

[2-31]

The time-dependent Schrodinger equation now depends on the rotating-frame Hamiltonian:[9]

$$\frac{\mathrm{d}}{\mathrm{d}t}|\psi^{\mathrm{rrf}}\rangle(t) = -\mathrm{i}\hat{H}_0^{\mathrm{rrf}}|\psi\rangle(t) = \hat{R}_z(-\Phi)\hat{H}_0^{\mathrm{rrf}}\hat{R}_z(\Phi) - \omega_{\mathrm{ref}}\hat{I}_z$$

[2-32]

With the application of an r.f. pulse, the Hamiltonian for the spin can be written as:

$$\hat{H}(t) = \hat{H}_0 + \hat{H}_{\mathrm{r.f.}}(t) \cong \omega_0\hat{I}_z + \left[-\tfrac{1}{2}\gamma B_1 \sin\theta_1 \{\cos(\omega_{\mathrm{ref}}t + \varphi_{\mathrm{p}})\hat{I}_x + \sin(\omega_{\mathrm{ref}}t + \varphi_{\mathrm{p}})\hat{I}_y\}\right]$$

[2-33]

where φ_{p} is the phase of the applied pulse and $\sin\theta_1$ is associated with the oscillation of the B_1 field.[9] This equation can be simplified to the following form in the rotating reference frame (the mathematics involved are time-consuming if not especially complex, and thus will be omitted):[9]

$$\hat{H}^{\mathrm{rrf}}(t) \cong \Omega_0\hat{I}_z + \omega_{\mathrm{nut}}(\hat{I}_x \cos\varphi_{\mathrm{p}} + \hat{I}_y \sin\varphi_{\mathrm{p}})$$

[2-34]

where the nutation frequency is defined as:

$$\omega_{\mathrm{nut}} = \left|\frac{1}{2}\gamma B_1 \sin\theta_1\right|$$

[2-35]

One can now see the value of the rotating frame, in that it results in a time-independent equation for the spin Hamiltonian under an applied r.f. pulse.

For an on-resonance x pulse (i.e. one with phase $\varphi_{\mathrm{p}} = 0$), the rotating frame Hamiltonian becomes:

$$\hat{H}^{\mathrm{rrf}}(t) \cong \omega_{\mathrm{nut}}\hat{I}_x$$

[2-36]

Integrating [2-32], the time-dependent Schrödinger equation in the rotating reference frame, yields:[9]

$$|\psi^{\text{rrf}}\rangle(t_b) = \exp\{-i\omega_{nut}\tau_p\hat{I}_x\}\,|\psi^{\text{rrf}}\rangle(t_a)$$

[2-37]

One can substitute the definition of the flip angle, introduced previously, into the equation to simplify:

$$|\psi^{\text{rrf}}\rangle(t_b) = \exp\{-i\mu\hat{I}_x\}\,|\psi^{\text{rrf}}\rangle(t_a)$$

[2-38]

This is now in the form of the rotation operator about *x* through the flip angle:[9]

$$|\psi^{\text{rrf}}\rangle(t_b) = \hat{R}_x(\mu)|\psi^{\text{rrf}}\rangle(t_a)$$

[2-39]

which, in its matrix representation, is:[9]

$$\hat{R}_x(\mu) = \exp\{-i\mu\hat{I}_x\} = \begin{bmatrix} \cos\left(\frac{\mu}{2}\right) & -\mathrm{i}\sin\left(\frac{\mu}{2}\right) \\ -\mathrm{i}\sin\left(\frac{\mu}{2}\right) & \cos\left(\frac{\mu}{2}\right) \end{bmatrix}$$

[2-40]

The equation can now be solved for a variety of starting states, and produces final states multiplied by phase factors, which are generally unimportant[9]. For the sake of completeness, the rotation operator about the *y* axis is:[9]

$$\hat{R}_y(\mu) = \exp\{-i\mu\hat{I}_y\} = \begin{bmatrix} \cos\left(\frac{\mu}{2}\right) & -\sin\left(\frac{\mu}{2}\right) \\ \sin\left(\frac{\mu}{2}\right) & \cos\left(\frac{\mu}{2}\right) \end{bmatrix}$$

[2-41]

This set of quantum mechanical equations constitutes a template from which the final state of a spin after a strong, on-resonance *x* or *y* pulse (or a series thereof) can be determined from its initial state. In the following sections, it will be presumed that equations are for the rotating reference frame unless otherwise noted.

2.1.1.3 Populations and Coherences

Since NMR experiments are performed on ensembles of spins, it is necessary to introduce the concept of the density operator, as well as populations and coherences. A full treatment will not be given, but the origins of these terms as well as the evolution of populations and coherences under some prototypical conditions will be summarized.

The density operator method is based on the expectation value of an observable and describes all spins in a system simultaneously.[9,69] The wavefunction as an arbitrary superposition of states [2-21] can be used to find the expectation value of an operator:[9,69]

$$\begin{aligned}\langle \hat{F} \rangle &= \langle \psi | \hat{F} | \psi \rangle \\ &= \begin{pmatrix} c_\alpha^* & c_\beta^* \end{pmatrix} \begin{pmatrix} F_{\alpha\alpha} & F_{\alpha\beta} \\ F_{\beta\alpha} & F_{\beta\beta} \end{pmatrix} \begin{pmatrix} c_\alpha \\ c_\beta \end{pmatrix} \\ &= c_\alpha c_\alpha^* F_{\alpha\alpha} + c_\alpha c_\beta^* F_{\alpha\beta} + c_\beta c_\alpha^* F_{\beta\alpha} + c_\beta c_\beta^* F_{\beta\beta}\end{aligned}$$

[2-42]

The quadratic products can be separated out into a single term:

$$|\psi\rangle\langle\psi| = \begin{pmatrix} c_\alpha c_\alpha^* & c_\alpha c_\beta^* \\ c_\beta c_\alpha^* & c_\beta c_\beta^* \end{pmatrix}$$

[2-43]

The expectation value of the operator can then be expressed as the trace of the product of the operator and the term from [2-43]:[9]

$$\langle \hat{F} \rangle = \mathrm{Tr}\{ |\psi\rangle\langle\psi| \hat{F} \}$$

[2-44]

For two spins, the most likely value for the observable is:[9]

$$\langle \hat{F}_{\mathrm{obs}} \rangle = \mathrm{Tr}\{ (|\psi_1\rangle\langle\psi_1| + |\psi_2\rangle\langle\psi_2|) \hat{F} \}$$

[2-45]

Extending this to an infinite number of spins, it is possible to define an operator, called the spin density operator:[9]

$$\hat{\rho} = \overline{|\psi\rangle\langle\psi|}$$

[2-46]

The average contribution of each spin to the macroscopic observable is then given as:

$$\langle\hat{F}\rangle = \mathrm{Tr}\{\hat{\rho}\hat{F}\}$$

[2-47]

The spin density operator greatly simplifies calculation of the behaviour of multi-spin systems as it represents the state of the entire spin set. In its matrix representation, diagonal elements are called populations of $|\alpha\rangle$ and $|\beta\rangle$, while off-diagonal elements are termed coherences between those states (and are called the (+1)- and (-1)-quantum coherences):[9]

$$\hat{\rho} = \overline{|\psi\rangle\langle\psi|} = \begin{pmatrix} \rho_{\alpha\alpha} & \rho_{\alpha\beta} \\ \rho_{\beta\alpha} & \rho_{\beta\beta} \end{pmatrix} = \begin{pmatrix} \overline{c_\alpha c_\alpha^*} & \overline{c_\alpha c_\beta^*} \\ \overline{c_\beta c_\alpha^*} & \overline{c_\beta c_\beta^*} \end{pmatrix} = \begin{pmatrix} \rho_{\boxed{\alpha}} & \rho_{\boxed{+}} \\ \rho_{\boxed{-}} & \rho_{\boxed{\beta}} \end{pmatrix}$$

[2-48]

The order of a coherence is the difference in *z* angular momentum between the two connected states.[9] Thus, the (-1)-quantum coherence is from $|\alpha\rangle$ to $|\beta\rangle$, while the (+1)-quantum coherence is from $|\beta\rangle$ to $|\alpha\rangle$. Because the quantum coherences are complex conjugates of each other, it is impossible to have only a (+1)- or only a (-1)-quantum coherence in a system; likewise, the sum of the populations (which are both real and positive) must be unity, which ties the two values together.[9]

From a physical perspective, the populations represent the fractional contributions of the $|\alpha\rangle$ and $|\beta\rangle$ states to the overall magnetization of the sample (although not the actual fraction of spins in those states, as the spins are free to exist in superposition states between the spin-up and spin-down states).[9,69] The (-1)-quantum coherence indicates the magnitude of net transverse polarization in the *xy* plane, with the phase of this complex number indicating the direction of the net polarization vector in the transverse plane.[9,69] Coherence orders and pathways will be important for the pulse sequences described later in this chapter, and correspond directly to the discussion presented here (although the next section will expand on coherences and populations for quadrupolar spins first).

The thermal-equilibrium spin density operator (in the rotating frame) is:[9]

$$\hat{\rho}\ (\text{eq}) = \frac{1}{2}\hat{1} + \frac{1}{2}\left(\frac{\hbar\gamma B_0}{k_B T}\right)\hat{I}_z = \frac{1}{2}\hat{1} + \frac{1}{2}\mathbb{B}\hat{I}_z$$

[2-49]

Under an r.f. pulse of general phase and flip angle, the spin-density operator evolves as:[9]

$$\hat{\rho}(t_b) = \hat{R}_{\varphi_\text{p}}(\mu)\hat{\rho}(t_a)\hat{R}_{\varphi_\text{p}}(-\mu)$$

[2-50]

with the rotation operators for each of the *x*, *y*, and *z* axes defined previously. Evolution under rotation about the *z* axis has similar results as for the quantum mechanical description of a single-spin, although now relaxation effects will be included. In the case of transverse relaxation, the coherences evolve as:[9,69]

$$\rho_{\boxed{-}}(t_b) = \rho_{\boxed{-}}(t_a)\exp\{(\text{i}\Omega_0 - \lambda)\tau\}$$

[2-51]

$$\rho_{\boxed{+}}(t_b) = \rho_{\boxed{+}}(t_a)\exp\{(-\text{i}\Omega_0 - \lambda)\tau\}$$

[2-52]

Under longitudinal relaxation, the populations evolve as:[9,69]

$$\rho_{\boxed{\alpha}}(t_b) = \left(\rho_{\boxed{\alpha}}(t_a) - \rho_{\boxed{\alpha}}(\text{eq})\right)\exp\left\{-\frac{\tau}{T_1}\right\} + \rho_{\boxed{\alpha}}(\text{eq})$$

[2-53]

$$\rho_{\boxed{\beta}}(t_b) = \left(\rho_{\boxed{\beta}}(t_a) - \rho_{\boxed{\beta}}(\text{eq})\right)\exp\left\{-\frac{\tau}{T_1}\right\} + \rho_{\boxed{\beta}}(\text{eq})$$

[2-54]

It is appropriate to mention here the concept of phase cycling. Phase cycling is a ubiquitous NMR technique wherein the phases of pulses are methodically and cyclically altered between transients to suppress unwanted signals while maintaining the desired coherence transfer pathways.[70] While the full theory of phase cycling is beyond the scope of this work, understanding the nature of coherences is necessary for appreciating how phase cycling is performed, as determining which pulse phases are to be changed and by how much (while preserving the desired coherence pathway) necessarily requires knowledge of what a coherence pathway is.

2.1.1.4 NMR of Quadrupolar Spins

The concepts used to discuss NMR experiments with spin-1/2 nuclei will now be extended to quadrupolar systems (specifically spin-3/2, although for the most part the main difference for even higher-spin systems is the larger size of the matrices involved). The spin density operator for an ensemble of equivalent spin-3/2 nuclei is a 4 × 4 matrix (since there are now four angular momentum eigenstates available):[9]

$$\hat{\rho} = \overline{|\psi\rangle\langle\psi|} = \begin{pmatrix} \rho_{|+3/2\rangle} & \rho_{\boxed{+1_{+2}}} & \rho_{\boxed{+2_{+2}}} & \rho_{\boxed{+3_{0}}} \\ \rho_{\boxed{-1_{-2}}} & \rho_{|+1/2\rangle} & \rho_{\boxed{+1_{0}}} & \rho_{\boxed{+2_{-2}}} \\ \rho_{\boxed{-2_{-2}}} & \rho_{\boxed{-1_{0}}} & \rho_{|-1/2\rangle} & \rho_{\boxed{+1_{-2}}} \\ \rho_{\boxed{-3_{0}}} & \rho_{\boxed{-2_{+2}}} & \rho_{\boxed{-1_{+2}}} & \rho_{|-3/2\rangle} \end{pmatrix} \quad [2\text{-}55]$$

In addition to coherence order (subscript), the coherences for this spin density operator also have an associated satellite order, which is the difference between the squares of the two Zeeman eigenstates involved (subscript of subscript).[9] There are six single-quantum, four double-quantum, and two triple-quantum coherences, which are represented schematically in Figure 13.

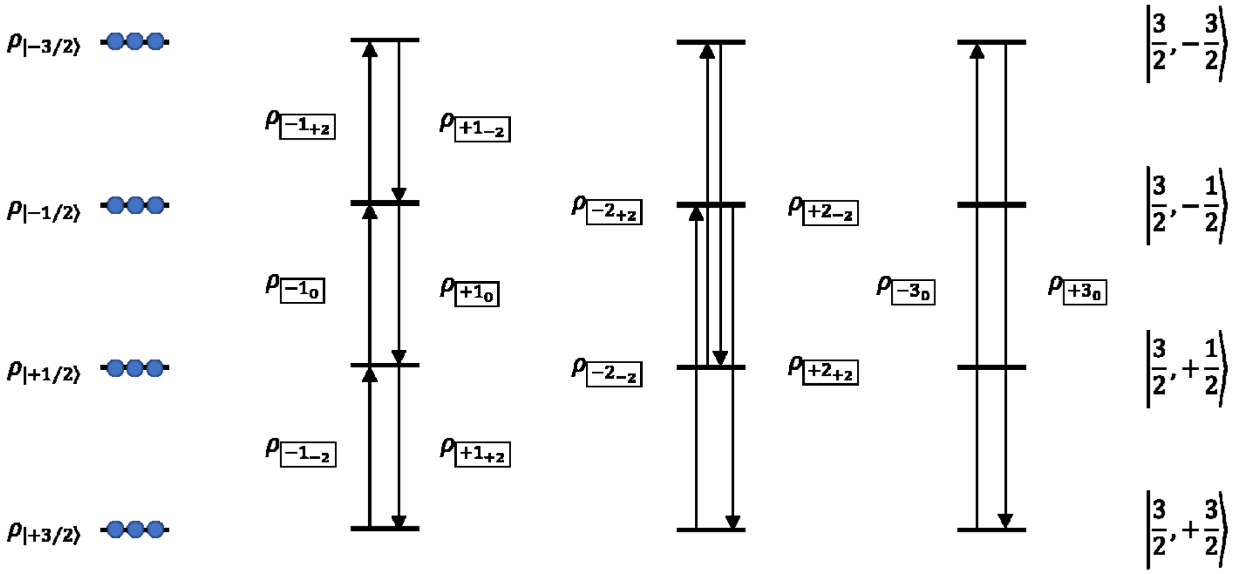

Figure 13: The populations and coherences for a spin-3/2 nuclide. Spin-3/2 nuclides have single, double, and triple-quantum coherences. The populations represent the proportional occupation of states while coherences represent transitions between those states.

The coherence associated with the two innermost eigenstates (± 1/2) is the most important, and is called the central transition (CT). A more general form of the equation for a quadrature-detected NMR signal [2-9] can be proven to be equivalent, and is given as:[9]

$$s(t) \sim 2\mathrm{i}\langle \hat{I}^{+} \rangle \exp\{-\mathrm{i}\varphi_{\mathrm{rec}}\}$$

[2-56]

(where φ_{rec} is the receiver phase) which, after evaluation with the spin-3/2 shift operator (Appendix I), gives the following equation:[9]

$$s(t) \sim 2\mathrm{i}\,\exp\{-\mathrm{i}\varphi_{\mathrm{rec}}\}\left(\sqrt{3}\rho_{\boxed{-1_{-2}}}(t) + 2\rho_{\boxed{-1_{0}}}(t) + \sqrt{3}\rho_{\boxed{-1_{+2}}}\right)$$

[2-57]

The three (-1)-quantum coherences thus contribute differently to the overall signal, with the central transition being the strongest of the three. Note that the angular momentum operators are now of a different dimension (Appendix I).

The effects of a single pulse on a set of equivalent spin-3/2 nuclides will be considered in two limits: where the pulse power is much larger than and where it is much smaller than the first-order quadrupolar interaction. The thermal equilibrium value of the (I = 3/2) spin density operator is:[9]

$$\hat{\rho}(\mathrm{eq}) = \frac{1}{4}\hat{1} - \frac{1}{4}\mathbb{B}\hat{I}_{y}$$

[2-58]

In the strong pulse regime, the density operator after a $(\pi/2)_x$ pulse is:[9]

$$\hat{\rho}(t_b) = \hat{R}_x(\pi/2)\hat{\rho}(\mathrm{eq})\hat{R}_x(-\pi/2) = \frac{1}{4}\hat{1} - \frac{1}{4}\mathbb{B}\hat{I}_{y}$$

[2-59]

(the explicit form of the spin-3/2 rotation operators will be omitted). From the density matrix, the (-1)-quantum coherences can be extracted (the other coherences are unaffected by the pulse):

$$\rho_{\boxed{-1_{+2}}}(t_b) = -\frac{\mathrm{i}\sqrt{3}}{8}\mathbb{B}$$

[2-60]

$$\rho_{\boxed{-1_0}} = -\frac{\mathrm{i}}{4}\mathbb{B}$$

[2-61]

$$\rho_{\boxed{-1_{+2}}} = -\frac{\mathrm{i}\sqrt{3}}{8}\mathbb{B}$$

[2-62]

Substituting the (-1)-quantum coherences back into [2-57] and applying a Fourier transform yields the relative intensities of the CT and satellite transition (ST) peaks:

$$S(\Omega) = \left(\frac{3}{4}\mathbb{B}\,\mathcal{L}\big(\Omega;\Omega_0 + {\omega_\mathrm{Q}}^{(1)},\lambda\big) + \mathbb{B}\,\mathcal{L}(\Omega;\Omega_0,\lambda) + \frac{3}{4}\mathbb{B}\,\mathcal{L}\left(\Omega;\Omega_0 - {{\omega_\mathrm{Q}}^{(1)}}_{l},\lambda\right)\right)$$

[2-63]

where ${\omega_\mathrm{Q}}^{(1)}$ is the first-order quadrupolar coupling (i.e. the magnitude of the transition between the relevant quadrupolar interaction-perturbed Zeeman levels, derived using [1-26]).[9]

To consider the weak pulse limit, one must first consider the rotating-frame spin Hamiltonian for a set of spins experiencing a first-order quadrupolar interaction during an applied *x* pulse:[9]

$$\hat{H} = {\hat{H}_\mathrm{Q}}^{(1)} + \omega_\mathrm{nut}\hat{I}_x = {\omega_\mathrm{Q}}^{(1)}\left(\hat{I}_z^2 - \frac{5}{4}\hat{1}\right) + \omega_\mathrm{nut}\hat{I}_x$$
$$= \begin{pmatrix} \frac{1}{2}{\omega_\mathrm{Q}}^{(1)} & \frac{\sqrt{3}}{2}\omega_\mathrm{nut} & 0 & 0 \\ \frac{\sqrt{3}}{2}\omega_\mathrm{nut} & -\frac{1}{2}{\omega_\mathrm{Q}}^{(1)} & \omega_\mathrm{nut} & 0 \\ 0 & \omega_\mathrm{nut} & -\frac{1}{2}{\omega_\mathrm{Q}}^{(1)} & \frac{\sqrt{3}}{2}\omega_\mathrm{nut} \\ 0 & 0 & \frac{\sqrt{3}}{2}\omega_\mathrm{nut} & \frac{1}{2}{\omega_\mathrm{Q}}^{(1)} \end{pmatrix}$$

[2-64]

Under the secular approximation, which is valid where the nutation frequency is much smaller than the first-order quadrupolar coupling (i.e. in the weak pulse limit) this Hamiltonian can be rewritten as:

$$\hat{H} \cong \begin{pmatrix} \frac{1}{2}\omega_{\mathrm{Q}}{}^{(1)} & 0 & 0 & 0 \\ 0 & -\frac{1}{2}\omega_{\mathrm{Q}}{}^{(1)} & \omega_{\mathrm{nut}} & 0 \\ 0 & \omega_{\mathrm{nut}} & -\frac{1}{2}\omega_{\mathrm{Q}}{}^{(1)} & 0 \\ 0 & 0 & 0 & \frac{1}{2}\omega_{\mathrm{Q}}{}^{(1)} \end{pmatrix}$$

[2-65]

Applied to a spin density operator at thermal equilibrium:[9]

$$\hat{\rho} = \frac{1}{4}\hat{1} + \frac{1}{4}\mathbb{B}\left[\hat{R}_x(\mu^{\mathrm{C}})\hat{I}_z\hat{R}_x(-\mu^{\mathrm{C}})\right]$$
$$= \frac{1}{4}\hat{1} + \frac{1}{4}\mathbb{B}\begin{pmatrix} \frac{3}{2} & 0 & 0 & 0 \\ 0 & \frac{1}{2}\cos\mu^{\mathrm{C}} & \frac{\mathrm{i}}{2}\sin\mu^{\mathrm{C}} & 0 \\ 0 & -\frac{\mathrm{i}}{2}\sin\mu^{\mathrm{C}} & -\frac{1}{2}\cos\mu^{\mathrm{C}} & 0 \\ 0 & 0 & 0 & -\frac{3}{2} \end{pmatrix}$$

[2-66]

where the CT flip angle and nutation frequency are, respectively:[9]

$$\mu^{\mathrm{C}} = \omega^{\mathrm{C}}{}_{\mathrm{nut}}\tau_{\mathrm{p}}$$

[2-67]

$$\omega^{\mathrm{C}}{}_{\mathrm{nut}} = 2\omega_{\mathrm{nut}}$$

[2-68]

Thus, as shown by [2-67] and [2-68], in the ‘weak pulse’ regime the optimum CT selective pulse is half the duration of the corresponding pulse in the ‘strong pulse’ regime (for spin-3/2). For this reason, pulses calibrated on spin-3/2 nuclei in high-symmetry (e.g. cubic) samples must be halved to obtain the equivalent maximally effective pulse for a lower-symmetry (higher-C_Q) compound.

2.1.1.5 Relaxation

As mentioned, the linewidth of an NMR signal is dependent on the transverse relaxation time constant, T_2. Further, the rate of repetition for an experiment depends on the rate at which the spins in the system return to thermal equilibrium, corresponding to the longitudinal relaxation time constant T_1. It would therefore be prudent to briefly discuss relaxation in general, and specifically the quadrupolar relaxation mechanism (with dominates for spin > 1/2 nuclei).

Relaxation depends on oscillations in magnetic (or for quadrupolar relaxation, electric) fields in the environment around the nucleus (although transverse relaxation also depends on inhomogeneity in the static field along z).[9] The most important relaxation mechanisms for spin-1/2 nuclei are the dipole-dipole and CSA mechanisms (in that order; spin-rotation is also a relaxation mechanism but is dominant only in some very specialized cases).[9] For spin > 1/2 nuclei, the quadrupolar relaxation mechanism is usually overwhelmingly dominant over the others.[71] The non-quadrupolar relaxation mechanisms depend on fluctuating local magnetic fields, which depend strongly on molecular motion; the correlation time τ_c is associated with the rate of motion (correspondingly, large molecules and solids have larger correlation times than small molecules in solution). A plot of T_1 and T_2 values as a function of correlation time is included in Figure 15. Note that practically, the transverse relaxation must be equal to or faster than longitudinal relaxation.[9,69] The equations for non-quadrupolar relaxation rates are provided:[69]

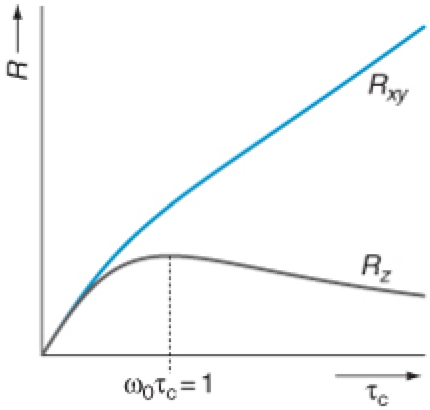

Figure 15: Plot of relaxation constants (where R_{xy} = 1/T_2 and R_z = 1/T_1) as a function of correlation time for a spin-1/2 nuclide. Reproduced by permission from John Wiley and Sons (ref. 69), copyright (2010).

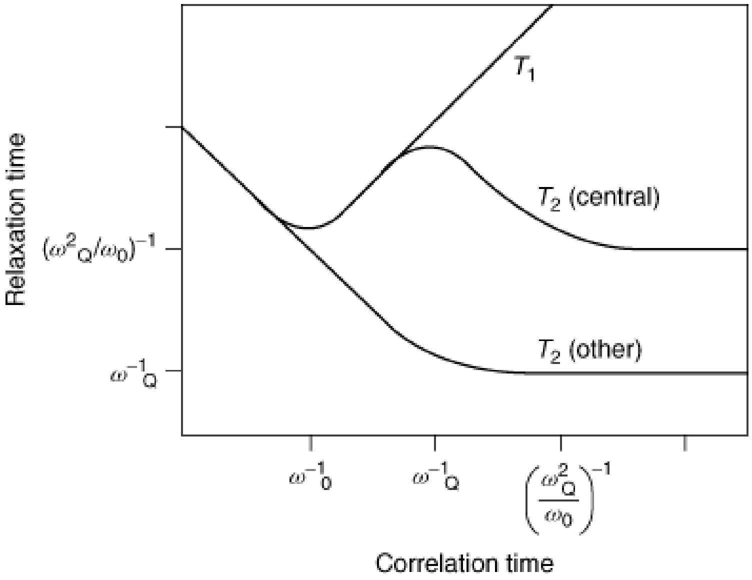

Figure 14: Relaxation times as a function of correlation time for spin > 1/2 nuclides. Note that at large correlation times the transverse relaxation for the central transition behaves differently from the other transitions. In terms of longitudinal relaxation, the same minimum is observed when τ_c^{-1} is equal to the Larmor frequency as seen for the non-quadrupolar case (Figure 15). Reproduced by permission from John Wiley and Sons (ref. 71), copyright (2012).

Slow motion limit (transverse): $\frac{1}{T_2} = \gamma^2[B_{\mathrm{loc}}^2]\tau_{\mathrm{c}}$

[2-69]

Slow motion limit (longitudinal): $\frac{1}{T_1} = 2\gamma^2[B_{\mathrm{loc}}^2]/(\omega_0^2\tau_{\mathrm{c}})$

[2-70]

Fast motion limit: $\frac{1}{T_2} = \frac{1}{T_1} = 2\gamma^2[B_{\mathrm{loc}}^2]\tau_{\mathrm{c}}$

[2-71]

The local magnetic field term depends on the interaction; specific expressions will not be provided as this is not considered necessary for understanding the generalities of relaxation processes. Given that the work in this thesis made use of non-viscous solutions or crystalline solids, descriptions of relaxation in the fast and slow motion limits will suffice.

Quadrupolar relaxation depends on local electric, rather than magnetic, fields and the magnitude of the quadrupole moment interacting with those fields, and must therefore be treated separately. The quadrupolar mechanism is extremely efficient because the electric field gradient around a nucleus exists continuously and is mostly intramolecular in origin, and because quadrupolar coupling is usually a much higher energy interaction than the others. Providing an expression for the longitudinal relaxation of a quadrupolar nucleus, especially in anisotropic solids, is not trivial because the relaxation will depend on both the CT and ST coherences.[71] However, the magnitude of these transition rates are usually similar enough that a simplified, general equation for longitudinal relaxation can be provided:

$$\frac{1}{T_1} = \omega_{\mathrm{Q}}^2\left(\frac{a\tau_{\mathrm{c}}}{1+\omega_0^2\tau_{\mathrm{c}}^2} + \frac{b\tau_{\mathrm{c}}}{1+4\omega_0^2\tau_{\mathrm{c}}^2}\right)$$

[2-72]

where *a* and *b* are constants that are proportional to the amplitude of EFG fluctuations experienced by the spin, and ω_{Q} is the quadrupolar coupling.[71] In the case of transverse relaxation, central and satellite transitions exhibit differing relaxation rates, especially in the slow-motion limit. In the fast-motion limit, transverse quadrupolar relaxation can be described by:

$$\frac{1}{T_2} = c\omega_{\mathrm{Q}}^2\tau_{\mathrm{c}} \tag{2-73}$$

where *c* is a motion-model dependent constant.[71] In the slow-motion limit, the satellite and central transition relaxation rates approach constant (though different) values:[71]

$$\text{Satellite transitions:} \quad \frac{1}{T_2} = \omega_{\mathrm{Q}} \tag{2-74}$$

$$\text{Central transition:} \quad \frac{1}{T_2} = \frac{\omega_{\mathrm{Q}}^2}{\omega_0} \tag{2-75}$$

The quadrupolar relaxation times are plotted as a function of relaxation rate in Figure 14. Of importance to note is the fact that for both quadrupolar (Figure 14) and non-quadrupolar (Figure 15) relaxation mechanisms, longitudinal relaxation is most efficient when the correlation time is the inverse of the Larmor frequency of the nucleus.

Heteronuclear decoupling, wherein the spins of one set of nuclei are saturated with r.f. irradiation while the detected nuclei are not, is not only important for significantly reducing acquisition times by removing *J* coupling patterns from NMR spectra, but can also have important effects for relaxation. This is mainly because the saturated nuclei are prevented, to a degree, from influencing the relaxation of the detected nuclei (i.e. by suppressing the local fields generated by those nuclei), which can be useful for quick relaxing (especially quadrupolar) nuclei.[17] This is because decreasing the relaxation rate by even a small amount can significantly lessen difficulties in manipulating spins for very fast relaxing species.

2.1.2 Solid-State (SS)NMR Spectroscopy

The presence of anisotropic terms further complicates NMR spectroscopy, particularly of powdered samples (which are a focus of this thesis). While a complete discussion of this field is, by necessity, beyond the scope of this work, care will be taken to focus on the techniques employed to maximize the utility of NMR in the solid state. Specifically, the ability to remove anisotropic effects through magic-angle spinning (MAS) NMR and the use of echo experiments to maximize signal from rapidly relaxing nuclei will be detailed.

2.1.2.1 Magic-Angle Spinning (MAS) NMR

The major difference between NMR in the solid state, as opposed to NMR spectroscopy of solutions, is the presence of angular dependence in many of the NMR interaction Hamiltonians discussed in Chapter 1. However, because many of the angular terms are dependent on the Legendre polynomial ($1 - 3\cos^2\theta$), they can be time-averaged to zero (or, practically speaking, at least reduced significantly) by spinning at an angle of 54.74° (the 'magic angle'). The axis system in Figure 16, which is with respect to the rotor (sample) frame, can be used to show that the chemical shift anisotropy [1-14], first-order quadrupolar coupling [1-26], and heteronuclear direct dipolar coupling [1-44] can be effectively averaged by spinning at the magic angle (although the second-order quadrupolar Hamiltonian, based on the perturbation in [1-27], requires maniuplation about two axes in order to be completely averaged out by

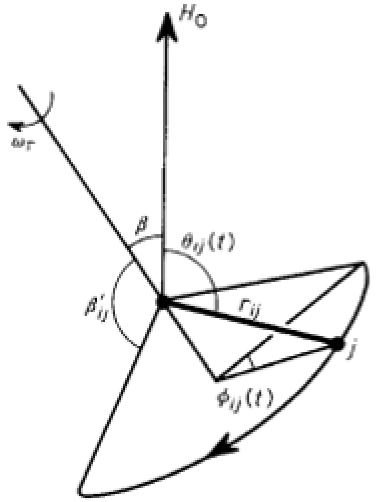

Figure 16: Co-ordinate system for the discussion of magic angle spinning. Note that H_0 is an older formalism for the external magnetic field B_0. r_{ij} is the rotating interaction vector (in the case of direct dipolar coupling this is the internuclear axis). Other terms are defined in-text (see [2-76]). Reproduced by permission from Taylor and Francis (ref. 14), copyright (1981).

mechanical means).[16,72] The angle between the interaction vector and the external magnetic field, $\theta_{\mathrm{i,j}}$, can be written in terms of the other angles in the system:

$$\cos\theta_{\mathrm{i,j}} = \cos\beta\cos{\beta'}_{\mathrm{i,j}} + \sin\beta\sin{\beta'}_{\mathrm{i,j}}\cos(\omega_{\mathrm{r}}t + \varphi_{\mathrm{i,j}}(0)) \tag{2-76}$$

where β is the fixed angle of the sample with respect to the external magnetic field, ${\beta'}_{\mathrm{i,j}}$ is the angle between the rotation axis and the interaction vector, ω_{r} is the sample rotation angular frequency, and $\varphi_{\mathrm{i,j}}(0)$ is the initial position of the axis of rotation (corresponding to Figure 16).[14] Equation [2-76] can be substituted into the equations for the interaction Hamiltonians and expanded out to show which terms average to zero under MAS. For example, with the case of heteronuclear dipolar coupling [1-44]:[14]

$$\begin{aligned}\widehat{H} = hR(\hat{I}_{1,z}\hat{I}_{2,z})[&\frac{1}{2}(3\cos^2\beta - 1)\left(3\cos^2{\beta'}_{\mathrm{i,j}} - 1\right)\\ &+\frac{3}{2}\sin(2\beta)\sin\left(2{\beta'}_{\mathrm{i,j}}\right)\cos(\omega_{\mathrm{r}}t + \varphi_{\mathrm{i,j}}(0))\\ &+\frac{3}{2}\sin^2\beta\sin^2{\beta'}_{\mathrm{i,j}}\cos 2(\omega_{\mathrm{r}}t + \varphi_{\mathrm{i,j}}(0))]\end{aligned} \tag{2-77}$$

The first angular term $\frac{1}{2}(3\cos^2\beta - 1)\left(3\cos^2{\beta'}_{\mathrm{i,j}} - 1\right)$ is zero when β is the magic angle. The other two angular terms are periodic in ω_{r} and $2\omega_{\mathrm{r}}$ respectively and produce spinning sidebands at frequencies that are multiples of ω_{r}.[14] The first order quadrupolar interaction [1-26] likewise can be effectively averaged under MAS, though the magnitude of the interaction is often large enough that spinning sidebands are observed even at high speeds.[12,72] The CSA can be shown to behave similarly.[16,72]

MAS NMR spectroscopy is achieved by using specialized probes which use a system of pressurized gas lines to support and spin a rotor (usually a zirconia cylinder with plastic cap(s)). The use of an optical feedback system allows for precise determination of the spinning rate and, with modern consoles, automated maintenance of that speed. Calibration of the magic angle is usually performed by mechanically adjusting the angle of rotation and optimizing the echo train or sideband envelope of a cubic and highly receptive quadrupolar sample (the ^{79}Br resonance of KBr is preferred), although one probe encountered during this work made use of a calibrated Hall effect sensor and pneumatic support to measure and adjust, respectively, the magic angle. In general, faster spinning speeds require smaller rotors, which can lead to some trade offs in terms of effective averaging of anisotropic interactions against the amount of sample available for measurement. In fact, while probes capable of spinning speeds greater than 100 kHz are commercially available, their sample volumes (on the order of tenths of microliters) make them unsuitable for most low-receptivity nuclides. As a result, this study used only 7 mm and 4 mm outer-diameter (o.d.) rotors for ^{61}Ni MAS NMR experiments; using a reduced-volume (thick-walled) 4 mm o.d. zirconia rotor allowed for an exceptionally high spinning speed of 18 kHz (which was necessary for the broadest spectrum), compared to a 5 kHz operational limit for standard 7 mm rotors.

In addition to physical limits on spinning speed, which affect the effectiveness of line-narrowing, MAS NMR has some other drawbacks. Firstly, as mentioned, second order quadrupolar coupling is not removed, nor is homonuclear dipolar coupling (although given the distance dependence of dipolar coupling and the fact that only ^{31}P among nuclides measured in the solid state has high enough natural abundance for this to be a factor, it was not particularly concerning). Secondly, spinning sidebands may be introduced which can increase spectral clutter and remove intensity from the central (isotropic) peak. Lastly, MAS demands a sacrifice of information for the sake of clarity.[72] Narrowing produces spectra which may be easier to measure and interpret, but it also removes line shape features stemming from dipolar, quadrupolar, and CSA effects which can provide physicochemical information; in general, it is not possible to remove one kind of interaction from the spectrum while preserving others without the use of specialized experiments.

2.1.2.2 Basic Echo Experiments

Of tremendous importance for more complicated NMR experiments, both in solution and the solid state, is the use of echo pulses for refocusing and preserving magnetization. It can be particularly important for quickly relaxing species as it allows for magnetization to decay before reappearing after a time interval (hence ‘echo’). The Hahn echo is the most commonly used in solution and involves the use of a $\pi/2$-π pulse sequence, and its refocusing effect can be explained using the vector model. While other variations on the echo sequence can have different quantum mechanical justifications, the echo motif itself is ubiquitous (a general echo sequence is provided as Figure 17). Given that the solution studies carried out in this work were exclusively single-pulse experiments with proton-decoupling as necessary, the discussion of echoes will be focused on their uses in SSNMR spectroscopy.

In general, the Hahn (or spin-) echo is useful for refocusing CSA or heteronuclear dipolar coupling, but is insufficient for nuclei with significant quadrupolar interactions (or homonuclear dipolar coupling). As a result, complete refocusing of magnetization requires a modified echo sequence for the quadrupolar ^{61}Ni nuclide that is the focus of this thesis. Refocusing of the magnetic shielding and heteronuclear dipolar interactions, and off-resonance and field inhomogeneity artifacts, occurs when the following condition is satisfied:

$$\tau_4 = (r - c)\tau_2 \tag{2-78}$$

where (*r, c*) is the coherence in a spin-density matrix (with index row *r* and column *c*), and the time periods τ are as defined in Figure 17.[73] On the other hand, the first order quadrupolar interaction is refocused when:[73]

$$(2m-1)\tau_4 = (r^2 - c^2)\tau_2$$

[2-79]

Lastly, the second-order quadrupolar interaction requires satisfaction of [2-79] as well as:[73]

$$(3m^2 - 3m + 1)\tau_4 = (r^3 - c^3)\tau_2$$

[2-80]

Only one coherence pathway can satisfy all these conditions simultaneously, and is readily selected by use of a tabulated phase cycle.[73] To hold off on the refocusing of the echo until all three conditions are met, it is advisable to use a CT-selective pulse, as discussed earlier for spin-3/2. For the more general case, the central transition is best excited by a radiofrequency pulse of strength:

$$\nu_{\pi/2} \sim \frac{\Delta}{I + \frac{1}{2}}$$

[2-81]

where Δ is the static CT linewidth (in Hz).[73] The effects of pulse power on line shape for a quadrupolar echo pulse sequence is displayed in Figure 18.

It should be noted that the quadrupolar echo sequence refocuses all the aforementioned interactions, but that the CT-selective pulse is only necessary to prevent distortion in the case when the quadrupolar coupling is dominant in defining the line shape. Thus, it is possible at times to obtain good powder patterns without CT-selective pulses (particularly for narrow or small-C_Q lines), and thus the pulse lengths can be adjusted to either maximize signal-to-noise or excitation bandwidth without fear of line shape distortion. In fact, as shown in Figure 18, for spin-3/2 nuclei with a C_Q of 5.2 MHz, the distortion in the line shape is modified by two- and

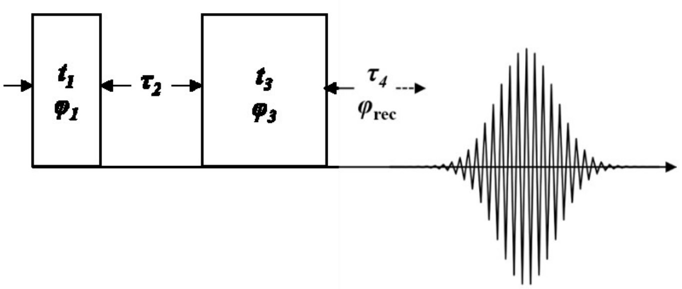

Figure 17: The general form of an echo pulse sequence. The numbering scheme is consistent with equations [2-78] to [2-80]. t_1 and t_3 are pulse lengths, φ_1 and φ_3 are pulse phases, τ_2 is the delay between the initial excitation and refocusing pulses, and signal acquisition occurs during τ_4. φ_{rec} is the receiver phase.

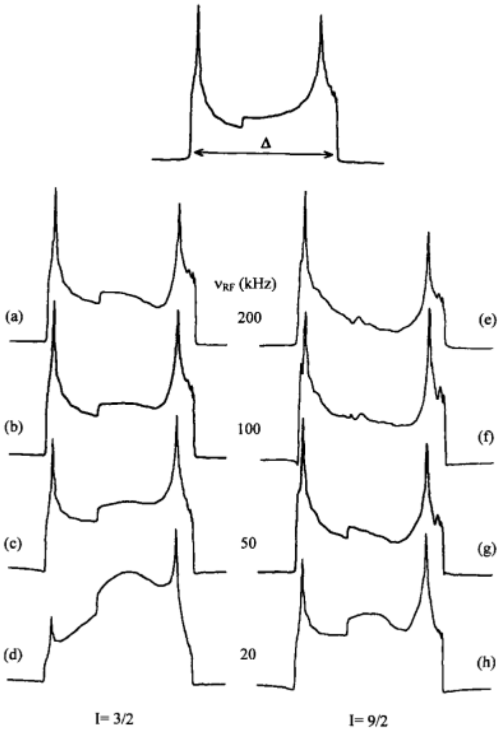

Figure 18: Calculated spectra for a quadrupolar echo sequence as a function of pulse power (a-h). For the purposes of this work, attention should be paid to the spin-3/2 case (a-d). Distortions are relative to a perfect single-pulse experiment of linewidth Δ = 200 kHz at the top of the figure. C_Q = 5.2 MHz and η = 0.1 for the spin-3/2 simulations. Reproduced by permission from Taylor and Francis (ref. 73), copyright (2000).

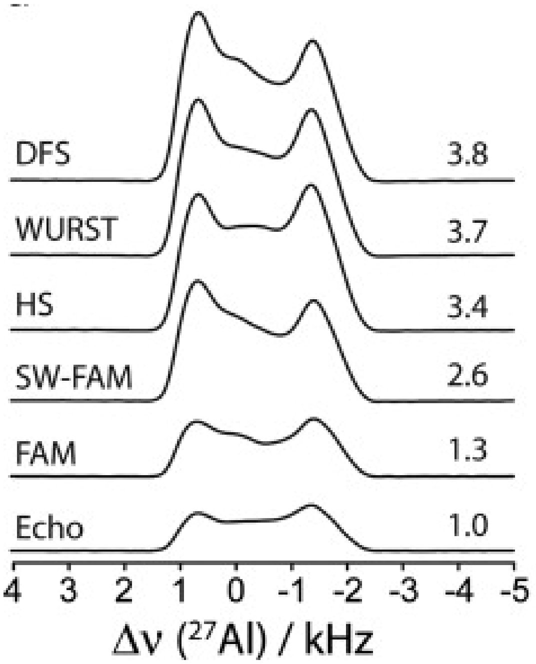

Figure 19: ^{27}Al (I = 5/2) SSNMR signal enhancements for Al(acac)$_3$ under static conditions. DFS refers to a double-frequency sweep experiment, WURST to a wideband uniform-rate smooth truncation sequence, HS to a hyperbolic secant inversion experiment, FAM to fast amplitude modulation, and SW-FAM to a swept FAM sequence. Significant signal enhancements are obtained, but the line shape varies considerably depending on the type of population transfer experiment. Adapted by permission from Elsevier (ref. 74), copyright (2013).

four-fold increases in pulse power from 50 to 100 and 200 kHz, but the deviation from the ideal single $\pi/2$-pulse experiment is actually more noticeable.

Echoes can also be used in combination with MAS, although in such cases the pulses must be rotor synchronized – that is to say, the pulses must occur such that the rotor is at the same angle each time a particular pulse in the sequence is applied. To understand why, consider what would happen if the pulsing occurred at arbitrary time points: in this case, the rotor during any given pulse will have its crystallites in different orientations relative to other pulses, and the anisotropic interactions encoded during the time the echo evolves will be different. As a result, instead of rotation producing a line shape where anisotropic interactions are time-averaged over each rotor period, the anisotropic interactions will be reintroduced into the echo, and by extension, the spectrum.

Removal of the second order quadrupolar broadening requires either specialised hardware capable of rotationally averaging both angular dependencies for the interaction, or the use of specialized pulse sequences such as multiple-quantum MAS (MQMAS). The latter technique has the advantage of being compatible with traditional MAS hardware, and thus imposes no physical limits on rotation frequency.[16] Nevertheless, MQMAS, despite its ability to effectively remove second order quadrupolar broadening, was not attempted for ^{61}Ni NMR spectroscopy in this work because of the low efficiency in converting between single and multiple quantum coherences and the potential for line shape distortion.[16] Given the acquisition times required for some of the relatively narrow lines encountered here, and the notable but relatively moderate quadrupolar coupling constants measured, removal of second-order quadrupolar broadening by MQMAS was not expected to be practicable.

2.1.2.3 The Carr-Purcell-Meiboom-Gill (CPMG) Experiment

Signal enhancement techniques, with a focus here on half-integer-quadrupole-specific techniques (most of which involve polarization transfer from the satellite transitions to the central transition), as well as more generally applicable (at least in terms of spin-number) polarization transfer methods (such as cross-polarization (CP) and dynamic nuclear polarization (DNP)) have been established in the literature as a means to improve acquisition times for very broad NMR spectra or for unreceptive nuclides.[17,74] At the same time, there is a tendency for satellite population transfer pulse sequences to be susceptible to line shape distortions (Figure 19). Given that the goals of this thesis included characterizing the structural environment in select nickel compounds using ^{61}Ni SSNMR (thus requiring confidence in the final line shape), and that the overall sensitivity enhancement benefits were unlikely to be large (since ^{61}Ni is a spin-3/2 nuclide, with fewer satellite transitions from which intensity can be transferred to boost the central transition), satellite-transition-based polarization transfer techniques were not attempted.

In terms of the more general polarization transfer techniques, CP was not attempted for any nickel-61 NMR experiments due to the absence of abundant ^{1}H nuclei close to the metal

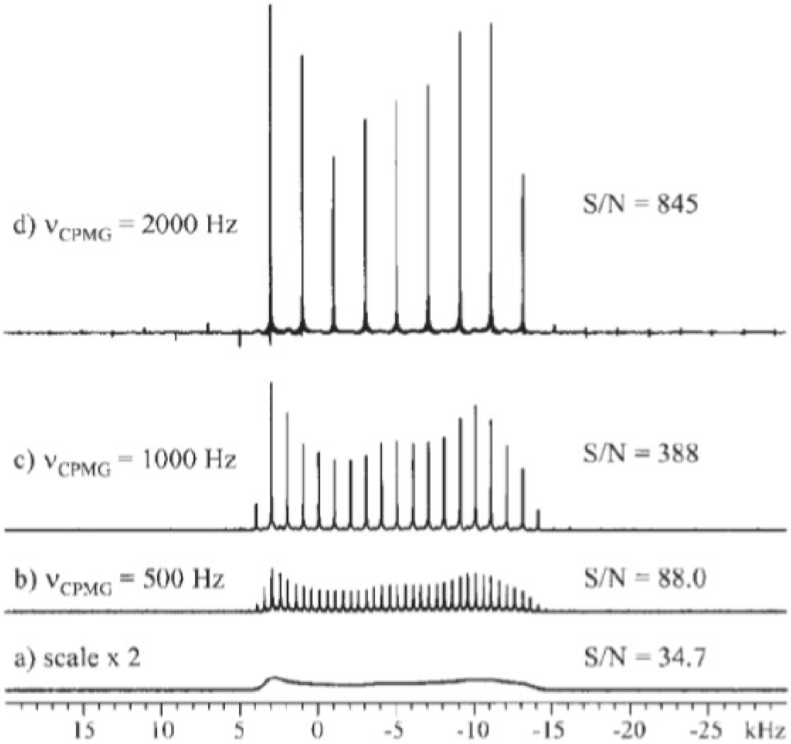

Figure 20: Signal enhancement obtained for a wideline ^{87}Rb SSNMR spectrum of $RbClO_4$ using the QCPMG experiment. The number of scans is the same for each spectrum, showing the increase in S/N from a) the echo experiment through increasing spikelet separations (b-d). At some point, one begins to lose significant line shape information by virtue of the large spikelet separation. Reproduced by permission from John Wiley and Sons (ref. 75), copyright (2010).

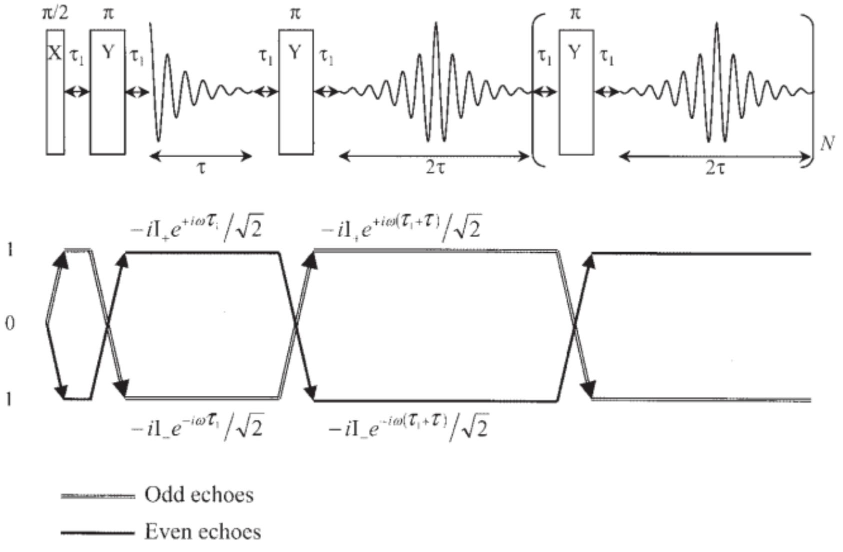

Figure 21: The CPMG pulse sequence and its associated coherence transfer pathway for a (m = -1/2 to m = +1/2) transition. Spin product operators are included with the coherence pathway diagram. Reproduced by permission from John Wiley and Sons (ref. 75), copyright (2010).

center in the structures studied (^{31}P spins, while present, resonate at such much lower frequency than ^{1}H and as a result tuning to both ^{61}Ni and ^{31}P was not possible with the probes available; at any rate, cross-polarization would be complicated by the relative relaxation rates of the two nuclides, as mentioned in Section 1.3.2). DNP on the other hand, requires extremely complex and expensive hardware to set up, and is otherwise still a relatively narrowly applicable technique.

As opposed to 'true' signal enhancement techniques, the CPMG experiment (or quadrupolar analogue, QCPMG, which will be used interchangeably) tends to produce fewer line shape distortions while still providing order-of-magnitude level signal-to-noise improvement over traditional pulse sequences.[74,75] The original use of the CPMG experiment was to reduce the effects of translational diffusion on the measurement of T_2 values in solution,[76,77] but Garroway[78] demonstrated that the series of echoes (produced by the train of refocusing pulses which are endemic to CPMG experiments) observed in the time-domain could be Fourier-transformed to produce a spikelet pattern outlining the shape of a wide solid-state spectrum. The overall S/N improvement of the QCMPG spikelet pattern versus a complete spectrum will depend on the rate of decay of the echo-train ($1/T_2$), the number of echoes acquired, and the acquisition time for each individual echo (i.e. the spikelet separation ν_{CPMG}).[75] In general, there is a limit to how closely the spikelets can be spaced for a given sample and nuclide before the S/N benefits become negligible because the original source of the 'signal enhancement' in the QCPMG experiment is the concentration of the full integrated intensity of the corresponding single-echo spectrum into a series of sharp peaks.[75] Figure 20 shows the S/N enhancement obtained for the ^{87}Rb NMR spectrum of $RbClO_4$ using QCPMG experiments, while Figure 21 demonstrates the pulse sequence itself and its coherence pathways.

2.2 Density Functional Theory (DFT) Computations

A brief overview of density functional theory (DFT) quantum chemical computations will now be provided. While an effort will be made to be as thorough as possible, a full overview of this field would take up many volumes and therefore only the basic theory will be described, with a focus on the application of DFT calculations to ^{61}Ni NMR.

2.2.1 Theoretical Basics of DFT Computations

2.2.1.1 Hartree-Fock (HF) Theory

One of the great achievements of quantum theory is the Schrödinger equation, which together with the wavefunction can describe the behaviour and state of a system (indeed, of arbitrary size) in its entirety. Nevertheless, when it comes to solving the Schrödinger equation, an analytical solution for anything but hydrogenic atoms becomes impracticably difficult. For this reason, quantum computations must take advantage of approximations and simplifications where possible (in the spirit seen earlier in the discussion of NMR). Key among these, in a computational chemistry sense, is the Born-Oppenheimer approximation. The Born-Oppenheimer approximation allows for separation of the electronic and nuclear components of the wavefunction, thanks to their physical differences and the timescales of motion for each:

$$\hat{H} = -\frac{\hbar^2}{2m_e}\sum_{i}^{electrons}\nabla_i^2 - \frac{\hbar^2}{2}\sum_{A}^{nuclei}\frac{1}{M_A}\nabla_A^2 - \frac{e^2}{4\pi\varepsilon_0}\sum_{i}^{electrons}\sum_{A}^{nuclei}\frac{Z_A}{r_{iA}} + \frac{e^2}{4\pi\varepsilon_0}\sum_{i>j}^{electrons}\sum_{j}^{electrons}\frac{1}{r_{ij}} + \frac{e^2}{4\pi\varepsilon_0}\sum_{A>B}^{nuclei}\sum_{B}^{nuclei}\frac{Z_A Z_B}{R_{AB}}$$

[2-82]

where m_e is the electron rest mass, Z_A is the nuclear charge, M_A is the nuclear mass, R_{AB} is the internuclear distance, r_{ij} is the interelectronic distance, r_{iA} is the distance between the respective electron and nucleus, and ε_0 is the permittivity of free space.[79] The nuclear-nuclear interactions produce only a constant (Coulombic) term and therefore the electronic Hamiltonian is:[79]

$$\hat{H}_{electronic} = -\frac{\hbar^2}{2m_e}\sum_{i}^{electrons}\nabla_i^2 - \frac{\hbar^2}{2}\sum_{A}^{nuclei}\frac{1}{M_A}\nabla_A^2 - \frac{e^2}{4\pi\varepsilon_0}\sum_{i}^{electrons}\sum_{A}^{nuclei}\frac{Z_A}{r_{iA}} + \frac{e^2}{4\pi\varepsilon_0}\sum_{i>j}^{electrons}\sum_{j}^{electrons}\frac{1}{r_{ij}}$$

[2-83]

However, this still leaves all the electrons and interactions between them to be accounted for. A second simplification can be assumed, called the Hartree-Fock approximation, wherein all the electrons in the system are assumed to move independently of each other.[79] Instead, any individual electron feels only the average electric field generated by the other electrons. Practically, this necessitates expressing individual electrons as functions termed spin orbitals, which are gathered in a single determinant called the Slater determinant:[79]

$$\Psi = \frac{1}{\sqrt{n!}}\begin{vmatrix} \chi_1(1) & \chi_2(1) & \dots & \chi_n(1) \\ \chi_1(2) & \chi_2(2) & \dots & \chi_n(2) \\ \dots & \dots & \dots & \dots \\ \chi_1(n) & \chi_2(n) & \dots & \chi_n(n) \end{vmatrix}$$

[2-84]

The Slater determinant also implicitly includes the Pauli exclusion principle; if one were to attempts to include two spin orbitals with the same overall state in the same row of the determinant, the entire determinant would evaluate to zero.[79]

The Hartree-Fock approximation produces a set of differential equations, each representing one electron. These can be represented as a set of algebraic equations by treating the spin orbital for a molecule as a linear combination of atomic orbitals (LCAO):

$$\psi_i = \sum_{\mu}^{basis\,functions} c_{\mu i}\varphi_\mu \tag{2-85}$$

where ψ_i is a molecular orbital (not including the spin of the χ term) and $c_{\mu i}$ are initially unknown molecular orbital coefficients.[79] The LCAO is described in terms of a series of well-behaved functions φ_μ (called basis functions, drawn from a basis set).[79] The lowest-energy set of molecular orbitals is obtained by performing a self-consistent field (SCF) procedure:[79]

1) An initial guess set of orbital functions is used to calculate the effective potential.
2) The effective potential is used to calculate the energy and improved orbital functions for each of the electrons in the system.
3) The improved orbital functions are used to calculate a new effective potential, followed by a new set of orbital functions, and so on.
4) Once the solutions and energies do not change to the precision of a predetermined threshold (i.e. the solutions become self-consistent), the orbitals and energies are finalized.

The total energy of the system can then be extracted from this information. For a geometry optimization calculation, for instance, a similar approach can be extended to changes in nuclear positions (with the total electronic energy calculated for each set of nuclear positions), as a result of the Born-Oppenheimer approximation.

2.2.1.2 Density Functional Theory (DFT)

A main drawback of the Hartree-Fock method is that it is quite computationally demanding. Density functional theory (DFT) is a significant computational improvement that takes advantage of the exact solution available for a many-electron system of uniform spatial density (a uniform 'electron gas').[79] The total HF energy can be written as the sum of four terms:

$$E^{HF} = E_T + E_V + E_J + E_K \tag{2-86}$$

where E_T is the kinetic energy term, E_V is the electron-nuclear potential energy, E_J is the electronic Coulomb term, and E_K is the electronic exchange term.[79] The total DFT energy carries over the first three terms, but the HF exchange energy is replaced by an exchange/correlation energy term:[79]

$$E^{DFT} = E_T + E_V + E_J + E_{XC} \tag{2-87}$$

Apart from the kinetic energy, all the terms depend on the total electron density:[79]

$$\rho(\mathbf{r}) = 2 \sum_{i}^{orbitals} |\psi_i(\mathbf{r})|^2 \tag{2-88}$$

Because the terms depend on the position of the electrons, which stem from the idealized many-electron gas problem, the spin state does not factor into calculations (which reduces computational demand). Otherwise, the first three terms are calculated using orbitals and basis functions similar to the Hartree-Fock method.[79] The exchange/correlation functional is a correction term obtained by fitting the density produced from the idealized electron gas problem to a function, although better models also fit the gradient of the electron density.[79] The total energy can then be minimized using a variation of the SCF procedure described for HF computations.

2.2.2 ZORA, GIAO and GIPAW DFT Methods

Due to the diverse nature of the variables one can desire to calculate in computational chemistry, different flavours of DFT methods have emerged to deal with different types of calculations or systems. These will only be superficially discussed, with the purposes and uses of each emphasized, given the complexity and length of the mathematics involved.

Zeroth order regular approximation (ZORA) DFT uses the Dirac equation, which includes both quantum mechanical and relativistic effects (specifically, it uses the zeroth order regular approximation to the Dirac equation).[80–84] As such it is useful for calculations involving heavier elements (particularly where *f* orbitals may be involved). Additionally, effects from spin-orbit coupling (where electron magnetic moments interact with the magnetic field generated by their own motion) can be included to improve the precision of spectroscopic calculations (including for NMR).[83,85]

When performing quantum chemical calculations on magnetic properties, it is common to encounter an unphysical dependence of the results on the position of the molecule in the magnetic field.[86] This stems from the fact that the z axis magnetic field produces infinitesimal rotation of atomic orbitals and is defined with respect to a particular coordinate origin.[86] For atomic orbitals close to the origin, the basis can suitably describe these infinitesimal changes.[86] However, farther out from the origin standard basis sets become insufficient to describe the perturbed atomic orbitals.[86] This, called the gauge problem, can be solved by including magnetic field dependence in the atomic basis function.[86] Resulting DFT calculations are said to take advantage of gauge-including atomic orbitals (GIAO); the usefulness of GIAO DFT for NMR calculations is implicit.

Gauge including projector augmented-waves (GIPAW) DFT calculations are useful for periodically repeating structures (such as crystals) as they can include effects from long-range interactions using periodic boundary conditions.[87] Pseudopotentials are used to reduce computational intensity by replacing non-valence electrons with an effective potential. The major concern with the use of pseudopotentials for NMR calculations is that they do not capture electronic structure and motion adequately at the core, but the use of Blöchl's projector augmented-wave (PAW) approach to electronic structure[88] has been demonstrated to be a suitable approach for the use of pseudopotentials in spectroscopic calculations.[87]

2.2.3 DFT Computations for Nickel-61 NMR

While the selection of a functional in particular is not trivial, previous work in assessing the suitability of various functionals to nickel compound geometry optimization and ^{61}Ni NMR parameter calculation has already been done, specifically by Bühl et al. In their 2009 article they provide a holistic attempt at calculating ^{61}Ni NMR parameters for gas-phase structures, using methods and basis sets consistent with previous literature on first-row transition metal elements. They optimized geometries using Becke's and Perdew's BP86/AE1 functional (despite

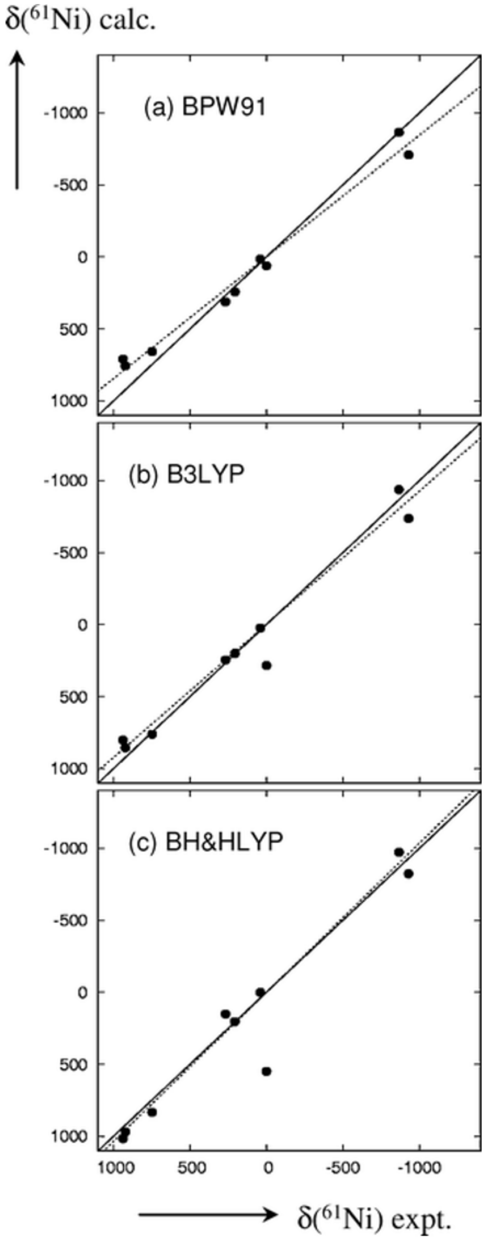

Figure 22: Experimental/theoretical correspondence of ^{61}Ni chemical shifts calculated by Bühl et al. Their GIAO DFT computations show improvement with higher HF mixing (from a) to c)), but note the increase in error for $Ni(CO)_4$ at 0 ppm $\delta(^{61}Ni)$ expt. contrary to the overall improvement in the fit (shown by the dotted line; perfect correlation is represented by the solid line). Reproduced by permission from The Royal Society of Chemistry (ref. 64), copyright (2009).

suggesting that a more modern functional may have provided better results, the authors chose the BP86 functional to keep in line with previous first row transition metal NMR studies), an augmented Wachters basis for nickel, and 6-31G(d) basis for other elements in the compounds studied which are relevant to this thesis (including: $Ni(CO)_4$, $Ni(C_2H_4)_2(PMe_3)$, $Ni(cod)_2$, $Ni(PF_3)_4$, $Ni(PMe_3)_4$, and $Ni(PCl_3)_4$).[64] Magnetic shieldings were evaluated using GIAO DFT and the BPW91, B3LYP, and BHandHLYP functionals (with each functional individually for each compound).[64] The same Wachters basis was used for nickel, while hydrogen magnetic shieldings were computed using a DZ (double-zeta) basis and an IGLO (individual gauge for localized orbitals) basis II was used for other elements.[64] Electric field gradients were computed by Bühl et al. at the B3LYP/II' level.[64]

While their specific results will be presented later in assessing experimental and computational NMR parameters determined during this Master's work, some of the authors' specific methods and observations are worth noting. Changing from a B3LYP to BHandH functional (both of which are hybrid functionals, with part of the exchange term coming directly from HF theory), which represents an increase from 20% to 50% HF exchange in the functional, removed systematic underestimation of high-frequency and overestimation of low-frequency shifts, but increased the paramagnetic contributions in $Ni(CO)_4$ selectively (as seen in Figure 22).[64] This caused the chemical shift of the reference to be drastically overestimated relative to the other compounds modeled. For this reason, the authors adopted an indirect referencing scheme wherein the theoretical nickel-61 chemical shifts were obtained for the compounds studied by fitting a linear equation to the plot of the computed shielding values as a function of experimentally known $\delta_{iso}(^{61}Ni)$ values (excluding of course $Ni(CO)_4$), and using that equation to calculate the theoretical reference shielding for an experimental chemical shift of 0 ppm (i.e. to find the reference shielding).[64] Regardless, the authors note that B3LYP and BHandHLYP produce similar errors, and given that the B3LYP functional is used for the majority of transition metal nuclei in literature, recommend it for use with ^{61}Ni shielding calculations as well.[64] Further, Bühl et al. write that the benefits of HF exchange appear to increase with later transition metal nuclei,[89,90] and that nickel fits this trend.[64]

2.3 Procedural Details

2.3.1 NMR Spectroscopy

$Ni(cod)_2$, $Ni(PPh_3)_4$ (with purity quoted as approximately 4-7% Ni), and $Ni[P(OPh)_3]_4$ were purchased from Sigma-Aldrich and used without further purification (the structures of these compounds are provided as Figure 23. $Ni(cod)_2$ was purchased in two lots: the first consisted of coarse olive-grey crystals while the second was composed of fine yellow crystals. Experiments using the first lot of $Ni(cod)_2$ were hindered by significant oxygen sensitivity, and attempts to dissolve the material in benzene-d6 resulted in almost immediate plating of nickel metal on the container. The physical characteristics of the second lot of $Ni(cod)_2$ were consistent with literature.[91] $Ni(PPh_3)_4$ and $Ni[P(OPh)_3]_4$ were received as fine red-brown and white powders, respectively. Specific parameters for individual NMR experiments are provided as needed in Chapter 3, and can be found with the associated spectra.

SSNMR studies were performed with these three compounds at 21.1, 11.7, 9.4, and 4.7 T at the University of Ottawa and the National Ultrahigh-field NMR Facility for Solids, using the

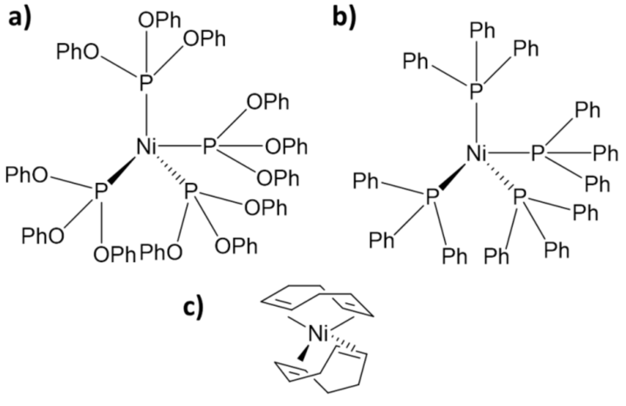

Figure 23: The three Ni(0) compounds studied in this work: a) Ni[P(OPh)$_3$]$_4$; b) Ni(PPh$_3$)$_4$; and c) Ni(cod)$_2$.

probes outlined in Table 4. The first lot of $Ni(cod)_2$ was not ground, as is typical for SSNMR to break up larger crystallites, given the chemical sensitivity of the material. Spectra were collected for stationary samples packed under inert atmosphere in 7 mm o.d. borosilicate cells. Borosilicate cells were used due to the proximity of ^{91}Zr resonances (see Table 2 for the frequency factor, compared to the frequency factor for nickel), but ultimately after some tests no interference from the rotor was observed. However, the borosilicate cells were still advantageous in that they allowed for visual inspection of sample integrity over time. ^{61}Ni MAS SSNMR spectra were acquired for $Ni(PPh_3)_4$ and $Ni[P(OPh)_3]_4$ by spinning at 8 kHz in high-speed (reduced-volume) 7 mm o.d. zirconia rotors, which decreased the sample volume considerably but increased the safe operational spinning speed by 60%. ^{31}P MAS NMR spectra were acquired for the phenylphosphine and phenylphosphite compounds in standard 7 mm o.d. zirconia rotors at 4.7 T and standard 2.5 mm o.d. zirconia rotors at 21.1 T. ^{61}Ni MAS NMR spectra for $Ni(cod)_2$ were acquired for the yellow lot by spinning at 18 kHz in a 4 mm o.d. reduced-volume zirconia rotor. ^{61}Ni QCPMG experiments were attempted for all three compounds given a lack of initial information about the linewidths and chemical shifts; except for $Ni(cod)_2$, too few spikelets were obtained to produce a line shape, although the experiment helped identify the chemical shift (particularly for $Ni(PPh_3)_4$, which had no chemical shift reported in solution). For the $Ni(cod)_2$ QCPMG experiments performed at 21.1 T, ^{1}H decoupling was employed and found to slightly decrease the decay rate of the echo train, improving signal acquisition (a process noted by Schurko in his discussion of ultra-wideline NMR spectrum acquistion[17]). The QCPMG experiment with $Ni(cod)_2$ at 9.4 T did not employ ^{1}H decoupling. Quadrupolar echo spectra likewise did not employ ^{1}H decoupling, and were acquired for all compounds in the solid state at 21.1 T, and for the olive-grey lot of $Ni(cod)_2$ at 11.7 T.

Table 4: Probe information for the experiments and magnetic fields used in this work.

Field	Compound	Phase	Nuclide	Probe
21.1 T	Ni(cod)$_2$	Solid	^{61}Ni	7 mm H/X low-gamma custom static probe
				4 mm H/X Bruker MAS probe
		Solid/ Solution		7 mm X low-gamma custom static probe
	Ni(PPh$_3$)$_4$	Solid		7 mm X low-gamma custom static probe
				7 mm X low-gamma custom MAS probe
	Ni[P(OPh)$_3$]$_4$			7 mm X low-gamma custom static probe
				7 mm X low-gamma custom MAS probe
			^{31}P	2.5 mm H/X Bruker MAS probe
		Solution	^{61}Ni	7 mm X low-gamma custom static probe
14.1 T	Ni(PPh$_3$)$_4$	Solution	^{13}C	5 mm H/C/N liquids autotuning cryoprobe
	Ni[P(OPh)$_3$]$_4$			
11.7 T	Ni(cod)$_2$	Solid	^{61}Ni	7 mm X Bruker static solids probe with custom coil
9.4 T	Ni(cod)$_2$	Solid/ Solution	^{61}Ni	7 mm H/X Bruker static solids probe
7.0 T	Ni(PPh$_3$)$_4$	Solution	^{31}P	5 mm H/X liquids autotuning broadband (BBOF) probe
			^{13}C	
	Ni[P(OPh)$_3$]$_4$		^{31}P	
			^{13}C	
4.7 T	Ni(PPh$_3$)$_4$	Solid	^{31}P	7 mm H/X/Y Bruker MAS probe

Solution NMR spectra were acquired for samples dissolved in deuterated solvents in borosilicate tubes under inert atmosphere. The deuterated solvents were degassed using the freeze-pump-thaw method before drying under inert atmosphere. Benzene-d6 and acetonitrile-d3 were dried using molecular sieves, and ^{1}H NMR integration suggested water content was below 30 ppm for the former and 50 ppm for the latter. Ni(PPh$_3$)$_4$ and Ni[P(OPh)$_3$]$_4$ samples were observed to be relatively insensitive to water content (doping with D$_2$O did not appear to increase the rate of decomposition appreciably). Drying of acetone-d6 (which is incompatible with molecular sieves), was thus milder and involved use of sodium sulfate. ^{1}H NMR integration suggested water content below 300 ppm for this solvent. All compounds studied were observed to be highly sensitive to oxygen. Solution samples were saturated mixtures in 5 mm borosilicate NMR tubes except in the case of solution ^{61}Ni NMR, which involved use of L-shaped 7 mm o.d. tubes custom made for use in a solenoid coil (similar to the cell of Behringer and Blümel[62]). Solution NMR experiments were performed at 21.1, 14.1, and 7.0 T at the University of Ottawa and the National Ultrahigh-field NMR Facility for Solids, with probes used again provided in Table 4.

All spectra were externally referenced. For ^{31}P SSNMR, spectra were calibrated with secondary references. Triphenylphosphine (at -6 ppm) was used for experiments at 4.7 T, while ammonium dihydrogen phosphate (ADP, at 0.81 ppm) was used for 21.1 T experiments. ^{31}P solution NMR spectra were referenced relative to 85% H_3PO_4 (the primary reference at 0 ppm for ^{31}P). ^{13}C and ^{1}H NMR spectra were referenced relative to tetramethylsilane (TMS) in $CDCl_3$. As the IUPAC primary chemical shift reference for ^{61}Ni NMR, $Ni(CO)_4$, is an extremely toxic and volatile liquid, and given the lack of a readily available secondary chemical shift reference, ^{61}Ni NMR spectra were calibrated using the IUPAC unified scale convention; that is, the absolute ^{61}Ni frequency of $Ni(CO)_4$ was calculated from the experimentally determined absolute ^{1}H frequency of 0.1% TMS in $CDCl_3$ according to:[19]

$$\Xi_x = \left(\frac{\nu_x}{\nu_{\text{TMS}}}\right) \times 100\% \tag{2-89}$$

where ν_x is the absolute frequency for the 0 ppm position in the NMR spectrum for nuclide x, ν_{TMS} is the absolute ^{1}H frequency of TMS, and Ξ_x is the frequency factor (found in Table 1 and Table 2). Where ^{1}H tuning was impractical (i.e. for probes where tuning to proton was difficult or impossible at a given field, often due to the lack of a dedicated ^{1}H channel), $^{35/37}$Cl resonances of NaCl in the solid state or as a dilute solution were used to calculate the theoretical absolute frequency of TMS, and then back-calculate the ^{61}Ni absolute reference frequency. Chlorine-based calibration of the chemical shift scale was previously done by Bastow et al. for their work with ^{61}Ni intermetallics in the solid state[68]. However, while this method was sufficient for SSNMR spectra, some discrepancies in chemical shifts for high-resolution solution ^{61}Ni NMR recommended the use of direct ^{1}H or ^{61}Ni calibration for these spectra. Fortunately, the saturated solution of Ni(cod)$_2$ in benzene-d6 produced an intense and narrow ^{61}Ni NMR signal which could be acquired in reasonable timeframes (20 min at 9.4 T and under 5 min at 21.1 T). The ^{61}Ni chemical shift of this signal was referenced to the absolute proton frequency of TMS at 9.4 T, and studied as a function of temperature. Temperatures were calibrated using the proton resonances of neat ethylene glycol according to:

$$T(\mathrm{K}) = 466.5 - 102.00\,\Delta\delta \qquad 273 < T < 416\ \mathrm{K} \qquad [2\text{-}90]$$

where $\Delta\delta$ is the separation in ppm between the two proton signals of ethylene glycol. Ni(cod)$_2$ was then used to check previous ^{61}Ni chemical shift referencing versus ^{1}H and $^{35/37}$Cl at 21.1 T (given the extremely low field drift); the ^{61}Ni(cod)$_2$ and ^{1}H referencing was found to be equivalent within errors associated with peak widths, and chlorine-referenced chemical shifts were updated as required.

$\pi/2$ pulses for ^{61}Ni NMR were calibrated using chlorine-35/37 NMR spectra as both chlorine nuclides are spin-3/2 with gyromagnetic ratios similar to that of ^{61}Ni (Table 2). Given the cubic symmetry of solid NaCl, and quadrupolar averaging in solution, all $\pi/2$ pulses for ^{61}Ni SSNMR were taken as half of the optimized chlorine pulse length to ensure a CT-selective pulse (as discussed in Section 2.1.1.4) and to maximize excitation bandwidth (shorter pulses produce less discriminate excitation). ^{61}Ni SSNMR peak shapes were optimized by moving the transmitter/receiver offset (to ensure the complete line shape was acquired) and by varying relaxation delays (typical values used ranged from 0.5 to 2 s given the efficient relaxation of ^{61}Ni, with 0.5 s giving a reproducible line shape at the shortest repetition time).

Table 5: Optimized bond lengths for nickel compounds as computed in this work compared to previous computational and experimental literature values. Atom indices are as in ref. 64. Bond lengths are averaged for each bond in the molecule corresponding to the listed bond class.

Compound	Bond	Bond length [Å]		
		ZORA-DFT	DFT[a]	Exp.
$Ni(CO)_4$	Ni-C	1.817	1.829	1.825(2)[b]
$Ni(C_2H_4)_2$ (PMe)	Ni-C1	1.997	2.008	2.000(2)[c]
	Ni-C2	2.000	2.011	2.015(2)[c]
	Ni-P	2.159	2.177	2.238(1)[c]
	C1=C2	1.406	1.412	1.383[c]
$Ni(cod)_2$	Ni-C1	2.114	2.121	2.124(9)[d]
	Ni-C2	2.125	2.140	2.124(9)[d]
	C1=C2	1.395	1.401	1.391(2)[d]
$Ni(PF_3)_4$	Ni-P	2.103	2.107	2.099(3)[e]
$Ni(PMe_3)_4$	Ni-P	2.160	2.180	
$Ni(PCl_3)_4$	Ni-P	2.148	2.154	
$Ni(PPh_3)_4$	Ni-P	2.298		
$Ni[P(OPh)_3]_4$	Ni-P	2.148		
$Ni(PPh_3)_3$	Ni-P	2.162		2.139(1)-2.156(1)[f]

[a] From [64]
[b] From [92]
[c] From [93]
[d] From [94]
[e] From [95]
[f] From [96]

2.3.2 Computations

Spin-orbit ZORA DFT computations were performed for a series of nickel compounds by way of the Amsterdam Density Functional[85,97,98] (ADF) computational chemistry program, running on a cluster accessible through the High Performance Computing Virtual Laboratory (HPCVL), a consortium of eight Canadian institutions and member of the national Compute Canada platform. Compounds modeled included the three studied here experimentally by NMR ($Ni(cod)_2$, $Ni(PPh_3)_4$, $Ni[P(OPh)_3]_4$) as well as compounds modeled previously by Bühl et al.[64] ($Ni(PMe_3)_4$, $Ni(PF_3)_4$, $Ni(PCl_3)_4$, $Ni(C_2H_4)_2(PMe_3)$). $Ni(PPh_3)_3$ and $Ni[P(OMe_3)]_4$ were also modeled. All atoms were treated using the same basis set and functional for any given calculation. The present work expands on the previous literature study on ^{61}Ni by including relativistic effects and results for a wider range of NMR parameters, including but not limited to ^{61}Ni-^{31}P J couplings and a broader characterization of the EFG tensor). Given that crystal structures for $Ni(PPh_3)_4$ and $Ni[P(OPh)_3]_4$ could not be found in the literature, geometries for all compounds except $Ni(cod)_2$ were generated by using GaussView[99] to produce an initial structure, followed by a TZP (triple zeta with one polarization function) basis/BP86 functional ZORA DFT optimization computation. The functional is a Generalized Gradient Approximation (GGA) functional (i.e. it includes calculation of electron density gradients, see Section 2.2.1.2) using an exchange term from Becke[100] and correlation term from Perdew[101], and was selected both to maintain consistency with the previous study by Bühl et al. and because it was deemed sufficient for a structural optimization (indeed, given the time required to optimize $Ni(PPh_3)_4$ and $Ni[P(OPh)_3]_4$, a hybrid functional would likely have been impractical for this purpose). Crystal structure atomic coordinates[94] were used to generate the structure of $Ni(cod)_2$, followed by a similar optimization scheme. Optimized geometries were assessed by comparing selected bond lengths to published experimental and computational results (Table 5).

Following the previously discussed recommendation by Bühl et al., NMR computations were performed using a B3LYP (hybrid) functional, first described by Becke[102,103]. Results were computed twice where possible, once with a TZP basis and once with a QZ4P (quadruple zeta with four polarization functions) basis. The TZP basis produced results for all compounds and is therefore the default for values presented for this work; QZ4P results will be included for comparison and clearly identified. Magnetic shieldings were converted to chemical shifts by using (i) direct calibration relative to $Ni(CO)_4$ (i.e. using the calculated magnetic shielding of

$Ni(CO)_4$ as the reference shielding, σ_{ref} in [1-6]), and (ii) by using the regression method demonstrated by Bühl et al. and described previously in this work (see Figure 22). Specifically, in the latter method chemical shifts were extrapolated from fitting the computed magnetic shielding values against previously reported solution chemical shifts (with the exception of $Ni(CO)_4$ itself).

GIPAW DFT computations were performed for $Ni(cod)_2$ in order to gain perspective on the effects of crystal structure on the NMR parameters determined for the gas-phase ZORA DFT computations, using the Cambridge Serial Total Energy Package (CASTEP)[87,104–106] program running on the private Wooki cluster with the permission of the Woo lab at the University of Ottawa. The NMR computation was performed using a PBE[107] (Perdew, Burke, Ernzerhof) GGA functional with an ultra-fine precision (5.0×10^{-7} eV/atom SCF tolerance, 0.04 Å^{-1} *k*-points separation, 390 eV energy cutoff) on the literature crystal structure[94] of $Ni(cod)_2$.

3 RESULTS AND DISCUSSION

3.1 NMR Spectroscopy

3.1.1 Bis(1,5-cyclooctadiene)nickel(0)

First, the results for the yellow lot of Ni(cod)$_2$ will be presented (i.e. in reverse chronological order), as there was some concern that the olive-grey lot of Ni(cod)$_2$ used was contaminated or otherwise impure. Figure 24 is a static ^{61}Ni SSNMR spectrum for solid Ni(cod)$_2$ which made use of a quadrupolar echo experiment at 21.1 T and a QCPMG sequence at both 21.1 and 9.4 T. Figure 25 demonstrates a ^{61}Ni rotor-synchronized-echo MAS SSNMR experimental spectrum at an 18 kHz spinning speed. Iterative fitting[108] of all spectra was used to extract a set of NMR parameters consistent with all line shapes acquired; the results are summarized in Table 6. The experimental δ_{iso} of 965 ± 10 ppm is slightly greater than the solution value reported previously for this compound[20] and measured in this work (δ_{iso} = 937 ppm), but is reasonable given the difference in state (for example, similar differences between solution and the solid state can be seen for Ni[P(OPh)$_3$]$_4$). The span (Ω) of 1700 ± 50 ppm (compared to the ZORA DFT value of 1306 ppm (TZP) and 1428 ppm (QZ4P)) suggests that for this compound the static line shape is dominated by the CSA, despite the not-insignificant quadrupolar coupling constant (C_Q = 2.0 ± 0.3 MHz). With regards to the computationally determined parameters, the experimental C_Q is smaller than both the value determined here (4.06 MHz for TZP, 3.93 MHz for QZ4P) and by Bühl et al. (2.60 MHz)[64]. The experimental

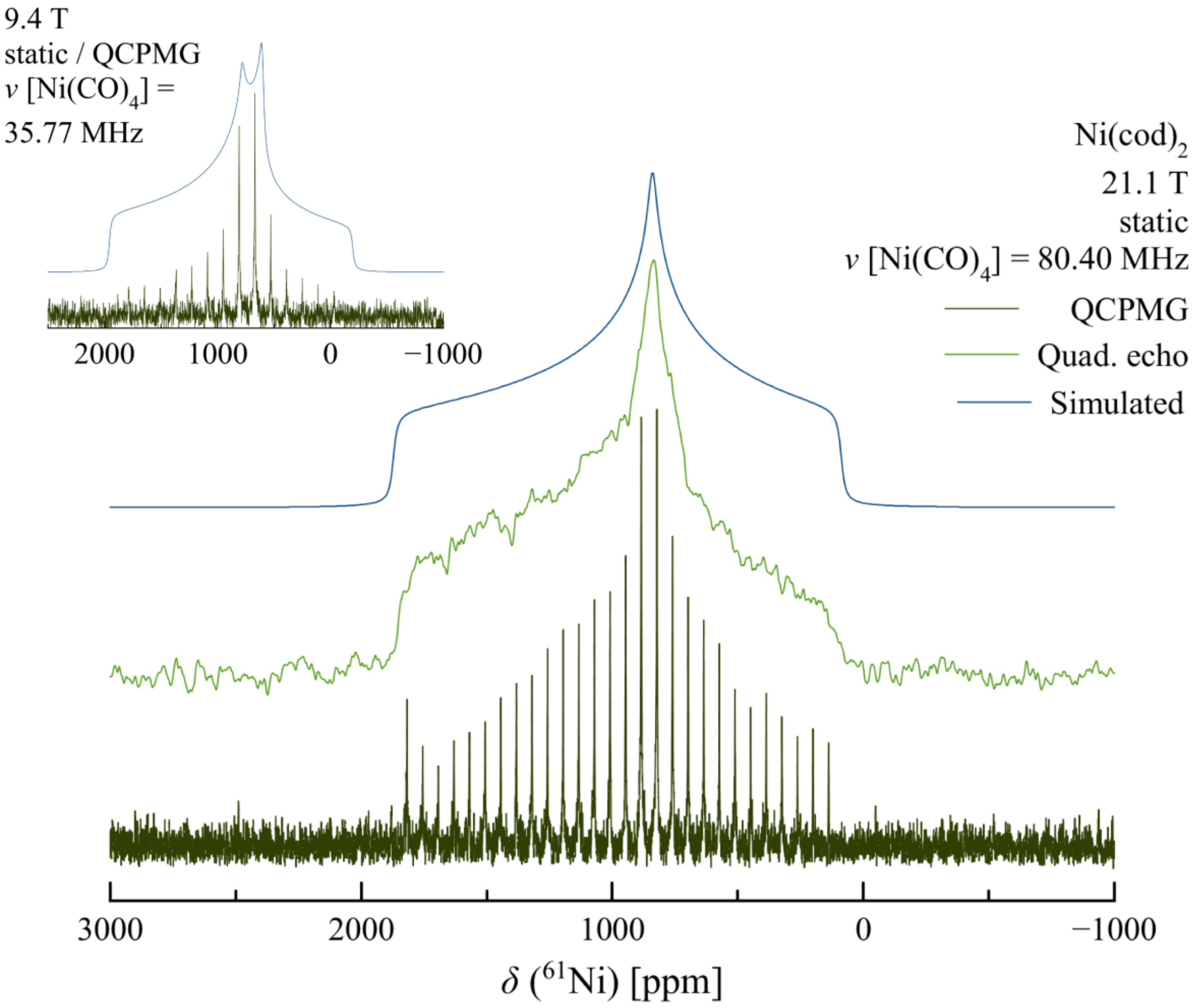

Figure 24: Experimental and simulated ^{61}Ni NMR spectra of static Ni(cod)$_2$ (yellow lot) at $\nu(^1H)$ = 900 MHz. Fit parameters (Table 6) were determined by iterative fitting at multiple fields. For both experiments shown, equal numbers of transients were acquired at offsets of 0, +80, and +160 kHz relative to 0 ppm, and the spectra summed to give the total line shape. A recycle delay of 0.5 s was used for both experiments. For the QCPMG experiment, 36k scans were acquired at each offset over a total of 17 h with a spikelet separation of 5 kHz. Proton decoupling slightly increased the length of the echo train. For the echo experiment a modified quadrupolar echo was used without proton decoupling. Specifically, the second pulse was decreased from a π to a $\pi/2$ pulse to maximize effective excitation bandwidth, resulting in a $\pi/2$-τ-$\pi/2$ quadrupolar echo. For the echo, 152k scans were acquired at each offset with a 70 µs echo time for a total experiment time of 66 h. The inset shows experimental and simulated ^{61}Ni NMR spectra of static Ni(cod)$_2$ at $\nu(^1H)$ = 400 MHz. Equal numbers of transients were acquired at offsets of 0, +36, and +66 kHz relative to 0 ppm, and the spectra summed to give the total line shape. 132k scans were acquired at each offset over a total of 60 h with a spikelet separation of 5 kHz.

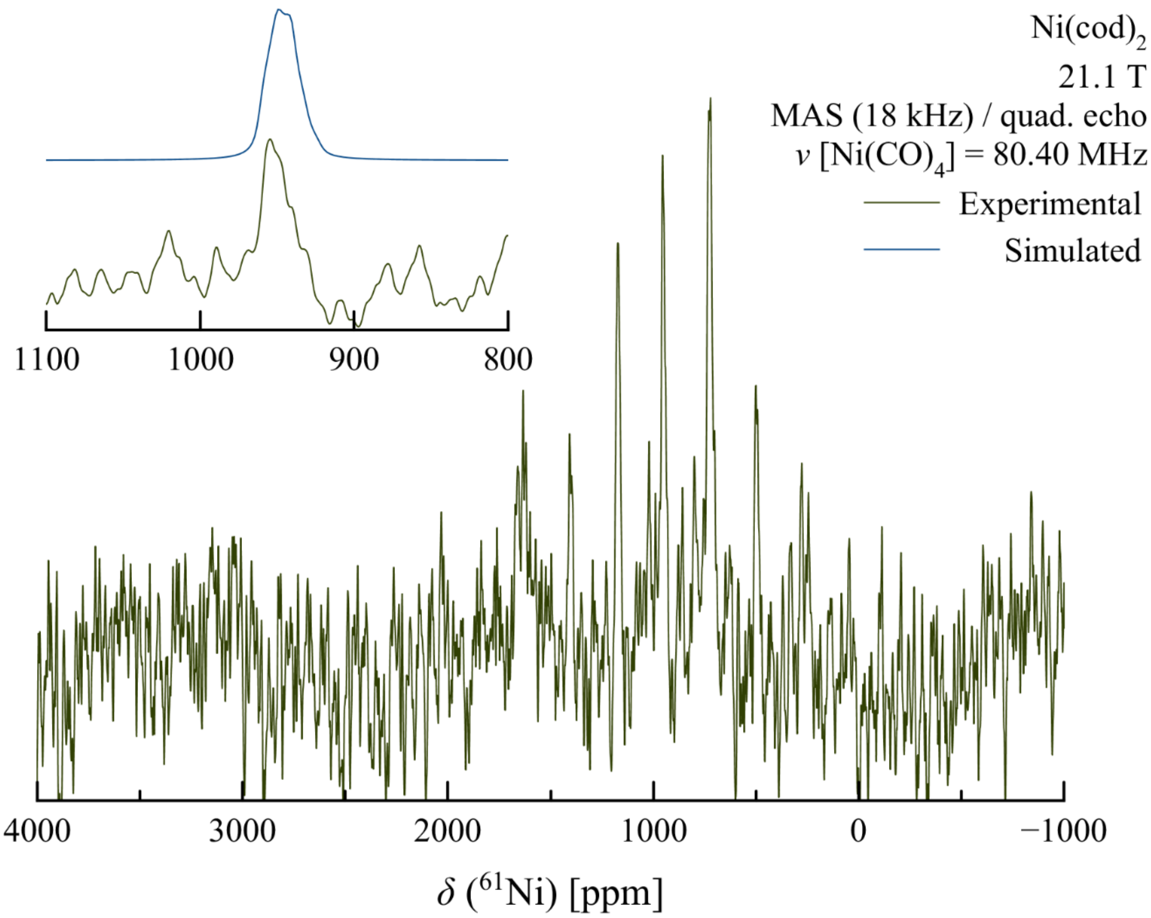

Figure 25: Experimental ^{61}Ni MAS NMR spectrum of Ni(cod)$_2$ (yellow lot) at $\nu(^1H) = 900$ MHz, with the isotropic peak and a quadrupolar parameter simulation in the inset. A rotor-synchronized $\pi/2$-τ-$\pi/2$ modified quadrupolar echo was used to acquire the spectrum at an 18 kHz spinning speed. Though this necessitated use of a reduced-volume 4 mm o.d. rotor, significantly reducing the amount of available sample in the coil, the 161 kHz static spectrum linewidth suggested that slower spinning speeds would not be able to effectively average the anisotropic interactions present. 655k transients were acquired over 93 h with a recycle delay of 0.5 s.

quadrupolar asymmetry parameter of $\eta = (0.5 \pm 0.2)$ is intermediate to the TZP computational value found here ($\eta = 0.36$) and the results of Bühl et al.($\eta = 0.87$), as well as the ZORA QZ4P value calculated in this work ($\eta = 0.90$). That the experimental C_Q for Ni(cod)$_2$ is within the range estimated for Ni[P(OPh)$_3$]$_4$ (discussed later) suggests that despite the co-ordination of the nickel center only by π-bonds, the structure is indeed highly symmetric. This may be related to the rigid nature of Ni-C alkene bonds, mentioned in Section 1.3.1.

As seen in Figure 26, for a static echo experiment at 11.7 T, and Figure 27, the ^{61}Ni static SSNMR for the olive-grey lot of Ni(cod)$_2$, despite being performed under otherwise identical experimental conditions at 21.1 T, gave distorted line shapes compared to the yellow lot. Namely, this sample produced significantly decreased intensity on the low-frequency edge of the CT powder pattern, which could not be fit by simulation. Two theories are presented as an explanation for this phenomenon. First, it may be that the distortion stemmed from an orientational preference in the sample as it was not ground prior to study. The lack of homogenization would require that sample be treated as a discrete number of crystallites, rather than an infinite collection of randomly oriented particles (which is presumed by theoretical treatments of powder SSNMR). Practically speaking, this means that rather than obtaining a truly random distribution of crystallite orientations there could be a preference for a certain range of orientations in the sample due to the stacking of larger crystallites disproportionately along certain directions. This would influence the effective anisotropic interactions observed for the bulk sample and cause distortions which cannot be accounted for by any single set of parameters for the overall spectrum. This effect has previously been observed in ^{35}Cl SSNMR spectra of MgCl$_2$, which form platelets that can stack in the solid state under the pressure resulting from packing the sample into a rotor.[109] Another possibility could be introduction of inhomogeneous broadening [2-12]. $Ni(cod)_2$ decomposes into nickel metal with time, which could result in spectral artifacts: the application of an oscillating magnetic field to a metal will produce a current that opposes the applied magnetic field (according to Lenz's law, a corollary to Faraday's law of induction). This in turn causes some of the applied magnetic pulse to be wasted, decreasing the signal measured by the NMR spectrometer. This does not, however, explain why one side of the spectrum is preferentially affected – the spatial dependence may arise from the slow penetration of oxygen into the sample with time, which would cause decomposition to progress from the capped end of the tube to the bottom. Indeed, this explanation would also account for why the tailing effect seen for the olive-grey sample can also be seen to a degree on the right-hand side of the echo experiment performed with the yellow lot. The echo experiment with the yellow lot was accompanied by some sample discolouration, with material closer to the opening of the borosilicate cell acquiring a tan hue relative to the original yellow state by the end of the experiment. The echo experiment was performed over a much longer time period than the QCPMG experiment (60 h and 17 h, respectively), however, and the magnitude of the spectral change is much smaller for the yellow sample. As a result, it is difficult to state definitively whether one, both, or neither of these proposals are the cause of this artifact. Nevertheless, between the use of multiple fields and the inclusion of MAS results, one can be confident in the fit obtained for the yellow $Ni(cod)_2$ material.

The fit for this compound assumes a single crystallographic site in the unit cell of solid $Ni(cod)_2$, as determined in a literature single-crystal X-ray diffraction study.[94] The presence of only a single crystallographic site helps to justify the use of gas-phase calculations to assess the spectral fit, and as the data in Table 5 demonstrate, the experimental solid- and computed gas-phase structures have similar characteristic bond lengths (Ni-C1 length of 2.114 Å and Ni-C2

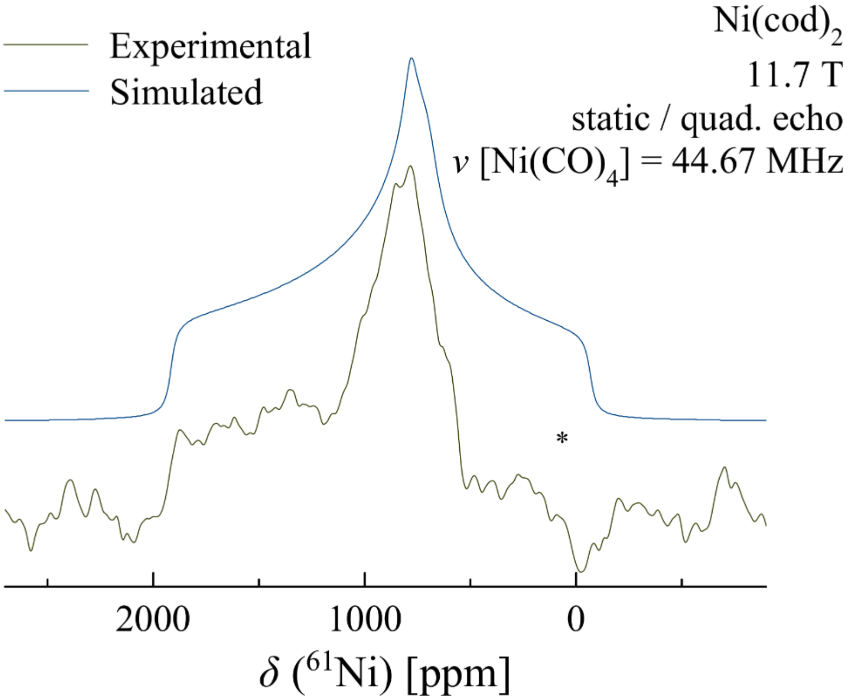

Figure 26: Experimental and simulated ^{61}Ni NMR spectra of static Ni(cod)$_2$ (olive-grey lot) at ν(^{1}H) = 500 MHz. '*' denotes a region of decreased intensity ascribed to preferential orientation of crystallites in the sample. The linewidth of approximately 2500 ppm corresponds to 112 kHz; the effects of pulse excitation width were determined by sampling at variable offsets and were not found to be the source of the artifact. For reasons of technical limitation a QCPMG experiment was not attempted at this field. 160k scans were acquired over 3 days using a $\pi/2$-τ-$\pi/2$ echo with an echo time of 76 μs and recycle delay of 0.5 s.

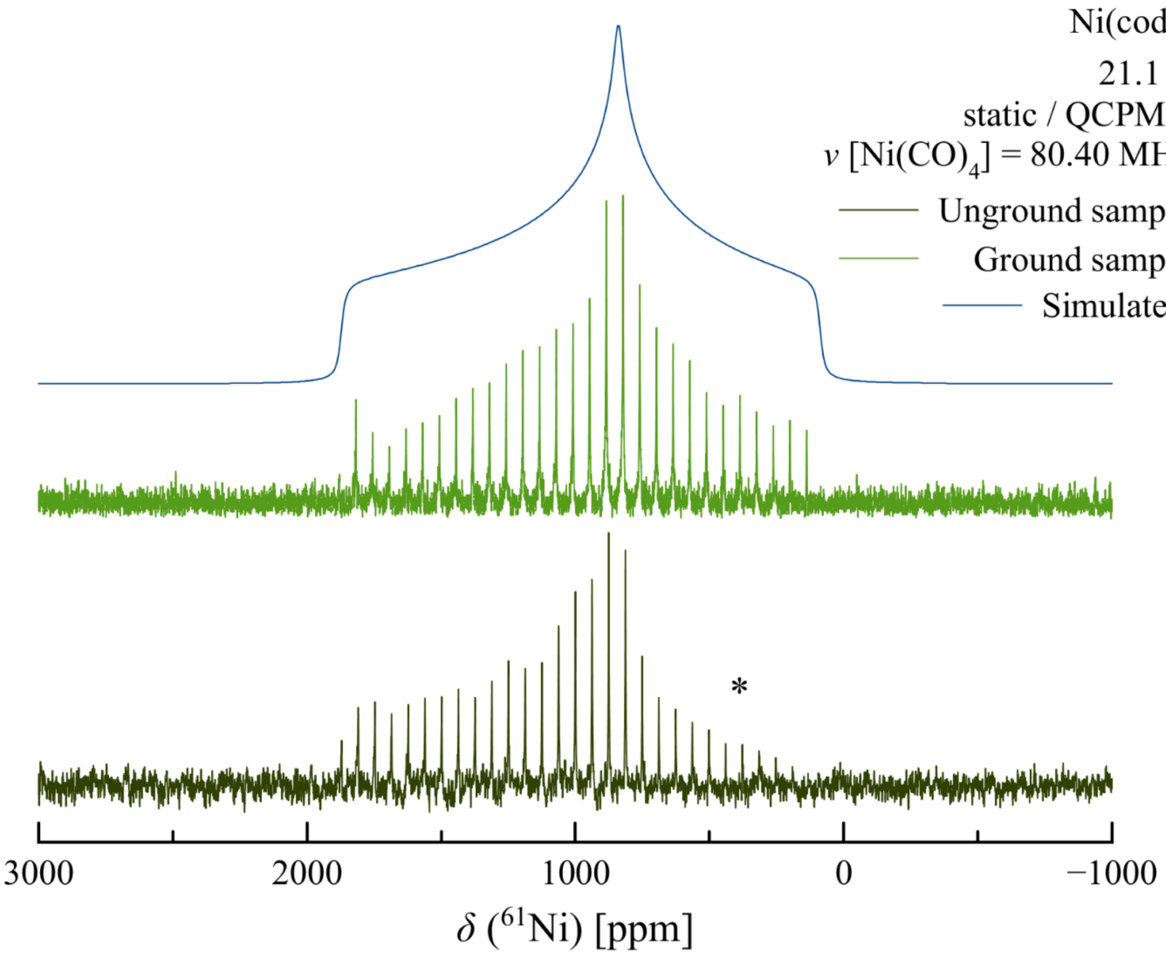

Figure 27: Experimental and simulated ^{61}Ni NMR spectra of static Ni(cod)$_2$ at ν(^{1}H) = 900 MHz. '*' denotes a region of decreased intensity ascribed to preferential orientation of crystallites in the original sample tested, which consisted of platelets of olive-grey material and was not ground due to chemical sensitivity issues with the compound. The experimental details of the ground sample spectrum are provided in Figure 24. For the unground sample, 88k scans were acquired over 20 h with a recycle delay of 0.5 s and a spikelet separation of 5 kHz. Proton decoupling slightly increased the length of the echo train.

length of 2.125 Å from ZORA DFT in this work; 2.121 Å and 2.140 Å respectively for the DFT results from Bühl et al.[64], and 2.124(9) Å for both bonds from the experimental crystal structure[94]).

Lastly, the purity of the yellow compound could be verified using solution NMR spectroscopy. The ^{1}H NMR chemical shifts (^{1}H NMR: δ 4.28 (br, =CH), δ 2.05 (br, CH_2)) are consistent with the literature[91], as is the ^{61}Ni chemical shift (δ_{iso} = 936.5 ppm compared to the literature 937 ppm[20]). Solution ^{13}C NMR also indicates the presence of the pure compound, with the cyclooctadiene ligands observed (^{13}C NMR: δ 89.30 (=CH), δ 30.49 (CH_2)).

Beyond its usefulness in assessing the chemical identity of the yellow $Ni(cod)_2$ material, the relative ease of ^{61}Ni NMR in solution with this compound is promising for its use as a secondary chemical shift reference and as a means for pulse calibration, particularly at high fields. The narrow linewidth ($\nu_{1/2}$ of ~50 Hz at 9.4 T and ~100 Hz at 21.1 T) enables acquisition of good signal-to-noise spectra in reasonable time periods with a high degree of precision in the isotropic chemical shift. A ^{61}Ni NMR nutation curve acquired using this sample produced results similar to those of $^{35/37}$Cl NaCl in solid or solution, increasing confidence in the use of chlorine to calibrate ^{61}Ni NMR pulse lengths. The chemical shift was observed to be strongly and linearly temperature dependent; a plot is provided in Figure 28 with the final equation of the fit being:

$$\delta_{\text{iso}}(\text{Ni(cod)}_2, {}^{61}\text{Ni}) = (0.4274 \pm 0.0063)T + (810.3 \pm 1.9) \qquad [3\text{-}1]$$

Based on this equation, the ^{61}Ni chemical shift at 295 K is 936.5 ± 2.7 ppm, with the error relative to the IUPAC and $Ni(CO)_4$ referencing methods, and taking into account the temperature dependence of the chemical shift.

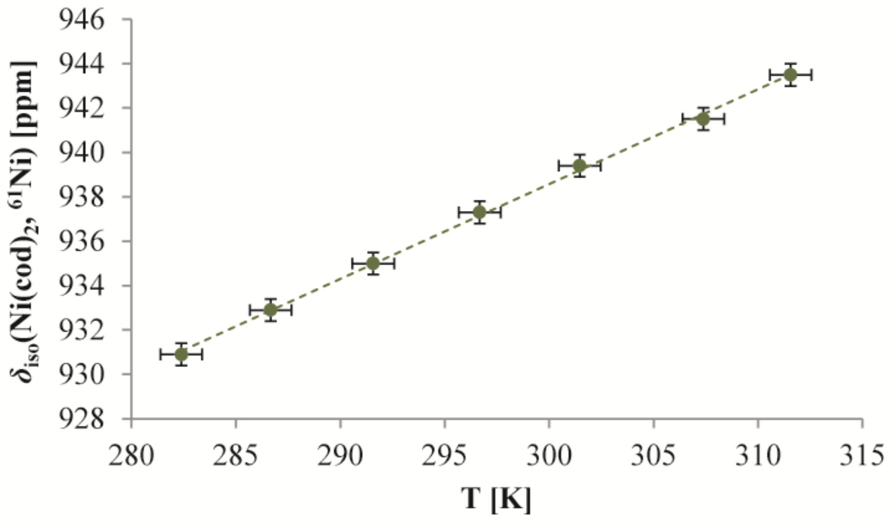

Figure 28: Temperature calibration of the ^{61}Ni δ_{iso} value of Ni(cod)$_2$ saturated in C_6D_6. The equation of the line of best fit is $\delta_{iso} = (0.4274 \pm 0.0063)T + (810.3 \pm 1.9)$, with $R^2 = 0.999$.

3.1.2 Tetrakis(triphenylphosphite)nickel(0)

Experimental solid-state ^{61}Ni NMR spectra of Ni[P(OPh)$_3$]$_4$ are provided in Figure 29 (both static and MAS at 8 kHz). In the case of Ni[P(OPh)$_3$]$_4$, only limited line shape fitting could be performed because of overlap between multiple sites, with two sites clearly resolved under MAS yielding relative integrations of 1.0 and 2.1. While keeping in mind that the integrations are approximate given the relatively low signal-to-noise, in the absence of impurities this would suggest the presence of multiple crystallographic sites. This is further supported by an inability to fit the MAS NMR line shapes adequately with anything but a two-site model. Upper bounds of C_Q and ranges for δ_{iso}, as determined by MAS NMR, are included in Table 6. For both sites, the C_Q was estimated to be less than 3.5 MHz using a two-site fitting and variable line broadening, while the δ_{iso} values could only be given as a range (δ_{iso} = -500 to -550 for one site, -590 to -635 for the other) as the fitted isotropic chemical shift varies with the second order quadrupolar shift. The static spectrum could not be fit due to a lack of crystallographic information which, coupled with uncertainty in the C_Q and δ_{iso} values obtained by ^{61}Ni MAS NMR, resulted in too many unknowns to allow for a reliable fitting.

The solution ^{61}Ni chemical shift for Ni[P(OPh)$_3$]$_4$ has been reported previously,[20] but here it is possible to also provide the ^{61}Ni-^{31}P *J* coupling seen for other nickel-phosphorus bond-containing species in literature (Figure 30). There is a difference of about 10 ppm in reported δ_{iso} values (with -587 ppm measured here and -576 ppm reported in literature[20]), but given the solvent sensitivity of ^{61}Ni isotropic chemical shifts,[64] and the lack of a solvent reported with the literature chemical shift,[20] the discrepancy is not especially concerning. In Figure 30, the central three peaks of the expected pentet fine structure can be clearly observed, with the

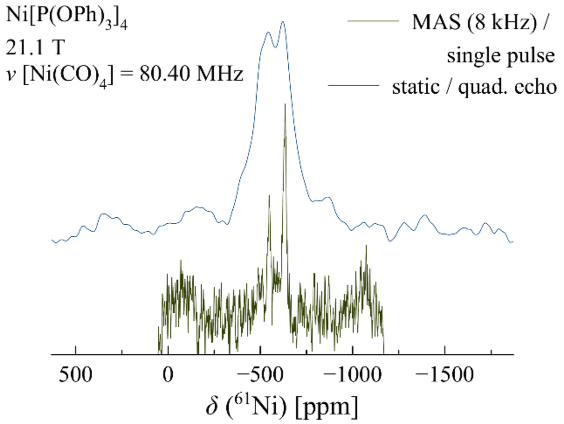

Figure 29: Experimental ^{61}Ni NMR spectra of Ni[P(OPh)$_3$]$_4$ at $\nu(^1H)$ = 900 MHz under static and MAS conditions. Under sample spinning the broad static spectrum narrows to two sites with integration of 2.1 to 1.0. Given that only one site appears in solution (Figure 30) this would appear to stem from multiple crystallographic sites rather than multiple species. For static at high field, 174k scans were acquired over 20 h using a $\pi/2$-τ-π quadrupolar echo with an echo time of 70 μs and recycle delay of 0.5 s. For MAS NMR, 436k scans were acquired over 3 days with a recycle delay of 0.5 s at an 8 kHz spinning speed.

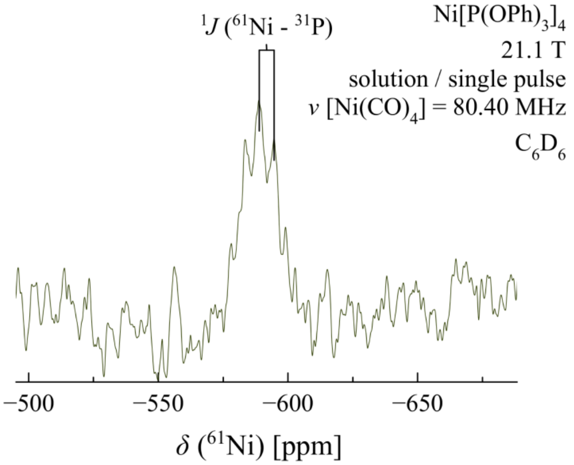

Figure 30: Experimental ^{61}Ni NMR spectrum of Ni[P(OPh)$_3$]$_4$ in benzene-d6 at $\nu(^1H)$ = 900 MHz. Note the presence of the expected nickel-phosphorus pentet (the central three peaks being clearly defined), with $^1J(^{61}Ni$-$^{31}P)$ = 400 ± 20 Hz, similar to what has been observed for related species (specifically 398 Hz for Ni[P(OMe)$_3$]$_4$)[4]. 66k scans were acquired over 10 h with a recycle delay of 0.5 s.

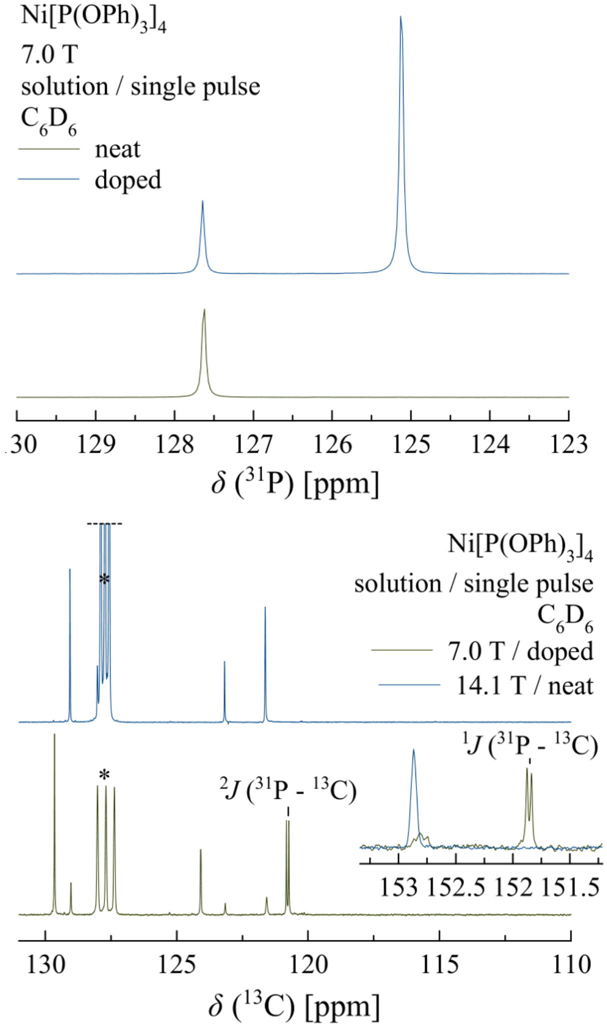

Figure 31: ^{31}P (top) and ^{13}C (bottom) solution NMR spectra of Ni[P(OPh)$_3$]$_4$ in benzene-d6 with the doped experiments including dissolved triphenylphosphite. Given that only one peak was observed in the ^{31}P NMR solution spectrum for this compound, it is unlikely that multiple chemical species exist in the starting solid. '*' denotes the solvent carbon 1:1:1 triplet.

measured one-bond J coupling value of $^1J(^{61}\text{Ni},^{31}\text{P}) = 400 \pm 20$ Hz within the same range found for the chemically similar $\text{Ni[P(OMe)}_3]_4$ (both experimentally at 398 Hz[59] and computationally at 396 Hz (TZP), although the ZORA QZ4P value of 450 Hz is overestimated), and equivalent within error to the value predicted from ZORA DFT calculations on $\text{Ni[P(OPh)}_3]_4$ itself at the TZP basis level (408 Hz).

Solution NMR experiments provide further evidence that the two signals observed in the solid state are associated with two crystallographically distinct sites rather than multiple chemical species. Doping experiments with triphenylphosphite were able to clearly separate and identify free and bound ligand peaks, with the ^{31}P NMR spectrum in particular demonstrating the presence of only one $\text{Ni[P(OPh)}_3]_4$ chemical environment in the sample upon dissolution of the solid in C_6D_6 (Figure 31). This, combined with the pentet observed in the ^{61}Ni solution NMR spectrum, strongly suggests that the two peaks observed in the solid-state stem from multiple crystallographically inequivalent molecules in the asymmetric unit, rather than from multiple chemical species. In theory, the ^{61}Ni-^{31}P J coupling should be seen in the ^{31}P solution NMR spectrum, but as a result of the quadrupolar nature and extremely low natural abundance of ^{61}Ni, ^{61}Ni-^{31}P satellite couplings are almost always broadened into the baseline (as mentioned previously).[62]

It is worth mentioning that the ^{31}P-^{13}C J coupling observed for the unbound triphenylphosphite cannot be seen in the bound ligand; even accounting for the increased line widths observed for the latter, the J coupling must be significantly smaller in order to not be detected (Figure 31). This likely stems from the effects of electron delocalization from the P-O-C region to the Ni-P-O moiety. In fact, the effects of ligand association in the case of triphenylphosphite have been previously reported. Single substitution from Ni(CO)_4 to

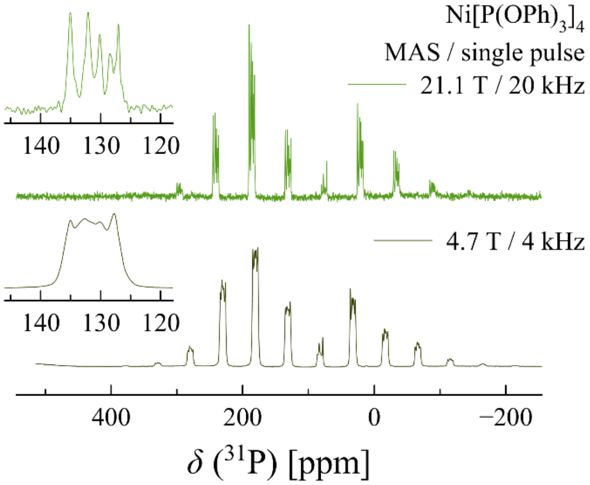

Figure 32: Experimental ^{31}P MAS NMR spectra of Ni[P(OPh)$_3$]$_4$ at 4.7 and 21.1 T. Isotropic peaks are shown in the inset, with all other peaks stemming from spinning sidebands. Isotropic peaks were identified by running at two spinning speeds at each field; the highest-speed spectrum is shown. Deconvolution of the spectra proved impossible, given the homonuclear dipolar coupling and lack of a crystal structure, without which the number of unique phosphorus sites to be modeled is unknown.

$Ni(CO)_3[P(OPh)_3]$ results in *J* coupling values of 2.9 and 5.0 Hz for the one- and two-bond couplings compared to 3.4 and 6.9 Hz in the free ligand,[110] the decrease correlating with a *J* coupling too small to be resolved in the case of fully substituted $Ni[P(OPh)_3]_4$ (though, from the spectra, unambiguously below 2 Hz).

^{31}P MAS NMR spectra for this compound were not helpful with resolving the crystallographic nature of this compound, thanks to the effects of homonuclear dipolar coupling (Figure 32).

3.1.3 *Tetrakis(triphenylphosphine)nickel(0)*

^{61}Ni SSNMR static and MAS spectra collected for $Ni(PPh_3)_4$, shown in Figure 34, reveal a rather narrow (30 kHz central transition linewidth) line shape flanked by two ‘horns’, corresponding to the central ($m = 1/2 \leftrightarrow -1/2$) and satellite ($m = 3/2 \leftrightarrow 1/2$ and $m = -1/2 \leftrightarrow -3/2$) transitions, respectively. Given that the ^{61}Ni chemical shift in solution has not previously been reported for this compound, computational and experimental results for the model $Ni(PMe_3)_4$ and computed values for $Ni(PPh_3)_4$ itself, in addition to the trend found in chemical shifts upon substitution from $Ni(CO)_4$ to $Ni(CO)_3(Ph)$ to $Ni(CO)_2(Ph)_2$,[62] were used to guide the search for the general peak location in the solid state, and in fact match what would be expected (with isotropic chemical shifts of 24.2, 90.7 and 515 ppm for $Ni(CO)_3(Ph)$, $Ni(CO)_2(Ph)_2$, and $Ni(PPh_3)_4$, respectively). The single-pulse ^{61}Ni MAS NMR spectrum acquired for this compound (Figure 34), while not exemplifying the satellite transition spinning sideband manifold that would be expected at 8 kHz (likely due to low signal-to-noise), is still useful in that it does not suggest the signal in the static spectrum originates from multiple crystallographic sites. As is shown in the Figure 35, the static line shape was fit (Table 6) at one field using the satellite transitions, with the quadrupolar coupling constant (C_Q = 0.05 ± 0.01 MHz) of similar magnitude to that computationally predicted for $Ni(PMe_3)_4$ (0.15 MHz). The ZORA DFT computed span of 132 ppm for $Ni(PPh_3)_4$ is similar to the experimental span of 50 ± 50 ppm.

Interestingly, despite giving narrower static solid-state line shapes than either of the other two compounds, $Ni(PPh_3)_4$ gives much weaker NMR signals for each nuclide studied over the same acquisition time. This is likely a result of the chemistry of this compound; $Ni(PPh_3)_4$ has been demonstrated to form an equilibrium with the trigonal planar species and free ligand in solution[111–113]:

$$Ni(PPh_3)_4 \rightleftharpoons Ni(PPh_3)_3 + PPh_3 \tag{3-2}$$

Given that the purity of the compound as provided was only quoted in terms of its nickel content, it is entirely possible and indeed, based on the ^{31}P MAS NMR spectra acquired (Figure 36), likely that the solid used was a mixture of the trigonal planar $Ni(PPh_3)_3$ and the tetrahedral $Ni(PPh_3)_4$. As can be seen from solution ^{31}P NMR, the chemical shift of the tetrahedral signal is observed at lower frequency relative to the trigonal planar $-(PPh_3)_3$ signal (Figure 37). Correspondingly, the number of signals present in the ^{31}P MAS NMR spectra and their chemical shifts would strongly suggest the presence of both these particular chemical species in the solid state as well, accounting for the low ^{61}Ni NMR signal intensity per unit volume compared to the other compounds: there is simply less $Ni(PPh_3)_4$ as a total proportion of the solid (the tricoordinate species being unobservable by ^{61}Ni NMR at present). Further evidence of the presence of $Ni(PPh_3)_3$ is provided by previous UV-vis characterizations which have

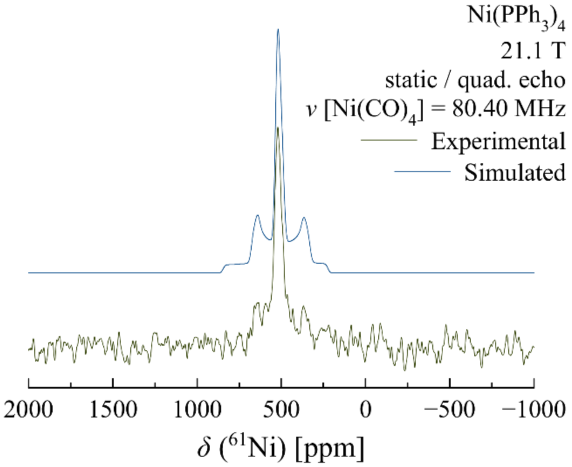

Figure 33: Experimental and simulated ^{61}Ni NMR spectra of static $Ni(PPh_3)_4$ at $v(^1H) =$ 900 MHz. Fit parameters (Table 6) were determined by analysis at one field, using the shape of the satellite transitions as a guide; demonstration of this process is shown in Figure 35. 174k scans were acquired over 20 h using a $\pi/2$-τ-π quadrupolar echo with an echo time of 70 µs and recycle delay of 0.5 s.

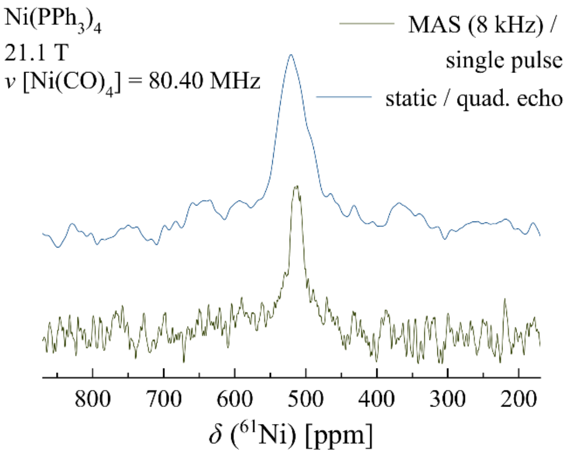

Figure 34: Experimental MAS and static (see Figure 7) ^{61}Ni NMR spectra of $Ni(PPh_3)_4$ at $v(^1H) = 900$ MHz. The single (relatively) narrow peak does not suggest the presence of multiple crystallographically distinct $Ni(PPh_3)_4$ sites in the solid phase. For MAS NMR, 461k scans were acquired over 67 h with a recycle delay of 0.5 s at an 8 kHz spinning speed.

demonstrated that the $Ni(PPh_3)_3$ form is red-orange[111], explaining the overall red-brown and red colours of the solids and solutions respectively. In fact it has been suggested by Tolman et al. that the solid form exists only as $Ni(PPh_3)_3 \cdot PPh_3$, with no presence of the tetra-coordinated species at all.[111] While single-crystal X-ray structures have not previously been obtained for this solid because of crystal disorder,[112] NMR spectroscopy depends only on local order. The ^{31}P MAS NMR spectra may suggest a complicated mixture of products, but alone it is far from conclusive, and it is the ^{61}Ni NMR spectra presented here which provide strong evidence for the existence of the high-symmetry $Ni(PPh_3)_4$ as a discrete complex in the solid state, as opposed to the solid being solely the trigonal planar species with the extra triphenylphosphine ligand incorporated as part of the crystal lattice. Between the ^{31}P MAS and ^{61}Ni static NMR experiments, and the colour of the solid material, it would appear that both of the hypotheses put forward by Tolman et al. regarding the nature of this solid were correct[111]: solid $Ni(PPh_3)_4$ appears to be a mixture of bound ligand and the tetrakis- and tris-coordinated species, with their suggestion of crystal packing forces stabilizing $Ni(PPh_3)_4$ being a likely explanation for the presence of the otherwise unstable complex. This would also explain the difficulty in characterization by X-ray crystallography, specifically explaining the apparent disorder in the crystal.

It is worth noting that while the quadrupolar coupling constant is the predominant indicator of the presence of $Ni(PPh_3)_4$, its value does not necessarily agree with the DFT computations (Table 7). While the experimental C_Q for $Ni(PPh_3)_4$ (0.05 ± 0.01 MHz) is much smaller than that predicted by computation for a model of $Ni(PPh_3)_4$, the C_Q is very close to that predicted for $Ni(PMe_3)_4$ (0.15 MHz at both TZP and QZ4P ZORA DFT levels), and is much too small to be attributable to $Ni(PPh_3)_3$, which should be broadened beyond the

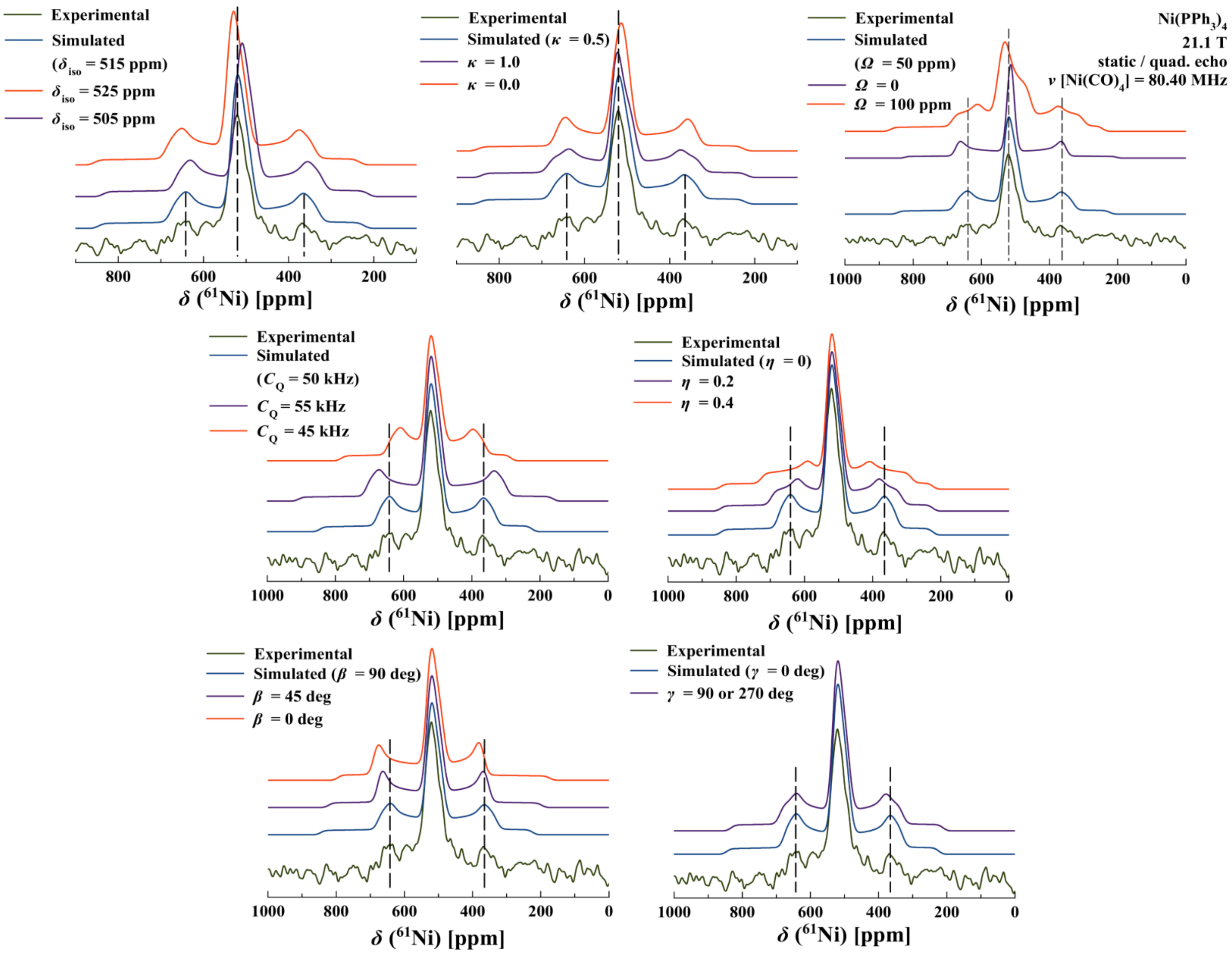

Figure 35: Demonstration of the protocol used to fit the ^{61}Ni static NMR spectrum of Ni(PPh$_3$)$_4$, taking advantage of the information provided by the satellite transitions.

observed spectral window (with a C_Q of around 20 MHz predicted, corresponding to a 640 kHz central transition linewidth at 21.1 T for ^{61}Ni NMR according to [1-30]). The reason why the quadrupolar coupling is overestimated for $Ni(PPh_3)_4$ in the computations is likely due to the fact that the models use gas-phase structures. Given that $Ni(PPh_3)_4$ is unstable outside of the solid state, the gas phase structure is unlikely to be representative. Indeed, the bond lengths predicted by DFT support this suggestion (Table 5). Specifically, the Ni-P bond-length in $Ni(PPh_3)_4$ appears to be significantly longer than for any other related nickel compound modeled, particularly $Ni(PMe_3)_4$ and $Ni(PPh_3)_3$. In fact, while $Ni(PMe_3)_4$, $Ni(PPh_3)_3$, and $Ni[P(OPh)_3]_4$ have essentially identical Ni-P bond lengths (2.160, 2.162, and 2.148 Å respectively), $Ni(PPh_3)_4$ has Ni-P bond lengths of 2.298 Å, about 0.15 Å longer than $Ni[P(OPh)_3]_4$ (keeping in mind that although the geometry optimizations were run only at one level, they are equivalent within the second decimal place to those of Bühl et al.[64]). GaussView[99] plots of pre- and post-optimization models highlight the differences in lowest-energy conformations of the $-(Ph_3)_4$ and $-[(OPh)_3]_4$ pair and are provided in Figure 38. The significance of the computational results, apart from validating the assignment of the experimental spectrum, is that their implications correspond with Tolman's original assertion that steric, rather than electronic effects, can determine homogeneous catalytic structure and function,[111,113] demonstrating the principle for one of the compounds he used in his original investigations into ligand cone angles and explaining the particular instability of $Ni(PPh_3)_4$. Specifically, Tolman and coworkers noted that steric effects explain that PPh_3, with a ligand cone angle of 145°, dissociates readily from a tetra-coordinated nickel center compared to the similar PMe_3 ligand (with a cone angle of 118°), which does not.[111] Indeed, it has been demonstrated (by Tolman) that the Ni-P bond strength in nickel(0) compounds depends primarily on steric effects.[113]

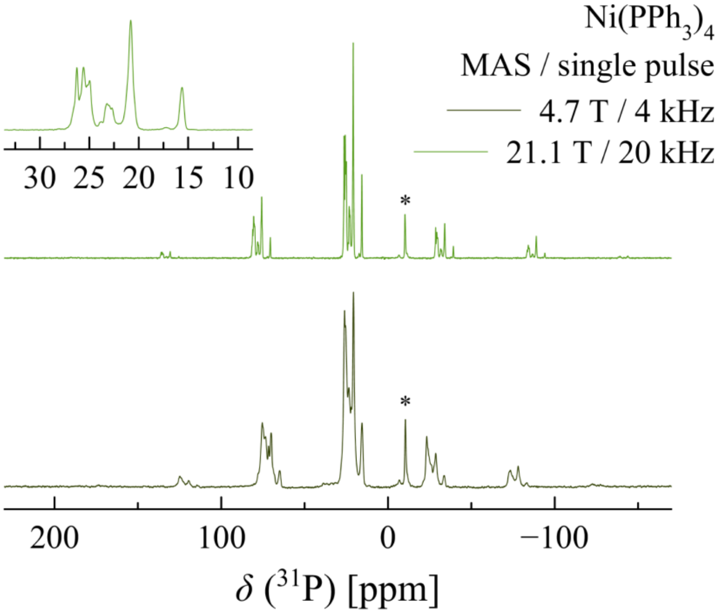

Figure 36: Experimental ^{31}P MAS NMR spectra of Ni(PPh$_3$)$_4$ at 4.7 and 21.1 T. Triphenylphosphine is marked with '*'. The other isotropic peaks are shown in the inset, with all other peaks stemming from spinning sidebands. Isotropic peaks were identified by running at two spinning speeds at each field; the highest-speed spectrum is shown. Unlike for Ni[P(OPh)$_3$]$_4$, the solid state ^{31}P spectrum was useful for characterizing the compound, as a large peak was observed for the equilibrium product PPh$_3$. The presence of triphenylphosphine supports the notion that Ni(PPh$_3$)$_3$ is present in the solid state as well as solution (Figure 37).

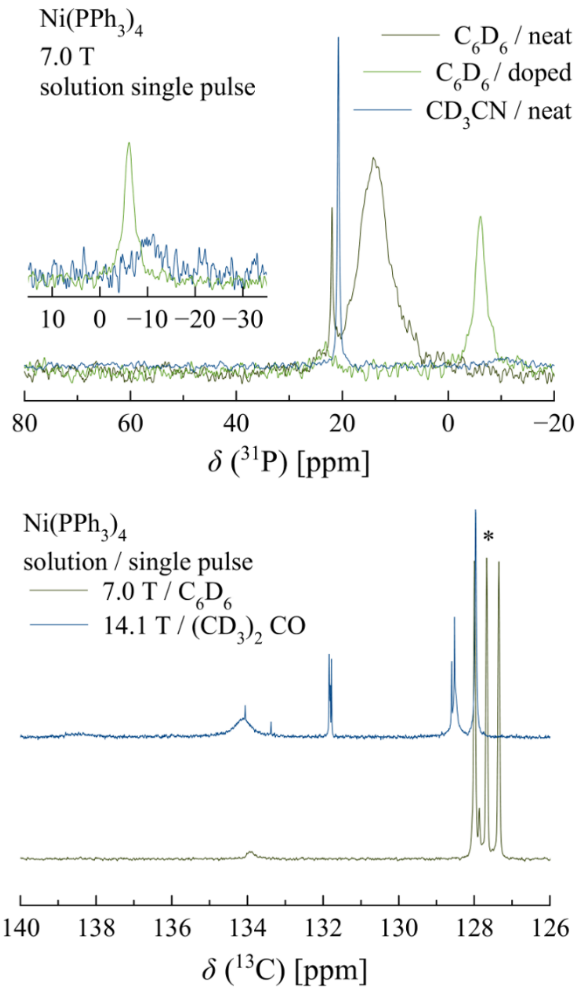

Figure 37: ^{31}P (top) and ^{13}C (bottom) solution NMR spectra of $Ni(PPh_3)_4$ in benzene-d6, acetone-d6, and acetonitrile-d3, with doped samples including dissolved PPh_3. The ^{31}P inset shows the broad triphenylphosphine peak present in acetonitrile; the relative integration of 1.0 to 3.0 for the narrow peaks present in this solvent is evidence that the broad peak in C_6D_6 (corresponding to $Ni(PPh_3)_4$ in fast exchange) is completely converted to $Ni(PPh_3)_3$ and PPh_3 in this acetonitrile. In the ^{13}C spectrum '*' denotes the solvent 1:1:1 triplet of benzene. The presence of broadened peaks in both solvents indicates the presence of a fast-exchanging species ($Ni(PPh_3)_4$), but the sharper peaks present in acetone indicate the presence of a significant amount of $Ni(PPh_3)_3$ and triphenylphosphine.

The equilibrium of [3-2] and its solvent dependence are readily observable in solution ^{31}P and ^{13}C NMR spectra (Figure 37), and the temperature dependence of the equilibrium has been previously characterized by NMR studies (among other methods).[112] For both nuclides, the appearance of relatively high-integration and broad peaks suggests a strong influence from rapid ligand exchange (although initially it was believed this might be due to the formation of paramagnetic nickel degradation products), with the proportion of signal stemming from the trigonal planar and tetrahedral species being strongly solvent dependent: in benzene-d6 most of the phosphorus signal in the sample stems from the broadened, tetrahedral species line shape; in acetone-d6 and acetonitrile-d3 the equilibrium appears to favour the trigonal planar form. In the case of acetonitrile-d3 in particular the peak areas of the free ligand and other signal are 1.0 to 3.0, which, while taking into account the uncertainty in the integration, is what would be expected from dissociation of $Ni(PPh_3)_4$.

Benzene-d6 was selected to attempt characterization of the ^{61}Ni solution NMR spectrum of $Ni(PPh_3)_4$ but no signal was obtained at 21.1 T after many hours of acquisition, likely due to broadening of the signal under rapid ligand exchange. At this time it is unlikely that solution ^{61}Ni NMR spectroscopy is possible for this compound at room temperature due to the interplay of unfavourable kinetics and thermodynamics for this species in a wide range of solvents. However, in the future it may be possible to extract the *J* coupling pattern for this species by running experiments at low temperature, where it has been shown by ^{31}P NMR in solution that the rate of exchange is slowed considerably.

Table 6: Experimentally measured ^{61}Ni NMR parameters for the chemical species studied in this work. Errors are given in parentheses. Errors for Ni(cod)$_2$ were obtained by iterative fitting at two fields; errors for Ni(PPh$_3$)$_4$ were determined by taking advantage of the satellite transitions.

Compound	δ_{iso} [ppm]	Ω [ppm]	κ	$\lvert C_Q \rvert$ [MHz]	η	α [deg]	β [deg]	γ [deg]
Ni(cod)$_2$	965 (10)	1700 (50)	-0.15 (0.05)	2.0(0.3)	0.5(0.2)	65 (10)	140 (5)	110 (5)
Ni(PPh$_3$)$_4$	515 (10)	50(50)	0.5(0.5)	0.05(0.01)	0.0(0.2)	0[a]	90 (45)	0[b]
Ni[P(OPh)$_3$]$_4$								
Site 1	-500 to -550	-	-	0 to 3.5	-	-	-	-
Site 2	-590 to -635	-	-	0 to 3.5	-	-	-	-

[a] Simulated line shape invariant to parameter variation

[b] Simulated line shape weakly sensitive to parameter variation but a conclusive range cannot be determined due to signal-to-noise limitations

3.2 Computational

3.2.1 *ZORA DFT*

A summary of chemical shift and *J* coupling results obtained from ZORA-DFT calculations for a series of nickel compounds is provided in Table 8. As discussed in Section 3.2.2, chemical shifts were obtained from the computed magnetic shielding values either by using a correlation method or by using $Ni(CO)_4$ as the reference. It is worth noting that in general the chemical shifts calculated by calibrating versus $Ni(CO)_4$ are significantly closer to experimental values from solution (including literature values[59,61,64]) and the solid state than those obtained using the correlation method (a plot of the correlation between experimental and calculated chemical shifts for the two methods and basis sets is provided in Figure 39). The span and skew information for the calculated lines is generally uninteresting (since most of the species are expected to produce very narrow lines); these are included in Appendix II.

With respect to computation of chemical shifts, the RMSD errors presented in this work are greater than for Buhl et al, but there is some reason to be confident in the results presented here. Most notably, the regression method did not produce any improvement over direct calibration (and indeed, for both basis sets produced a larger RMSD). The regression method used by Buhl et al may have yielded better results in their work because of the small number of compounds with negative δ_{iso} values they modelled (two, as opposed to four modelled here); indeed, as seen in Figure 39, $Ni(C_2H_4)_2(PMe_3)$ (at $\delta_{iso}(exp) = -866$ ppm), which is a trigonal planar complex, appears to be an outlier in this region. The nickel phosphites (methyl at $\delta_{iso}(exp)$ = -742 ppm and phenyl at $\delta_{iso}(exp)$ = -587 ppm) trend closer to the ideal correlation, and

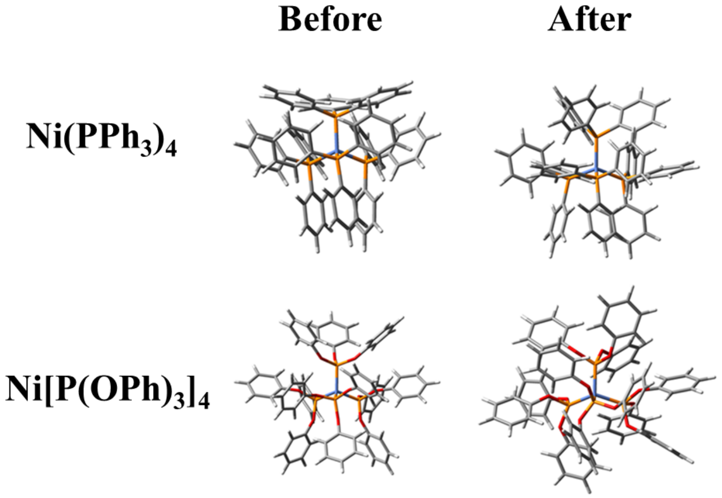

Figure 38: GaussView atomic coordinate plots of Ni(PPh$_3$)$_4$ (top) and Ni[P(OPh)$_3$]$_4$ (bottom) showing initial input structure guesses (left) and final ADF optimized structures (right). Blue denotes nickel, orange phosphorus, red oxygen, grey carbon, and white hydrogen. Note the similarity in the optimized orientations of phenyl moieties and the clear steric benefit to the inclusion of a bridging oxygen bond between the phosphorus and phenyl ring, specifically the inclusion of an extra degree of freedom in orienting the phenyl groups.

Table 7: Comparison of ADF single-molecule ZORA-DFT computational EFG results to previously reported gas-phase computational work by Bühl et al.[64] and experimental solid-state values from this work. All values are determined for the ^{61}Ni site in each compound. Computational details can be found in the main text. Errors are given in parentheses for experimental values. The C_Q values in particular appear to be only marginally affected by the transition from a TZP to a QZ4P basis.

Compound	$\lvert C_Q \rvert$ [MHz]^a	Calc. $\lvert C_Q \rvert$ [MHz]^a		η	Calc. η	
		TZP	QZ4P		TZP	QZ4P
$Ni(CO)_4$	-	0.09	0.14	-	0.19	0.35
$Ni(cod)_2$	2.0(0.3)	4.06	3.93	0.5(0.2)	0.36	0.90
		2.60^b			0.87^b	
$Ni(PMe_3)_4$	-	0.16	0.15	-	0.90	0.71
$Ni[P(OMe)_3]_4$	-	1.65	1.69	-	0.24	0.16
$Ni(PF_3)_4$	-	0.04	0.06	-	0.60	0.67
$Ni(PCl_3)_4$	-	0.02	0.02	-	0.40	0.70
$Ni(C_2H_4)_2(PMe_3)$	-	30.9	29.7	-	0.27	0.23
		38.0^b			0.20^b	
$Ni(PPh_3)_4$	0.05(0.05)	5.58	-	0.0(0.2)	0.08	-
$Ni[P(OPh)_3]_4$	0 to 3.5	4.37	-	-	0.94	-
$Ni(PPh_3)_3$	-	21.0	-	-	0.09	-

[a] C_Q can take the value of any real number, but only the magnitude is measurable by NMR spectroscopy.
[b] Non-relativistic GIAO DFT value from [64]

if excluded might result in a fit closer to parallel with the ideal correlation, which the regression method would treat as a systematic shift. Overall then, exclusion of the nickel phosphite chemical shifts would make it appear that $Ni(CO)_4$ alone is not treated properly by hybrid functionals. On the contrary, from Figure 39 it would appear that the high frequency shifts are underestimated in the direct calibration regime, not $Ni(CO)_4$ and the low frequency chemical shifts. Regardless of what effects are causing this discrepancy between low- and high-frequency ^{61}Ni chemical shifts, there is clearly room for further exploration of the effects of HF mixing on the computation of ^{61}Ni NMR chemical shifts.

Table 8: Comparison of single-molecule ZORA DFT computed isotropic chemical shift and *J* coupling results to previously reported solution experimental values and gas-phase computational work. All values are determined for the ^{61}Ni site in each compound. Computational details can be found in the main text. Boldface compounds were studied by experiment in this work.

Compound	δ_{iso} [ppm]		Calculated δ_{iso} [ppm]				$J(^{61}Ni\text{-}^{31}P)$ [Hz]	Calculated $J(^{61}Ni\text{-}^{31}P)^{a}$ [Hz]	
			TZP		QZ4P			TZP	QZ4P
Ni(CO)$_4$	0	284^{c}	0	-118^{e}	0	-52^{e}	-	-	-
Ni(cod)$_2$	**$937^{a,b}$**	**802^{c}**	**347^{d}**	**561^{e}**	**536^{d}**	**401^{e}**	**-**	**-**	**-**
Ni(PMe$_3$)$_4$	40^{b}	23^{c}	-240^{d}	-146^{e}	-184^{d}	-210^{e}	285^{f}	246	281
Ni[P(OMe)$_3$]$_4$	-742^{f}	-	-684^{d}	-680^{e}	-720^{d}	-671^{e}	398^{g}	396	450
Ni(PF$_3$)$_4$	-929^{f}	-738^{c}	-879^{d}	-916^{e}	-961^{d}	-878^{e}	482^{g}	413	468
Ni(PCl$_3$)$_4$	267^{f}	245^{c}	-18^{d}	121^{e}	86^{d}	21^{e}	450^{g}	385	441
Ni(C$_2$H$_4$)$_2$(PMe$_3$)	-866^{c}	-937^{c}	-988^{d}	-1048^{e}	-1155^{d}	-1044^{e}	-	227	262
Ni(PPh$_3$)$_4$	**$515^{a,h}$**	**-**	**103^{d}**	**267^{e}**	**-**	**-**	**-**	**243**	**-**
Ni[P(OPh)$_3$]$_4$	**-587^{a}** **-576^{b}**	**-**	**-618^{d}**	**-602^{e}**	**-**	**-**	**400^{a}**	**408**	**-**
Ni(PPh$_3$)$_3$	-	-	-562^{d}	-534^{e}	-	-	-	326	-

[a] From this work
[b] From [20]
[c] From [64]
[d] From the regression method
[e] From direct calibration versus Ni(CO)$_4$ magnetic shielding
[f] From [60]
[g] From [59]
[h] For this compound the isotropic chemical shift is for the solid

The ^{61}Ni-^{31}P *J* coupling constants at both TZP and QZ4P levels agree well with experiment,[59] including the value measured for Ni[P(OPh)$_3$]$_4$ in this work (400 ± 20 Hz), and are possibly related to the electronegativity of the substituent on the phosphorus site, as suggested by Hao et al. from solution NMR experiments.[59]

EFG tensor information from ZORA-DFT calculations is presented in Table 7. The calculated ^{61}Ni quadrupolar coupling constants follow the trends predicted by symmetry and ligand bulk for the tetrakis(methylphosphine)nickel(0) and tetrakis(trimethylphosphite)nickel(0) pair (namely that for isostructural species the electron withdrawing ability of the substituents is expected to have an effect on the C_Q)[12], with $Ni(PMe_3)_4$ predicted to have the smaller quadrupolar coupling constant (on the order of tens to hundreds of kilohertz) relative to $Ni[P(OMe)_3]_4$ (on the order of a few megahertz). On the other hand, the calculated $Ni(PPh_3)_4$ and $Ni[P(OPh)_3]_4$ C_Q values do not mirror the methyl-derivative trend, which is at odds with what was observed experimentally. Based on the NMR spectra presented in this work, it appears that crystal structure plays a significant role in the solid-state chemistry of these compounds in particular, which is not captured by single-molecule gas-phase computations. The discrepancies between computational C_Q and η values in this work versus Bühl et al.[64] (Table 7), particularly for $Ni(cod)_2$, suggest that computational ^{61}Ni NMR results are highly dependent on very small structural changes, but are nevertheless useful for anticipating the order of magnitude of the interactions involved. Overall, comparing the results shows that the inability to obtain $Ni(PPh_3)_4$ and $Ni[P(OPh)_3]_4$ values with the QZ4P basis does not seem to have resulted in a loss of significant information.

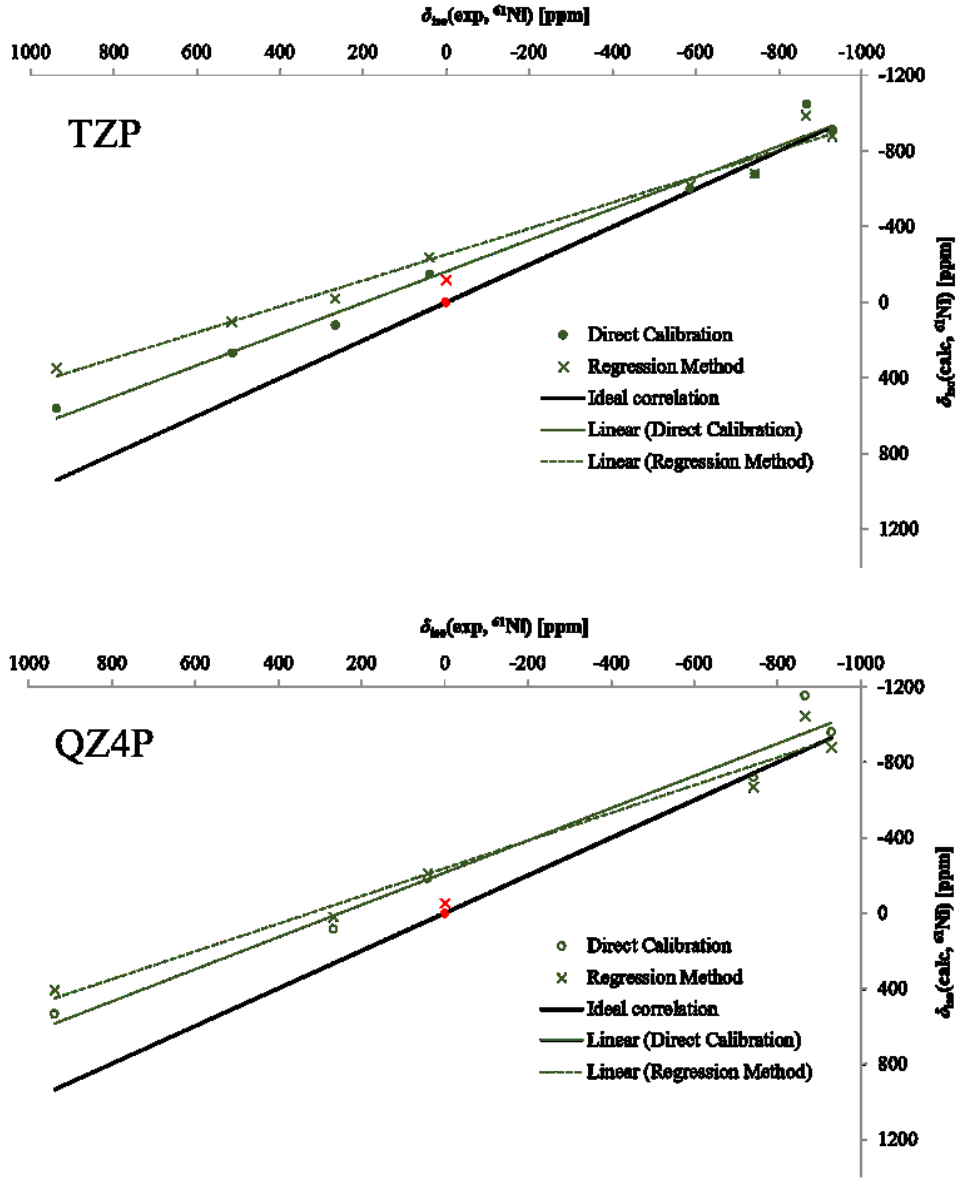

Figure 39: Correlation between experimental δ_{iso} values (see Table 8) and δ_{iso} values obtained computationally in this work. $Ni(PPh_3)_4$ is included, using its isotropic shift as determined in the solid state. Overall, high-frequency chemical shifts appear to be systematically underestimated by the computational methods used. For TZP the equation of the line of best fit for the direct calibration is $\delta_{\text{iso}}(\text{calc}) = (0.827 \pm 0.047)\delta_{\text{iso}}(\text{exp}) - (164 \pm 32)$, with $R^2 = 0.981$ and a RMSD of 192 ppm. The equation of the line of best fit for the regression method is $\delta_{\text{iso}}(\text{calc}) = (0.687 \pm 0.039)\delta_{\text{iso}}(\text{exp}) - (254 \pm 27)$, with $R^2 = 0.981$ and a RMSD of 296 ppm. For QZ4P the equation of the line of best fit for the direct calibration is $\delta_{\text{iso}}(\text{calc}) = (0.856 \pm 0.077)\delta_{\text{iso}}(\text{exp}) - (215 \pm 55)$, with $R^2 = 0.969$ and a RMSD of 234 ppm. The equation of the line of best fit for the regression method is $\delta_{\text{iso}}(\text{calc}) = (0.736 \pm 0.066)\delta_{\text{iso}}(\text{exp}) - (237 \pm 47)$, with $R^2 = 0.969$ and a RMSD of 271 ppm. $Ni(CO)_4$ (in red) exhibited issues similar to those seen by Bühl et al.[64] when the TZP basis was used; it was not used when determining the equation of the fit or when calculating errors.

3.2.2 GIPAW DFT

Given the lack of crystal structures reported for the target compounds of this work, extended crystal structure calculations using GIPAW DFT were minimal. Nonetheless, results were obtained for $Ni(cod)_2$ at an ultrafine level using the crystal structure published by Proserpio et al.[94] The results (Table 9) are essentially equivalent within error to those given by ZORA DFT computations (given the differences between calculations run at the ZORA-QZ4P and ZORA-TZP levels), although some key distinctions should be noted. Namely, it appears that the C_Q value (3.38 MHz) and quadrupolar asymmetry (η = 0.39) are improved (moved closer to the experimental results) by use of an extended crystal structure calculation. On the other hand, the CSA appears to be even more underestimated using GIPAW DFT than ZORA DFT, with the span in particular decreasing to Ω = 1288 ppm with the use of CASTEP. This may be due to the fact that ZORA DFT calculations are all-electron and include spin-orbit terms (which are important for magnetic shielding calculations in particular), while the use of pseudopotentials by GIPAW DFT limits it to back-prediction of electron properties in the core region. Overall, however, the computational results (apart from $Ni(PPh_3)_4$) differ from experiment with about the same magnitude observed in literature for vanadium-51[114] and cobalt-59[115] NMR spectroscopy and DFT computations.

Table 9: A comparison of the computationally-derived fit parameters obtained using various levels of theory (described in the text) for Ni(cod)$_2$, including experimental results. It is difficult to draw general conclusions about which level of theory produces the 'best' results; ZORA appears to capture the CSA parameters better, but GIPAW produces the set of EFG values most consistent with the experimental fit.

Model	$\|C_Q\|$ [MHz][a]	Calc. η	Ω [ppm]	κ
Experimental	2.0 ± 0.3	0.5 ± 0.2	1700 ± 50	-0.15 ± 0.05
GIPAW DFT (PBE/ultrafine)	3.38	0.39	1288	0.11
ZORA DFT (B3LYP/TZP)	4.06	0.36	1306	-0.25
ZORA DFT (B3LYP/QZ4P)	3.93	0.90	1428	-0.22
GIAO DFT[b] (B3LYP/II')	2.60	0.87	-	-

[a] C_Q can take the value of any real number, but only the magnitude is measurable by NMR spectroscopy.

[b] From [64]

4 CONCLUSION

This thesis has provided the first SSNMR spectra of ^{61}Ni for non-metallic species, specifically for a series of diamagnetic Ni(0) complexes. The broad ^{61}Ni line shape of Ni(cod)$_2$ presented provides evidence that, especially with the use of high fields, valuable spectra can be acquired even for elements with as unfavourable nuclear and chemical properties as nickel. ^{61}Ni NMR proved invaluable in providing an explanation for the solid-state behaviour of Ni(PPh$_3$)$_4$ and offering insights into the crystallographic nature of Ni[P(OPh)$_3$]$_4$. Ni(cod)$_2$ saturated in C_6D_6 has also been proposed as a secondary chemical shift reference for ^{61}Ni, which should make the field of nickel NMR more user-friendly in the future. With the level of recent interest in the field of nickel catalysis and synthesis of (in particular) diamagnetic Ni(0) compounds for catalytic processes in mind, ^{61}Ni NMR spectroscopy has been demonstrated to be a tool which has considerable applications in structural, and perhaps even mechanistic characterization.

NMR spectroscopy of various challenging nuclides continues to be indispensable. particularly when other techniques prove unsuitable or insufficient in explaining organometallic chemistry. While NMR spectroscopy of co-ordinating ligand nuclei (involving ^{1}H, ^{13}C, ^{19}F, and ^{31}P among several other nuclides) can provide a great deal of information, it also forfeits the knowledge that can be gained by directly probing the environment of transition metal centers. As a result, significant information regarding the chemistry and structure regarding metal complexes can be lost, particularly at the site most pivotal to the chemical behaviour of the overall compound. NMR of insensitive nuclides opens up the possibility of directly studying centers of interest, thanks to recent advances in magnetic field strengths, solid-state NMR methodology,[110] and sensitivity-enhancement techniques.[26,116,117] In the solid state in particular, NMR spectroscopy provides crucial information, both as a complement to X-ray diffraction but especially in amorphous, disordered, or otherwise crystallographically difficult species, where characterization by X-ray crystallography becomes difficult or impossible.

REFERENCES

(1) Chandrasekhar, S. *Philos. Mag.* **1931**, *11* (70), 592–596.

(2) Ramsey, N. F. *Phys. Rev.* **1950**, *78* (6), 699–703.

(3) Widdifield, C. M.; Schurko, R. W. *Concepts Magn. Reson. Part A* **2009**, *34A* (2), 91–123.

(4) Chizhik, V. I.; Chernyshev, Y. S.; Donets, A. V.; Frolov, V. V.; Komolkin, A. V.; Shelyapina, M. G. *Magnetic Resonance and Its Applications*; Springer International Publishing: Cham, 2014.

(5) Still, B. M.; Kumar, P. G. A.; Aldrich-Wright, J. R.; Price, W. S. *Chem. Soc. Rev.* **2007**, *36* (4), 665–686.

(6) Mueller, L. J. *Concepts Magn. Reson. Part A* **2011**, *38A* (5), 221–235.

(7) Robert, J. B.; Wiesenfeld, L. *Phys. Rep.* **1982**, *86* (7), 363–401.

(8) Anet, F. A. L.; O'Leary, D. J. *Concepts Magn. Reson. Part A* **1991**, *3* (4), 193–214.

(9) Levitt, M. H. *Spin Dynamics*, 2nd ed.; John Wiley & Sons, Ltd: Chichester, UK, 2013.

(10) Herzfeld, J.; Berger, A. E. *J. Chem. Phys.* **1980**, *73* (12), 6021–6030.

(11) Ford, K. W.; Hill, D. L. *Phys. Rev.* **1954**, *94* (6), 1630–1637.

(12) Autschbach, J.; Zheng, S.; Schurko, R. W. *Concepts Magn. Reson. Part A* **2010**, *36A* (2), 84–126.

(13) Samoson, A. *Chem. Phys. Lett.* **1985**, *119* (1), 29–32.

(14) Andrew, E. R. *Int. Rev. Phys. Chem.* **1981**, *1* (2), 195–224.

(15) Vaara, J.; Jokisaari, J.; Wasylishen, R. E.; Bryce, D. L. *Prog. Nucl. Magn. Reson. Spectrosc.* **2002**, *41* (3–4), 233–304.

(16) *Solid State NMR Spectroscopy*, 1st ed.; Duer, M. J., Ed.; Blackwell Science Ltd.:

Hoboken, 2001.

(17) Schurko, R. W. *Acc. Chem. Res.* **2013**, *46* (9), 1985–1995.

(18) *Modern NMR techniques and their application in chemistry*; Popov, A. I., Hallenga, K., Eds.; M. Dekker: New York, 1991.

(19) Harris, R. K.; Becker, E. D.; Cabral de Menezes, S. M.; Goodfellow, R.; Granger, P. *Pure Appl. Chem.* **2001**, *73* (11), 1795–1818.

(20) Benn, R.; Rufińska, A. *Angew. Chem. Int. Ed. Engl.* **1986**, *25* (10), 861–881.

(21) Benn, R.; Reinhardt, R.-D.; Rufińska, A. *J. Organomet. Chem.* **1985**, *282* (2), 291–295.

(22) Benn, R.; Michael Büch, H.; Reinhardt, R.-D. *Magn. Reson. Chem.* **1985**, *23* (7), 559–564.

(23) Dechter, J. In *Progress in Inorganic Chemistry; Volume 33*; Lippard, S. J., Ed.; John Wiley & Sons, 1985; p 393.

(24) Rees, G. J.; Orr, S. T.; Barrett, L. O.; Fisher, J. M.; Houghton, J.; Spikes, G. H.; Theobald, B. R. C.; Thompsett, D.; Smith, M. E.; Hanna, J. V.; Rossi, M.; Skelton, B. W.; Sobolev, A. N.; White, A. H. *Phys. Chem. Chem. Phys.* **2013**, *15* (40), 17195.

(25) Mastrorilli, P.; Todisco, S.; Bagno, A.; Gallo, V.; Latronico, M.; Fortuño, C.; Gudat, D. *Inorg. Chem.* **2015**, *54* (12), 5855–5863.

(26) Kobayashi, T.; Perras, F. A.; Goh, T. W.; Metz, T. L.; Huang, W.; Pruski, M. *J. Phys. Chem. Lett.* **2016**, *7* (13), 2322–2327.

(27) Knight, M. J.; Felli, I. C.; Pierattelli, R.; Emsley, L.; Pintacuda, G. *Acc. Chem. Res.* **2013**, *46* (9), 2108–2116.

(28) Kim, J.; Middlemiss, D. S.; Chernova, N. A.; Zhu, B. Y. X.; Masquelier, C.; Grey, C. P. *J. Am. Chem. Soc.* **2010**, *132* (47), 16825–16840.

(29) Granger, P. *Encyclopedia of Magnetic Resonance*; John Wiley & Sons, Ltd: Chichester, UK, 2007.

(30) Rehder, D. *Coord. Chem. Rev.* **2008**, *252* (21–22), 2209–2223.

(31) Howarth, O. W. *Prog. Nucl. Magn. Reson. Spectrosc.* **1990**, *22* (5), 453–485.

(32) Pyykkö, P. *Mol. Phys.* **2008**, *106* (16–18), 1965–1974.

(33) Larsen, F. H.; Farnan, I.; Lipton, A. S. *J. Magn. Reson.* **2006**, *178* (2), 228–236.

(34) Bryce, D. L.; Wasylishen, R. E. *Phys. Chem. Chem. Phys.* **2001**, *3* (23), 5154–5157.

(35) Forgeron, M. A. M.; Wasylishen, R. E. *Magn. Reson. Chem.* **2008**, *46* (3), 206–214.

(36) Rüegger, H. *Magn. Reson. Chem.* **2004**, *42* (9), 814–818.

(37) Seitchik, J. A.; Gossard, A. C.; Jaccarino, V. *Phys. Rev.* **1964**, *136* (4A), A1119–A1125.

(38) Matsuda, K.; Kohori, Y.; Kohara, T. *Phys. Rev. B* **1997**, *55* (22), 15223–15227.

(39) Fedotov, M. A.; Likholobov, V. A. *Bull. Acad. Sci. USSR Div. Chem. Sci.* **1984**, *33*, 1751.

(40) Widdifield, C. M.; Perras, F. A.; Bryce, D. L. *Phys. Chem. Chem. Phys.* **2015**, *17* (15), 10118–10134.

(41) O'Dell, L. A.; Moudrakovski, I. L. *J. Magn. Reson.* **2010**, *207* (2), 345–347.

(42) Wagler, T. A.; Daunch, W. A.; Rinaldi, P. L.; Palmer, A. R. *J. Magn. Reson.* **2003**, *161* (2), 191–197.

(43) Tasker, S. Z.; Standley, E. A.; Jamison, T. F. *Nature* **2014**, *509*, 299–309.

(44) Wilke, G. *Angew. Chem. Int. Ed. Engl.* **1988**, *27*, 185–206.

(45) Yamaguchi, J.; Muto, K.; Itami, K. *Eur. J. Org. Chem.* **2013**, 19–30.

(46) Taylor, B. L. H.; Swift, E. C.; Waetzig, J. D.; Jarvo, E. R. *J. Am. Chem. Soc.* **2011**, *133* (3), 389–391.

(47) Harris, M. R.; Hanna, L. E.; Greene, M. A.; Moore, C. E.; Jarvo, E. R. *J. Am. Chem. Soc.*

2013, *135* (9), 3303–3306.

(48) Zhou, J.; Fu, G. C. *J. Am. Chem. Soc.* **2003**, *125*, 14726–14727.

(49) *The Mizoroki-Heck Reaction*; Oestreich, M., Ed.; Wiley, 2009.

(50) Miller, K. M.; Jamison, T. F. *J. Am. Chem. Soc.* **2004**, *126*, 15342–15343.

(51) Moslin, R. M.; Jamison, T. F. *Org. Lett.* **2006**, *8*, 455–458.

(52) Qiu, Z. Late transition metal-carboryne complexes: synthesis, structure, bonding, and reaction with alkenes and alkynes, Springer, 2012.

(53) Iyer, S.; Sattar, A. K. *Synth. Commun.* **1998**, *28* (10), 1721–1725.

(54) Bamford, C. H.; Hargreaves, K. *Nature* **1966**, *209*, 292.

(55) Brandsma, L.; Vasilevsky, S. F.; Verkruijsse, H. D. In *Application of Transition Metal Catalysts in Organic Synthesis*; Springer, 1999; p 227.

(56) Lyons, J. E. In *Aspects of Homogeneous Catalysis : A Series of Advances Volume 3*; Ugo, R., Ed.; Springer Netherlands, 1977; p 29.

(57) Drain, L. *Phys. Lett.* **1964**, *11* (2), 114–115.

(58) Schumann, H.; Meissner, M.; Kroth, H.-J. *Zeitschrift fur Naturforsch. B* **1980**, *35* (5), 639–641.

(59) Hao, N.; McGlinchey, M. J.; Sayer, B. G.; Schrobilgen, G. J. *J. Magn. Reson.* **1982**, *46* (1), 158–162.

(60) Avent, A. G.; Cloke, F. G. N.; Day, J. P.; Seddon, E. A.; Seddon, K. R.; Smedley, S. M. *J. Organomet. Chem.* **1988**, *341* (1–3), 535–541.

(61) Benn, R.; Rufińska, A. *Magn. Reson. Chem.* **1988**, *26* (10), 895–902.

(62) Behringer, K. D.; Blümel, J. *Magn. Reson. Chem.* **1995**, *33* (9), 729–733.

(63) Behringer, K. D.; Blümel, J. *Inorg. Chem.* **1996**, *35* (7), 1814–1819.

(64) Bühl, M.; Peters, D.; Herges, R. *Dalton Trans.* **2009**, *30*, 6037–6044.

(65) Segransan, P. J.; Clark, W. G.; Chabre, Y.; Carter, G. C. *J. Phys. F Met. Phys.* **1976**, *6* (5), L153–L156.

(66) Segransan, P. J.; Chabre, Y.; Clark, W. G. *J. Phys. F Met. Phys.* **1978**, *8* (7), 1513–1524.

(67) Mishina, S.; Iwamoto, Y.; Kohori, Y.; Ueda, K.; Kohara, T.; Jung, M.-H.; Takabatake, T. *J. Appl. Phys.* **2000**, *87* (9), 5134.

(68) Bastow, T. J.; West, G. W. *J. Phys. Condens. Matter* **2003**, *15* (49), 8389–8406.

(69) Keeler, J. *Understanding NMR Spectroscopy*, 2nd ed.; John Wiley and Sons, 2010.

(70) McClung, R. E. D. *Concepts Magn. Reson.* **1999**, *11* (1), 1–28.

(71) Vega, A. J. In *Encyclopedia of Magnetic Resonance*; John Wiley & Sons, Ltd: Chichester, UK, 2010.

(72) Maricq, M. M.; Waugh, J. S. *J. Chem. Phys.* **1979**, *70* (7), 3300–3316.

(73) Bodart, P. R.; Amoureux, J.-P.; Dumazy, Y.; Lefort, R. *Mol. Phys.* **2000**, *98* (19), 1545–1551.

(74) Perras, F. A.; Viger-Gravel, J.; Burgess, K. M. N.; Bryce, D. L. *Solid State Nucl. Magn. Reson.* **2013**, *51–52*, 1–15.

(75) Siegel, R.; Nakashima, T. T.; Wasylishen, R. E. *Concepts Magn. Reson. Part A* **2005**, *26A* (2), 62–77.

(76) Carr, H. Y.; Purcell, E. M. *Phys. Rev.* **1954**, *94* (3), 630–638.

(77) Meiboom, S.; Gill, D. *Rev. Sci. Instrum.* **1958**, *29* (8), 688–691.

(78) Garroway, A. N. *J. Magn. Reson.* **1977**, *28* (3), 365–371.

(79) Engel, T.; Reid, P.; Hehre, W. *Physical Chemistry*, 3rd ed.; Pearson Education, Inc., 2013.

(80) van Lenthe, E.; Baerends, E.-J.; Snijders, J. G. *J. Chem. Phys.* **1993**, *99* (6), 4597–4610.

(81) van Lenthe, E.; Baerends, E.-J.; Snijders, J. G. *J. Chem. Phys.* **1994**, *101* (11), 9783–9792.

(82) van Lenthe, E.; van Leeuwen, R.; Baerends, E.-J.; Snijders, J. G. *Int. J. Quantum Chem.* **1996**, *57* (3), 281–293.

(83) Lenthe, E. van; Snijders, J. G.; Baerends, E.-J. *J. Chem. Phys.* **1996**, *105*, 6505.

(84) Lenthe, E. van; Ehlers, A.; Baerends, E.-J. *J. Chem. Phys.* **1999**, *110*, 8943.

(85) te Velde, G.; Bickelhaupt, F. M.; Baerends, E. J.; Fonseca Guerra, C.; van Gisbergen, S. J. A.; Snijders, J. G.; Ziegler, T. *J. Comput. Chem.* **2001**, *22* (9), 931–967.

(86) Magyarfalvi, G.; Wolinski, K.; Hinton, J.; Pulay, P. In *Encyclopedia of Magnetic Resonance*; John Wiley & Sons, Ltd: Chichester, UK, 2011.

(87) Pickard, C. J.; Mauri, F. *Phys. Rev. B* **2001**, *63* (24), 245101.

(88) Blöchl, P. E. *Phys. Rev. B* **1994**, *50* (24), 17953–17979.

(89) Bühl, M. *Chem. Phys. Lett.* **1997**, *267* (3–4), 251–257.

(90) Bühl, M. *Theor. Chem. Acc.* **2002**, *107* (6), 336–342.

(91) Wender, P. A.; Smith, T. E. In *Encyclopedia of Reagents for Organic Synthesis*; John Wiley & Sons, Ltd: Chichester, UK, 2001.

(92) Hedberg, L.; Iijima, T.; Hedberg, K. *J. Chem. Phys.* **1979**, *70* (7), 3224–3229.

(93) Nickel, T.; Goddard, R.; Krüger, C.; Pörschke, K.-R. *Angew. Chem. Int. Ed. Engl.* **1994**, *33* (8), 879–882.

(94) Macchi, P.; Proserpio, D. M.; Sironi, A. *J. Am. Chem. Soc.* **1998**, *120* (7), 1447–1455.

(95) Almenningen, A.; Andersen, B.; Astrup, E. E. *Acta Chem. Scand.* **1970**, *24*, 1579–1584.

(96) Dick, D. G.; Stephan, D. W.; Campana, C. F. *Can. J. Chem.* **1990**, *68*, 628–632.

(97) ADF2016. SCM, Theoretical Chemistry, Vrije Universiteit, Amsterdam, The Netherlands, http://www.scm.com.

(98) Fonseca Guerra, C.; Snijders, J. G.; te Velde, G.; Baerends, E. J. *Theor. Chem. Acc.* **1998**, *99* (6), 391–403.

(99) GaussView, Version 4. Dennington, R.; Keith, T.A.; Millam, J.M. Semichem Inc., Shawnee Mission, KS, 2016.

(100) Becke, A. D. *Phys. Rev. A* **1988**, *38*, 3098–3100.

(101) Perdew, J. P. *Phys. Rev. B* **1986**, *33*, 8822–8824.

(102) Becke, A. D. *J. Chem. Phys.* **1993**, *98*, 5648–5652.

(103) Stephens, P. .; Devlin, F. J.; Chabalowski, M. J.; Frisch, J. *J. Phys. Chem.* **1994**, *98*, 11623–11627.

(104) Clark, S. J.; Segall, M. D.; Pickard, C. J.; Hasnip, P. J.; Probert, M. J.; Refson, K.; Payne, M. C. *Zeitschrift fuer Krist.* **2005**, *220* (5–6), 567–570.

(105) Yates, J. R.; Pickard, C. J.; Mauri, F. *Phys. Rev. B* **2007**, *76*, 24401.

(106) Profeta, M.; Mauri, F.; Pickard, C. J. *J. Am. Chem. Soc.* **2003**, *125*, 541.

(107) Perdew, J. P.; Burke, K.; Ernzerhof, M. *Phys. Rev. Lett.* **1996**, *77*, 3865–3868.

(108) WSolids1. Eichele, K. Universitat Tubingen, 2015.

(109) Blaakmeer, E. S.; Antinucci, G.; Busico, V.; van Eck, E. R. H.; Kentgens, A. P. M. *J. Phys. Chem. C* **2016**, *120* (11), 6063–6074.

(110) Bodner, G. M.; Gaul, M. M. *J. Organomet. Chem.* **1975**, *101*, 63–69.

(111) Tolman, C. A.; Seidel, W. C.; Gerlach, D. H. *J. Am. Chem. Soc.* **1972**, *94* (8), 2669–2676.

(112) Mynott, R.; Mollbach, A.; Wilke, G. *J. Organomet. Chem.* **1980**, *199* (1), 107–109.

(113) Tolman, C. A. *J. Am. Chem. Soc.* **1970**, *92* (10), 2956–2965.

(114) Ooms, K. J.; Bolte, S. E.; Smee, J. J.; Baruah, B.; Crans, D. C.; Polenova, T. *Inorg. Chem.* **2007**, *46* (22), 9285–9293.

(115) Crewdson, P.; Bryce, D. L.; Rominger, F.; Hofmann, P. *Angew. Chemie Int. Ed.* **2008**, *47*, 3454–3457.

(116) Venkatesh, A.; Hanrahan, M. P.; Rossini, A. J. *Solid State Nucl. Magn. Reson.* **2017**.

(117) Perras, F. A.; Kobayashi, T.; Pruski, M. *J. Magn. Reson.* **2016**, *264*, 125–130.

APPENDIX I – SOME USEFUL OPERATORS AND STATES

Shift Operators

$$\hat{I}_+ = \hat{I}_x + \mathrm{i}\hat{I}_y \qquad \hat{I}_- = \hat{I}_x - \mathrm{i}\hat{I}_y$$

Angular Momentum Operators (*I* = 1/2)

$$\hat{I}_x = \left(\frac{1}{2}\right)\begin{bmatrix} 0 & 1 \\ 1 & 0 \end{bmatrix} \qquad \hat{I}_y = \left(\frac{1}{2\mathrm{i}}\right)\begin{bmatrix} 0 & 1 \\ -1 & 0 \end{bmatrix} \qquad \hat{I}_z = \left(\frac{1}{2}\right)\begin{bmatrix} 1 & 0 \\ 0 & 1 \end{bmatrix}$$

Angular Momentum Operators (*I* = 3/2)

$$\hat{I}_x = \left(\frac{1}{2}\right)\begin{bmatrix} 0 & \sqrt{3} & 0 & 0 \\ \sqrt{3} & 0 & 2 & 0 \\ 0 & 2 & 0 & \sqrt{3} \\ 0 & 0 & \sqrt{3} & 0 \end{bmatrix} \qquad \hat{I}_y = \left(\frac{1}{2\mathrm{i}}\right)\begin{bmatrix} 0 & \sqrt{3} & 0 & 0 \\ -\sqrt{3} & 0 & 2 & 0 \\ 0 & -2 & 0 & \sqrt{3} \\ 0 & 0 & -\sqrt{3} & 0 \end{bmatrix}$$

$$\hat{I}_z = \left(\frac{1}{2}\right)\begin{bmatrix} 3 & 0 & 0 & 0 \\ 0 & 1 & 0 & 0 \\ 0 & 0 & -1 & 0 \\ 0 & 0 & 0 & -3 \end{bmatrix}$$

Spin States (incl. Superposition States) (*I* = 1/2)

$$|\alpha\rangle = \begin{bmatrix} 1 \\ 0 \end{bmatrix} \qquad |\beta\rangle = \begin{bmatrix} 0 \\ 1 \end{bmatrix}$$

$$|x\rangle = \left(\frac{1}{\sqrt{2}}\right)\begin{bmatrix} 1 \\ 1 \end{bmatrix} \qquad |-x\rangle = \left(\frac{1}{\sqrt{2}}\right)\begin{bmatrix} -\mathrm{i} \\ \mathrm{i} \end{bmatrix}$$

$$|y\rangle = \left(\frac{1}{2}\right)\begin{bmatrix} 1-\mathrm{i} \\ 1+\mathrm{i} \end{bmatrix} \qquad |-y\rangle = \left(\frac{1}{2}\right)\begin{bmatrix} 1+\mathrm{i} \\ 1-\mathrm{i} \end{bmatrix}$$

APPENDIX II – FULL CHEMICAL SHIFT TENSOR INFORMATION FOR ZORA DFT NMR COMPUTATIONS ON NICKEL

Compound	Span (Ω) [ppm]		Skew (κ)	
	TZP	QZ4P	TZP	QZ4P
$Ni(CO)_4$	5.2	5.0	0.22	0.66
$Ni(cod)_2$	1306	1428	-0.25	-0.22
$Ni(PMe_3)_4$	3.8	5.5	0.01	0.14
$Ni[P(OMe)_3]_4$	21	26	-0.30	-0.30
$Ni(PF_3)_4$	2.4	1.6	0.05	0.62
$Ni(PCl_3)_4$	5.9	0.7	-0.07	-0.47
$Ni(C_2H_4)_2(PMe_3)$	516	527	0.69	0.65
$Ni(PPh_3)_4$	132	-	-0.99	-
$Ni[P(OPh)_3]_4$	216	-	0.46	-
$Ni(PPh_3)_3$	1898	-	-0.85	-

APPENDIX III – SAMPLE COMPUTATIONAL INPUT FILES AND PULSE PROGRAMS

Sample ADF (ZORA DFT) geometry optimization

```
#! /bin/bash
#$ -S /bin/bash
#$ -N NBAPN_geom.run
#$ -q abaqus.q
#$ -l qname=abaqus.q
#$ -M pwerh080@uottawa.ca
#$ -m be
#$ -o NBAPN_geom.out
#$ -e test.err
#$ -V
#$ -cwd
#$ -pe shm.pe 8
adf -n $NSLOTS <test.adf >test.log

#!/bin/sh

$ADFBIN/adf << eor
Title NBAPN - scf

Basis
 Type TZP
 Core None
End

relativistic spinorbit zora

XC
 GGA BP86
End

Symmetry NOSYM

Atoms
 Ni                 0.16889533    1.26994539   -0.00163868
 C                 -0.54637510   -0.48418242   -0.00553527
 C                  0.95332573   -0.45435606   -0.00833428
 C                 -0.94652169    2.77355792    0.00474087
 C                 -1.69232884    1.47210934    0.00292230
 H                 -1.07958847   -0.48355545    0.92214092
 H                  1.48653910   -0.45498256   -0.93601047
```

```
 H                  -0.68002864    3.23617648    0.93203021
 H                  -1.95882230    1.00949101   -0.92436704
 H                   1.44179974   -0.45400516    0.83397488
 H                  -0.70211813    3.19578722   -0.83792217
 H                  -1.96090425    1.00812114    0.92892564
 H                  -1.08315972   -0.48456746   -0.93114973
 P                   1.92323861    2.59745407   -0.00224601
 C                   1.37223287    4.33098940   -0.06264406
 H                   0.76532484    4.54234617    0.79286220
 H                   2.22548165    4.97664135   -0.06293944
 H                   0.80194920    4.49314706   -0.95336367
 C                   2.89325384    2.32163450    1.51280977
 H                   3.21719677    1.30246812    1.54831851
 H                   3.74650261    2.96728645    1.51251439
 H                   2.28634580    2.53299127    2.36831603
 C                   2.95554947    2.23795003   -1.45740619
 H                   3.80879825    2.88360198   -1.45770157
 H                   3.27949241    1.21878365   -1.42189744
 H                   2.38526580    2.40010769   -2.34812579
End

Integration 6.0

Geometry
  optim cartes
End

SAVE TAPE10
SAVE TAPE15
SAVE TAPE21

END INPUT
eor
```

Sample ADF (ZORA DFT) NMR calculation

```
#! /bin/bash
#$ -S /bin/bash
#$ -N NBAPN_NMR.run
#$ -q abaqus.q
#$ -l qname=abaqus.q
#$ -M pwerh080@uottawa.ca
#$ -m be
#$ -o NBAPN_NMR.out
#$ -e test.err
#$ -V
#$ -cwd
#$ -pe shm.pe 8
adf -n $NSLOTS <test.adf >test.log
```

```
#!/bin/sh

$ADFBIN/adf << eor
Title NBAPN - scf

Basis
 Type TZP
 Core None
End

SCF
 Iterations 5000
End

relativistic spinorbit zora

XC
 Hybrid B3LYP
End

Symmetry NOSYM

Atoms
   Ni        0.015625    1.304479   -0.010918
   C        -0.328142   -0.659312   -0.103498
   C         1.050137   -0.399716   -0.203382
   C        -1.275953    2.813130    0.196318
   C        -1.955903    1.582822    0.167521
   H        -0.758307   -1.022222    0.832942
   H         1.544067   -0.462082   -1.176571
   H        -1.131023    3.335029    1.146309
   H        -2.473009    1.256263   -0.737712
   H         1.705394   -0.581993    0.653366
   H        -1.271448    3.463113   -0.682641
   H        -2.325886    1.135088    1.092415
   H        -0.908441   -0.902319   -0.996346
   P         1.795918    2.526053   -0.035022
   C         1.654710    4.365107   -0.190115
   H         1.036351    4.757203    0.626742
   H         2.640861    4.849588   -0.160273
   H         1.161817    4.615531   -1.138131
   C         2.836249    2.394470    1.490998
   H         3.136972    1.349854    1.638911
   H         3.734639    3.024182    1.420690
   H         2.245174    2.705526    2.361806
   C         3.047731    2.184475   -1.354947
   H         3.913920    2.856113   -1.271722
   H         3.387794    1.144511   -1.278878
   H         2.582101    2.320048   -2.339588
End

Integration 6.0
```

```
SAVE TAPE10
SAVE TAPE21

qtens

End Input
eor

cp TAPE21 t21
cp TAPE10 t10

$ADFBIN/nmr << eor
NMR
  U1K BEST
  Out TENS
  Atoms 1
  SCF 1.d-4
END
eor

rm TAPE10 TAPE15 TAPE21
cp t21 TAPE21
cp t10 TAPE10

$ADFBIN/cpl<< eor
maxmemoryusage 40
nmrcoupling
atompert {1}
atomresp {14}
dso
pso
sd
fc
scf {convergence=1e-7}
END

END INPUT
eor
```

QCPMG pulse program

```
# 1 "/opt/topspin/exp/stan/nmr/lists/pp/user/lao.QCPMG_dec"
; QCPMG
; Written by Luke O'Dell, March 2010

; Modified with full echo acquisition
; and 8-step phase cycling

;parameters:
```

```
;ns : should be a multiple of 8
;d1 : recycle delay
;d3 : time to allow pulse ringdown
;d10 : enter duration of echo
;p1 : Pulse length
;pl1 : Pulse power
;pl2 : CW decoupling power on channel 2
;l22 : # of echos to be acquired
;setTD : ensure TD exceeds this
;spikesep : spikelet separation in Hz
;d25 : not used
;d26 : not used

# 1 "/opt/topspin/exp/stan/nmr/lists/pp/Avancesolids.incl" 1
;Avancesolids.incl
;   for 1
;
;version 1 28.2.2001, written by HF
;       4.4.2006, complemented by Ste

;switch between 1H or 19F output (H amplifier)
;version 1 28.2.2001, written by HF     4.4.2006,
;complemented by Ste
;$COMMENT=definitions for setrtp and setnmr
;$CLASS=Solids INCL

;switch between 1H or 19F output (H amplifier) gating pulse for RX22,
ADC and HPPR
;$OWNER=Bruker

;gating pulse for RX22, ADC and HPPR
;generate dwell clock
;blank/unblank receiver path
;turn dwell clock on/off
;
;define data sampling for WAHUHA type experiments

;explicit transmitter blanking

;NCO switching


# 21 "/opt/topspin/exp/stan/nmr/lists/pp/user/lao.QCPMG_dec" 2


define delay echod
"echod=(d10/2)+2u"
define delay setTD
"setTD=(5u+p1+(d10/2)+l22*(2*d3+p1+4u+d10))/dw"
"d25=1/setTD"
define delay spikesep
"spikesep=(1/(2*d3+4u+p1+d10))"
```

```
"d26=spikesep"


# 1 "mc_line 33 file
/opt/topspin/exp/stan/nmr/lists/pp/user/lao.QCPMG_dec dc-measurement
inserted automatically"
    dccorr
# 33 "/opt/topspin/exp/stan/nmr/lists/pp/user/lao.QCPMG_dec"
1 ze
2 d1
  10u reset:f1
  (1u adc ph31 syrec)
  (1u ph30:r):f1
  1u setrtp1^0^1^2
  1u setnmr0|0^16
  1u pl2:f2
  1u cw:f2
  (p1 pl1 ph1):f1
  echod
3 d3
  (p1 pl1 ph2):f1
  d3
  1u setrtp1|7
  1u setnmr0^0|16
  d10 setrtp1|0|1|2
  1u setrtp1^0^1^2
  1u setnmr0|0^16
  lo to 3 times l22
  1u do:f2
  1u setrtp1^7
  rcyc=2
  10m wr #0
exit

ph0=0
ph1=0 0 1 1 2 2 3 3
ph2=1 3 2 0 3 1 0 2
ph30=0
ph31=0 0 1 1 2 2 3 3
```

Quadrupolar echo pulse program

```
# 1 "/opt/topspin/exp/stan/nmr/lists/pp/user/solidecho_2.av"
;solidecho.av
;90-180 solid echo sequence for wide line observation


;set d6 to 5-100usec depending on dead time
;set d7 shorter than d6 by 3usec plus 10 dw to make
;sure the evolution of the echo is obvserved, then left shift
;FID prior to ft to get smallest possible 1st order pohase correction
```

```
;set receiver phase either with phcor0 or with HPCU receiver phase
;to get maximum signal in ADC channel A and almost no signal in
channel B
;for minimum 0 order phase correction (no signal in channel B  is only
;possible if O1 exactly in center and spectrum perfectly symmetric).
;phase cycle will cancel deadtime partially, but not perfectly

;set:
;d1 : recycle delay
;p1 : X 90 degree pulse
;p2 : X 180 degree pulse
;pl1 : X power level
;d6 : echo delay
;d7 : =0, or no longer than d6-de

# 1 "mc_line 23 file
/opt/topspin/exp/stan/nmr/lists/pp/user/solidecho_2.av dc-measurement
inserted automatically"
    dccorr
# 23 "/opt/topspin/exp/stan/nmr/lists/pp/user/solidecho_2.av"
1 ze
2 d1
  10u pl1:f1
3 1u
  (p1 ph1):f1
  d6
  (p2 ph2):f1
  d7
  go=2 ph31
  wr #0
exit

ph0=0
ph1= 0 0 0 0 1 1 1 1 2 2 2 2 3 3 3 3
ph2= 0 1 2 3
ph31= 3 1 3 1 2 0 2 0 1 3 1 3 0 2 0 2
```